INFORMATION TO USERS

NOTE TO USERS

The original manuscript received by UMI contains pages with slanted print. Pages were microfilmed as received.

This reproduction is the best copy available

UMI

WAVE ENERGY CONVERSION IN A RANDOM SEA

by

JOHN M. WARNER

A dissertation Submitted to the
Faculty of Engineering
in Partial Fulfilment of the Requirements
for the Degree of

DOCTOR OF PHILOSOPHY
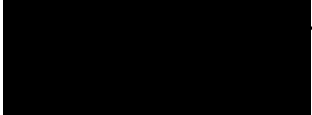
Major Subject: Fisheries Engineering

APPROVED:

K.C.Watts _____ (Supervisor)

M.G. Satish ___

M. Rahman ___

J.S. Pawlowski (External Examiner)

TECHNICAL UNIVERSITY OF NOVA SCOTIA

Halifax, Nova Scotia   1997

TECHNICAL UNIVERSITY OF NOVA SCOTIA

AUTHORITY TO DISTRIBUTE MANUSCRIPT THESIS

TITLE:

WAVE ENERGY CONVERSION IN A RANDOM SEA

The above library may make available or authorize another library to make available individual photo/microfilm copies of this thesis without restrictions

Full Name of Author: John M. Warner

Signature of Author:

Date: November 15, 1997

ii

TABLE OF CONTENTS

LIST OF TABLES

LIST OF FIGURES

LIST OF FIGURES (Continued)

x

LIST OF FIGURES (Continued)

LIST OF ABBREVIATIONS AND SYMBOLS USED

Symbol		Brief Definition	Dimensions
a	=	Characteristic horizontal dimension (radius for a cylindrical device, half-length for a square device)	L
A	=	Interior OWC surface area	L^2
A_{kj}	=	Real added mass coefficient matrix	M
b_a	=	Normalized applied damping coefficient	-
b_r	=	Normalized radiation damping coefficient	-
B	=	Boundary of all solid surfaces	-
B_a	=	Applied damping coefficient	MT^{-1}
B_r	=	Radiation damping coefficient	MT^{-1}
B_{kj}	=	Real radiation damping coefficient matrix	MT^{-1}
C_z	=	Normalized vertical diffraction force coefficient	-
CWR	=	Capture width Ratio	-
$\overline{\text{CWR}}$	=	Average capture width ratio in random seas	-
d_n	=	Coefficients of an approximate dispersion relationship	-
$\overline{E}$	=	Average wave energy per unit width	MLT^{-2}
f	=	Wave frequency	T^{-1}
f_n	=	Natural frequency of device	T^{-1}

Symbol		Brief Definition	Dimensions
f_o	=	Peak wave spectral frequency	T^{-1}
$\bar{f}_{k_o}$	=	Froude Krylov force	MLT^{-2}
$\bar{f}_{k_j}$	=	Radiation force components	MLT^{-2}
$\bar{f}_{k_z}$	=	Diffraction force components	MLT^{-2}
$\bar{f}_k$	=	Linearized hydrodynamic resultant force	MLT^{-2}
F	=	Free surface boundary	-
$F_d(t)$	=	Time-dependent diffraction force	MLT^{-2}
$F_{p_d}(t)$	=	Time-dependent dynamic pressure force	MLT^{-2}
$F_r(t)$	=	Time-dependent radiation force	MLT^{-2}
g	=	Acceleration due to gravity	LT^{-2}
$G(\theta)$	=	Directional spreading function	-
h	=	Water depth	L
H	=	Wave height	L
H_c	=	Characteristic wave height	L
H_{rms}	=	Root-mean squared wave height	L

LIST OF ABBREVIATIONS AND SYMBOLS USED (Continued)

Symbol		Brief Definition	Dimensions
$H_{1/3}$	=	Significant wave height	L
$H_{z_{1/3}}$	=	Zero up-crossing significant wave height	L
i	=	Imaginary unit; $\sqrt{-1}$	-
J	=	Stationary functional	-
$\lvert J \rvert$	=	Jacobian matrix	-
k	=	Wave number	L^{-1}
k_m	=	Imaginary roots of dispersion relationship	L^{-1}
k_r	=	Restoring force coefficient	MT^{-2}
K_j	=	Assembled matrices	-
K_n	=	Modified Bessel function	-
l_d	=	Device draft dimension (front wall)	L
l_x, l_y, l_z	=	Characteristic device dimension	-
m	=	Mass of rigid plate	M
m_a	=	Added mass coefficient	M
m_0	=	Area under wave spectra	L^2
m_1	=	1ˢᵗ moment, spectral density function	L^2T^{-1}

Symbol		Brief Definition	Dimensions
m_2	=	2nd moment, spectral density function	L^2T^{-2}
n_j	=	Directional cosines	-
N_{tot}	=	Total number of wave observations	-
OWC	=	Oscillating water column	-
P	=	Wave power per unit crest width	MLT^{-3}
P(t)	=	Instantaneous wave power	MLT^{-3}
P_e	=	Average wave power extraction	MLT^{-3}
$P_e(t)$	=	Instantaneous wave power extraction	MLT^{-3}
$P_{1/n}$	=	Average of the highest 1/n wave power values	MLT^{-3}
P_N	=	Normalized wave power	-
$p_d(t)$	=	Instantaneous dynamic wave pressure	$ML^{-1}T^{-2}$
pdf	=	Probability density function	-
pdf(x)	=	pdf of random variable x	-
pdf(x,y)	=	Joint pdf of random variables x and y	-
ΔP	=	Air pressure differential	$ML^{-1}T^{-2}$
$\bar{P}_{e_N}$	=	Average normalized wave power extraction in random seas	-

Symbol		Brief Definition	Dimensions
$\bar{P}_N$	=	Available average normalized wave power in random seas	-
Q	=	Air flow rate	L^3T^{-1}
Q_r, Q_{pj}	=	Assembled vectors	-
r	=	Radial position in wave plane	L
R	=	Normalized wave height (H/H_{rms})	-
s	=	Wave directional spreading coefficient	-
S	=	Boundary of Artificial Cylindrical Surface	-
S(f)	=	Spectral density function	L^2T
S(f,θ)	=	Directional spectral density function	L^2T
t	=	Time	T
T	=	Wave Period	T
T_e	=	Energy Period	T
$T_{m_{01}}$	=	Average wave spectra period (m_0/m_1)	T
$T_{m_{02}}$	=	Average wave spectra period ($\sqrt{m_0/m_2}$)	T
T_p	=	Spectra peak period	T

LIST OF ABBREVIATIONS AND SYMBOLS USED (Continued)

Symbol		Brief Definition	Dimensions
T_z	=	Average zero crossing period	T
$u(t)$	=	Time dependent horizontal orbital wave velocity	LT^{-1}
U_j	=	Vector of unknown coefficients	-
V	=	Normal velocity distribution	LT^{-1}
W_T	=	Dimensionless wave period	-
$\overline{W}_T$	=	Mean dimensionless wave period	-
$(W_T)_{res}$	=	Dimensionless resonant wave period	-
x,y,z	=	Position in wave plane	L

LIST OF GREEK SYMBOLS

Symbol		Brief Definition	Dimensions
$\alpha_o =$	=	Wave amplitude	L
α_{mn}, β_{mn}	=	Coefficients of the exterior eigen function expression	-
$\beta(v)$	=	Numerically integrated function	-
ϵ	=	Wave phase	-
$\overline{\xi}$	=	Nodal coordinates	-
ξ_j	=	Displacement associated with a mode of oscillation	L

Symbol		Brief Definition	Dimensions
ξ	=	Internal OWC surface displacement	L
$\dfrac{d\xi}{dt}$	=	Internal OWC surface velocity	LT^{-1}
$\dfrac{d^2\xi}{dt^2}$	=	Internal OWC surface acceleration	LT^{-2}
ξ_o	=	Internal OWC surface amplitude of occilation	L
η	=	Free-surface water displacement	L
$\overline{\eta^2(x,t)}$	=	Mean squared surface elevation	L^2
θ_w	=	Wave direction	-
$\bar{\theta}$	=	Mean wave direction	-
ρ	=	Water density	ML^{-3}
μ	=	Normalized added mass coefficient	-
τ	=	Normalized wave period ($T/T_{m_{01}}$)	-
Φ	=	Velocity potential	L^2T^{-1}
Φ_s	=	Scattered wave velocity potential	L^2T^{-1}
Φ_o	=	Incident wave velocity potential	L^2T^{-1}

LIST OF ABBREVIATIONS AND SYMBOLS USED (Continued)

Symbol		Brief Definition	Dimensions
ν	=	Spectral bandwidth parameter	-
ψ	=	Phase angle of force and displacement	-
ω	=	Angular wave frequency	T^{-1}
ω_n	=	Natural frequency of OWC	T^{-1}

ACKNOWLEDGEMENTS

ABSTRACT

The response of a three-dimensional oscillating water column (OWC) wave energy converter in monochromatic and random seas was investigated to determine the potential power available. Probabilistic models of available average wave power in a random sea state were formulated through the development of probability density functions transformed from theoretical distributions of wave heights and periods in a random wave field and a functional relationship describing the wave power. The computed available average wave power in a random sea state was in good agreement with measured wave spectra data. A hybrid-finite element method was used to numerically model the fluid-device interaction and to establish the radiation diffraction hydrodynamic force coefficients for the device. Six OWC devices with varying wall configurations, modelled in finite depth and monochromatic seas, showed considerable variation in peak performance and frequency response bandwidth with a consistent variation in performance between devices for obliquely incident wave directions. The numerical model for monochromatic seas was verified using the results of wave tank experiments. Based on a transformation of random variables using a functional relationship developed for wave power extraction in monochromatic seas, a probabilistic density function of wave power extraction was derived. Based on a linear superposition principle, overall device performance in random seas with narrow and broad banded wave spectra characteristics was determined. In random seas, the performance of the device is influenced by the frequency bandwidth of the wave spectra such that an increase in the spectral bandwidth parameter causes a reduction in peak performance, but effectively broadens the frequency response of the device. Predicted overall device performance in random seas were in agreement with experimental tests.

CHAPTER 1

INTRODUCTION

As ocean waves propagate through deep water into shallow continental shelf regions, the waves begin to transform, dissipating their energy by viscous and bottom friction and the more apparent wave breaking phenomena. The instability of a wave at breaking is the most obvious and spectacular of all the wave processes, revealing the immense energy levels associated with ocean waves. The stresses on the sea surface, due to the complicated local and global wind patterns, produce waves with various characteristics with energy levels potentially available for extraction into useable energy. With approximately 360 million square kilometres (71 percent) of the earth's surface covered with water (Neumann and Pierson (1966)), the availability of ocean wave power is tremendous and has led researchers from numerous countries to study wave energy conversion. The highly irregular ocean wave environment, with temporal and spatial variability of wave height, frequency and direction has made the design of a wave energy conversion device a difficult challenge. However, one of the more promising devices for harnessing ocean wave power is the oscillating water column wave energy converter. Through the continued process of theoretical and experimental research, an operational oscillating water column wave power plant at the Island of Islay, Scotland was constructed in 1992 and is currently producing small scale, low cost, electrical power from ocean waves to the nearby community (Whittaker (1991,1993)).

Physically, the oscillating water column is a rigid, hollow, fixed or floating structure open at the immersed bottom or side (depending on the type of configuration) that traps a volume of air above it. The incoming wave field produces an oscillating pressure field at the subsurface

opening causing the internal free-surface to rise and fall. This oscillation drives the volume of air through a constriction containing an air turbine which is connected to a generator for direct energy conversion. Figure 1.1 depicts the fixed oscillating water column in finite depth. The main advantage of the oscillating water column is that the device is a simple one with no moving parts other than the air turbine and electrical generator.
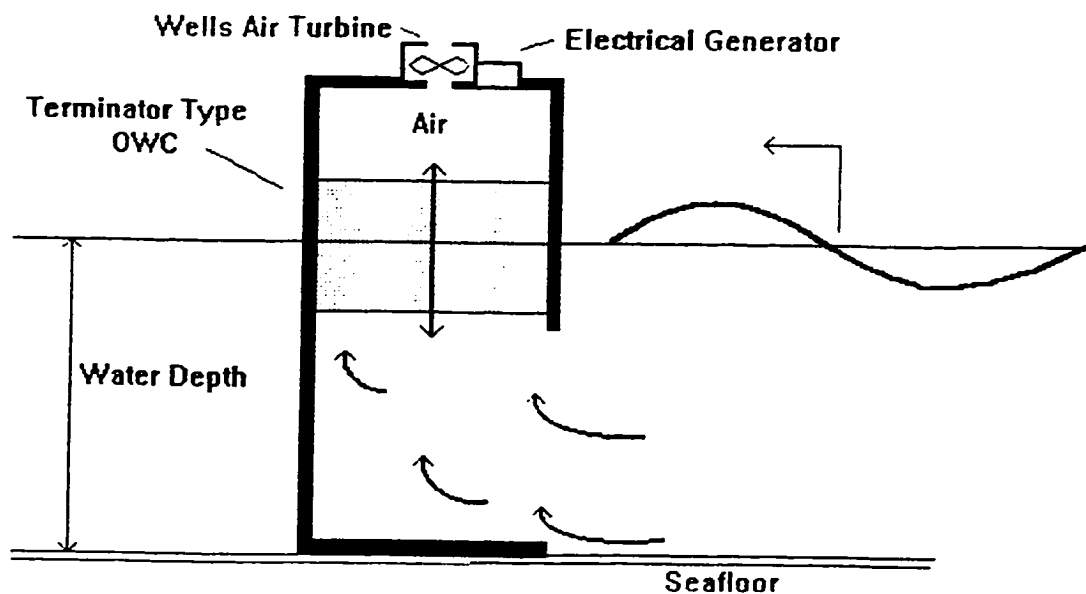
Figure 1.1 The Oscillating Water Column in Finite Depth

The entrained fluid mass within the structure responds well to both regular and irregular sea states with frequencies close to the natural frequency and wave directions normal to the front wall, amplifying the free-surface response and ultimately improving the efficiency of the device.

However, this amplified response is narrow-banded and generally does not respond well to frequencies outside the natural frequency of the device.

Numerous types of oscillating water column devices have been considered in the past and can be classified essentially under three categories.

(1) Attenuator Oscillating Water Column - A hollow structure partially immersed below the free surface. Based on energy conservation, a portion of the energy in the incident wave is transmitted under the structure (attenuated wave). The remaining energy is captured by the device and also lost due to scattering.

(2) Terminator Oscillating Water Column - A hollow structure partially immersed below the free surface along the front face and fully extended along the back and side faces to the sea bed or to an appreciable depth to reduce the transmitted wave energy. The remaining energy is scattered and captured by the device.

(3) Multi Resonant Oscillating Water Column - A structure similar to the terminator type oscillating water column with the exception of two parallel projecting sidewalls in front of the device. Waves entering between the two sidewalls are amplified by an additional resonance with the increased energy levels captured by the device and the remaining energy scattered.

Research into the attenuator type oscillating water column device has shown that an optimized attenuator device can only absorb approximately half of the energy as an equivalent terminator type device (Count et al. (1983)). Because of this, only limited research into the attenuator device has been carried out in the past decade. In the early 1980's, considerable

research efforts were being carried out in the United Kingdom on the Terminator and Multi Resonant Oscillating Water Column devices with the intent of developing an effective device that could generate large scale ocean wave power. However, large scale wave power production schemes at that time were not considered to be cost effective (Grove-Palmer (1982)) and as a result, government funding was significantly reduced in the area of wave power development world wide. Because these early cost estimate studies identified remotely located communities and third world countries as potential sites for small scale wave power development, research has continued with an emphasis on isolated small scale devices capable of generating low cost electricity. The recent construction of the oscillating water column wave power plant at Islay, Scotland is an important step in the development stages of these devices.

Preliminary results on the performance of this oscillating water column wave power plant (Whittaker (1993)) are encouraging but clearly demonstrate a need for further research in predicting the response of the oscillating water column in random seas.

1.1   Research Objectives

An essential step towards a theoretical understanding of the oscillating water column is the accurate prediction of the wave climatology and the hydrodynamic interaction between this wave field and the device. The wave directionality bandwidth response of the various OWC device types has not been thoroughly investigated in the past. In addition, the effects of broadbanded wave spectra on the overall device performance has not been quantified in the past. One of the main goals of this research is to numerically model various geometrical configurations of the oscillating water column and to quantify the response for a wide range of hydrodynamic

conditions in monochromatic and random seas. In particular, this dissertation covers four main research areas:

1. The development of probabilistic models of wave power with the establishment of probability density distributions of wave power and the determination of statistical average wave power values in random seas.

2. Coupling together a three-dimensional numerical finite element model of the fluid and an analytical model describing the motion of the internal oscillating water column surface to describe quantitatively and qualitatively the physical behaviour of the device.

3. A comparative analysis of the frequency and directional response bandwidths for various oscillating water column devices, and verification with experimental results.

4. The development of a probabilistic approach to determine the performance of the oscillating water column device in random seas with narrow and broad banded wave spectra characteristics.

CHAPTER 2

OCEAN WAVE POWER

2.1 Evaluation of the Ocean Wave Power Environment

A vital part in considering the development of wave power as an alternative source of energy is to confirm that the levels of energy in the ocean waves at nearshore or offshore locations are of sufficient magnitude to generate electricity. To do this, an understanding into the physics and transformation processes of ocean waves must be clearly understood. Nearshore locations are often considered the most ideal location for wave energy extraction due to the close proximity to the coastline. However, several changes occur as ocean waves propagate into shallow coastal waters. The transformation of waves travelling from deep to shallow water for long distances lose a tremendous amount of energy due to wave dissipation, primarily in the form of wave breaking and sea bottom friction. Another important consideration in evaluating the ocean wave power environment are sites which are fetch-limited due to the physical constraint of coastal boundaries. The growth of large waves are severely restricted under these conditions which limits the wave power availability at the site. Site locations where consistently strong winds blow over fetch-unlimited seas are ideal conditions for a high wave energy environment and potential wave power extraction. However, these geographical regions are often located greater distances offshore, making it unrealistic for power extraction.

The variability of wave height, frequency and direction of ocean waves also pose a difficult problem in evaluating wave power for potential energy extraction. Because of the temporal and spatial complexity of ocean waves, a comprehensive ocean data collection program is needed for the accurate prediction of ocean wave power. A large wave data base, usually comprised of long-term wave spectral energy information, allows for the mathematical determination of seasonal and long-term statistical wave power levels.

This chapter introduces methods for determining ocean wave power for random wave sea conditions with emphasis on the frequency and directional wave energy spectra. Twenty-years of measured wave data for Osborne Head, Nova Scotia has been analyzed to determine the average and seasonal wave power values by these methods.

2.2 Linear Wave Approximation for Ocean Wave Power

The rate at which work is done is referred to as power. The instantaneous power, $P(t)$ transmitted by a wave can be defined as the product of the instantaneous dynamic pressure force, $F_{p_d}(t)$, and velocity, $u(t)$, of fluid flow across an undisturbed vertical plane in the water column. The instantaneous power on an elemental vertical plane is given by

$$dP(t) = F_{p_d}(t)u(t) \tag{2.1}$$

where $F_{p_d}(t)$ is defined as the product of the instantaneous dynamic pressure $p_d(t)$ and elemental plane area. Therefore

$$F_{p_d}(t) = p_d(t)(1)dz \tag{2.2}$$
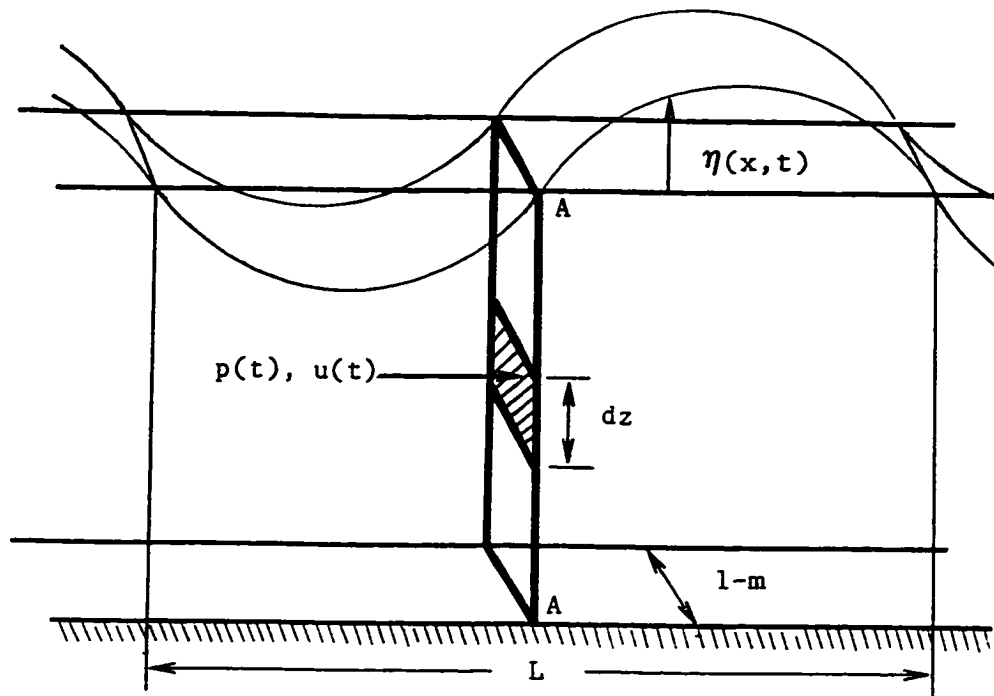
Figure 2.1. Definition Sketch for Ocean Wave Power

and the instantaneous power for the elemental plane becomes

$$dP(t) = p_d(t)u(t)dz \tag{2.3}$$

The instantaneous power across the vertical section A-A, shown in Figure 2.1, per unit width in the direction of wave propagation is

$$P(t) = \int_{-h}^{\eta} p_d(t)u(t)dz \tag{2.4}$$

where η and h are the free-surface displacement and water depth, respectively, and the average wave power over one wave period T is

$$P = \frac{1}{T}\int_{t}^{t+T} \int_{-h}^{\eta} p_d(t)u(t)dz \qquad (2.5)$$

Based upon Linear Wave Theory, $p_d(t)$ and $u(t)$ are given as

$$p_d(t) = \rho g \frac{H}{2} \frac{\cosh \ k(h+z)}{\cosh \ kh} \cos \ \omega t \qquad (2.6)$$

and

$$u(t) = \frac{\pi \ H}{T} \frac{\cosh \ k(h+z)}{\sinh \ kh} \cos \ \omega t \qquad (2.7)$$

where the constant parameters H,T,ω,k,h,ρ, and g are the wave height, wave period, wave frequency, wave number, water depth, density and acceleration due to gravity, respectively. For a linear wave approximation, only the terms to the second order in wave height are retained and it is only necessary to integrate up to the mean free-surface ($\eta \approx 0$). Therefore, substituting equations 2.6 and 2.7 into equation 2.5 gives

$$P = \frac{\rho g \pi H^2}{2T^2} \int_{t}^{t+T} \int_{-h}^{0} \frac{\cosh^2 \ k(h+z)}{\cosh \ kh \ \sinh \ kh} \cdot \cos^2 \omega t \ dzdt \qquad (2.8)$$

and carrying out the integration yields

$$P = \frac{\rho g^2 H^2 T}{32 \pi} \left[1 + \frac{2kh}{\sinh \ 2kh} \right] \tanh \ kh \qquad (2.9)$$

For waves travelling in deep water (i.e. kh→large), the term

$$\left[1 + \frac{2kh}{\sinh \ 2kh} \right] \tanh \ kh \rightarrow 1 \qquad (2.10)$$

and equation 2.9 becomes

$$P = \frac{\rho g^2}{32\pi} H^2 T \qquad (2.11)$$

The above expression is the average wave power (kW/m) per unit width of wave crest. Although it is a linear wave approximation representing a sinusoidal and regular sea state, the equation yields fairly good results for random sea conditions upon substitution of statistical wave parameters derived from the energy spectrum.

2.3 Mathematical Formulation of Random Seas

In a regular sea state, such as the conditions described in the previous section, the average wave power is determined by a linear wave approximation. The free-surface elevation time series ($\eta(x,y,t)$) for a two-dimensional regular sea state is given by

$$\eta(x,y,t) = \alpha_o \cos (kx \cos \theta_w + ky \sin \theta_w - 2\pi f t + \epsilon) \qquad (2.12)$$

where α_o, k, f and ϵ are the wave amplitude, number, frequency, and phase, respectively. This expression represents a simple harmonic wave travelling past a fixed coordinate system with direction θ_w for any time t.

For random sea conditions, the free-surface elevation time series ($\eta(x,y,t)$) is highly irregular, nonrepeatable, and exceedingly complicated. However, Longuet-Higgins (1957) has shown that $\eta(x,y,t)$ in a random sea can be considered as a linear superposition of simple harmonic waves coming from various relative directions $(\theta_w)_n$ and having various amplitudes $(\alpha_o)_n$, phases (ϵ_n), and frequencies (f_n) that can be mathematically expressed by

$$\eta(x,y,t) = \sum_{n=1}^{\infty} (\alpha_o)_n \cos (k_n x \cos (\theta_w)_n + k_n y \sin (\theta_w)_n - 2\pi f_n t + \epsilon) \tag{2.13}$$

It is well known (Lamb, 1932) that the average wave energy, comprised of half kinetic and half potential energy, is given by

$$\overline{E} = \rho g \; \overline{\eta^2(x,y,t)} \tag{2.14}$$

For a single harmonic wave in regular sea state conditions, the mean-squared elevation $(\overline{\eta^2(x,y,t)})$ simply becomes $\alpha_o^2/2$ and average wave energy equals

$$\overline{E} = \frac{1}{2} \rho g \alpha_o^2 = \frac{1}{8} \rho g H^2 \tag{2.15}$$

The mean-square elevation term for random wave conditions is determined by squaring Equation 2.13 and averaging over the period. On squaring the series, all the cross products average out to be zero because of the orthogonality of cosine functions and each square term contributes a mean value of $1/2 \; (\alpha_o)_i^2$ to the mean total energy. Therefore, total mean energy for a random sea state is given by

$$\overline{E} = \frac{1}{2} \rho g \sum_{i=1}^{\infty} (\alpha_o)_i^2 \tag{2.16}$$

The sum of $1/2 (\alpha_o)_i^2$ defines the spectral density function

$$\sum_{f}^{f+\Delta f} \frac{1}{2} (\alpha_o)_i^2 = S(f)\Delta f \tag{2.17}$$

or, directional spectral energy function

$$\sum_{f}^{f \cdot \Delta f} \sum_{\theta}^{\theta \cdot \Delta \theta} \frac{1}{2} (\alpha_o)_i^2 = S(f,\theta)\Delta f \Delta \theta \qquad (2.18)$$

The area under the spectral energy function is the total energy of the wave energy spectrum and is often defined by the parameter m_0. Higher moments of the spectral density function are defined by

$$m_n = \int_0^\infty f^n S(f) df \qquad (2.19)$$

and are often used for the determination of statistical wave parameters that are representative of the spectrum. Equations 2.17, 2.18, and 2.19 are extremely useful functions for the determination of average wave power as well as other ocean related problems. In many cases the spectral density function (S(f)) or directional spectral density function (S(f,θ)) are represented by theoretical wave energy spectra dependent on wave frequency, direction, and statistical parameters (i.e. significant wave height (H_s) and peak wave frequency (f_o)) that are derived from the discrete wave energy spectrum.

Numerous parametric spectra of the form S(f) have been developed for the one-dimensional (non-directional) spectrum. Some of the most widely used are the Pierson Moscowitz (1964), Scott (1965), and JONSWAP (Hasslemann et al., 1973) spectra described in Table 2.1.

Table 2.1

Parametric Wave Spectra

1. Pierson-Moscowitz Spectrum	where
$S(f) = \dfrac{A}{f^5} \exp - \left[\dfrac{B}{f^4} \right]$	$A = \dfrac{5}{16} H_c^2 f_o^4$ $B = \dfrac{5}{4} f_o^4$
2. Scott Spectrum $S(f) = 1.34 H_c^2 \exp - \left[\dfrac{(f-f_o)^2}{0.01(f-f_o+0.042)} \right]^{1/2}$	for $-0.041 < f-f_o < 0.26$ 0, outside that range
3. JONSWAP Spectrum $S(f) = \dfrac{5}{16\gamma^{1/3}} \left[\dfrac{f}{f_o} \right]^{-5} \exp \left[\dfrac{-5}{4} \left[\dfrac{f_o}{f} \right]^4 \right] \gamma^a$	where $a = \exp \left[-\dfrac{(f-f_o)^2}{2\,\sigma^2\,f_o^2} \right]$ $\sigma = \begin{cases} 0.07 & f \le f_o \\ 0.09 & f > f_o \end{cases}$ $\gamma = \left[\dfrac{S(f_o)}{\dfrac{5H_c^2}{16f_o} \exp - \left[\dfrac{5}{4} \right]} \right]^{3/2}$

In Table 2.1, S(f) is the variance of sea-surface displacement in m^2/Hz; f is the frequency, and f_o the frequency of the peak energy of the spectrum; H_c is the characteristic wave height in metres and defined as 4 times the square root of the area under the spectrum (m_0).

The directional parametric spectrum ($S(f,\theta)$) can be portioned into a one-dimensional spectral density function (S(f)) and a directional spreading factor ($G(\theta)$) about the mean direction ($\bar{\theta}$). In general, the directional spectral density function can be expressed by

$$S(f,\theta) = S(f)G(\theta) \tag{2.20}$$

where a commonly used directional spreading function put forward by Borgman (1979) is

$$G(\theta) = g(s)\cos^{2s}\left(\frac{\theta - \bar{\theta}}{2}\right) \quad, \tag{2.21}$$

often referred to as the cosine squared function. The parameter $g(s)$ is a normalizing function to ensure that

$$\int_{0}^{2\pi} G(\theta)d\theta = 1 \tag{2.22}$$

and s is an empirically found spreading coefficient depending upon locally generated wind waves or swell waves.

2.4   Existing Methods for the Determination of Average Wave Power in a Random Sea State

In Section 2.2, the average wave power in a regular sea state (sinusoidal waves of constant height and period) was determined by a linear wave approximation. Although this ideal sea state does not occur in the real ocean, some qualitative and quantitative conclusions can be inferred. The average wave power is given by:

$$P = \frac{\rho g^2}{32\pi} H^2 T [1 + \frac{2kh}{\sinh 2kh}] \tanh kh \tag{2.23}$$

For a random sea, which can be considered as a linear superposition of an infinite number of regular waves of height H_i, period T_i, and wave number k_i, equation 2.23 can be expressed as

$$P = \frac{\rho g^2}{32\pi} \sum_{i=1}^{\infty} H_i^2 T_i \left[1 + \frac{2k_i h}{\sinh 2k_i h}\right] \tanh k_i h \tag{2.24}$$

or, in terms of wave amplitude and frequency

$$P = \frac{\rho g^2}{8\pi} \sum_{i=1}^{\infty} \frac{(\alpha_o)_i^2}{f_i} \left[1 + \frac{2k_{f_i}h}{\sinh 2k_{f_i}h} \right] \tanh k_{f_i}h \qquad (2.25)$$

Baird and Mogridge (1976) recognized the summation term to be similar in form to the mean square elevation for random waves. Recalling that $\overline{\eta^2(x,t)}$ for irregular waves is

$$\overline{\eta^2(x,t)} = \sum_{i=1}^{\infty} \frac{1}{2} (\alpha_o)_i^2 = \int_0^{\infty} S(f)df \qquad (2.26)$$

and by substituting equation 2.26 into equation 2.25, the expression developed by Baird and Mogridge (1976) for average wave power is

$$P = \frac{\rho g^2}{4\pi} \int_0^{\infty} \frac{S(f)}{f} \left[1 + \frac{2k_f h}{\sinh 2k_f h} \right] \tanh k_f h\, df \qquad (2.27)$$

which for deep water conditions, reduces to

$$P = \frac{\rho g^2}{4\pi} \int_0^{\infty} \frac{S(f)}{f}\, df \qquad (2.28)$$

Equations 2.27 and 2.28 are the most widely used for the determination of average wave power in an irregular sea state. The expressions sum the power associated with each frequency component of the wave energy spectrum. Therefore, narrow or broad-banded wave energy spectra with single or multiple energy peaks can be accounted for by discretely integrating over the upper and lower frequency bounds of the spectra.

Because Baird and Mogridge (1976) have used a linear wave approximation in their derivation, the assumption of a linear wave with a Gaussian type distribution for free-surface elevation is invoked. However, shallow coastal water waves that have a non-Gaussian type distribution for free-surface elevations will have a different level of wave energy and power than

the linear wave approximation. As kh becomes small for shallow water conditions, the linear wave approximation reduces to

$$P = \frac{\rho g H^2}{8} \sqrt{gh} \tag{2.29}$$

For non-linear shallow water waves, the expression for average wave power using Stokes' second order theory is

$$P = \frac{\rho g H^2}{8} \sqrt{gh} \left[1 + \frac{9}{1024}(gH)^2 \left(\frac{T}{\pi h} \right)^4 \right] \tag{2.30}$$

By comparison of equations 2.29 and 2.30, it can be seen that the non-linear shallow water wave contains a higher order term of magnitude $9/1024\ (gH)^2(T/\pi h)^4$ which is dependent on wave height and period. The extent of deviation of deep water ocean waves from a linear Gaussian distribution will, however, depend upon the sea severity and water depth (Ochi and Wang (1984)).

Funke and Mansard (1979) have determined the average wave power for directional irregular waves in a similar approach as Baird and Mogridge (1976). For three-dimensional waves with a directional wave energy spectrum, the expression for mean-squared elevation is given by

$$\overline{\eta^2(x,y,t)} = \int_0^\infty \int_0^{2\pi} S(f,\theta)d\theta df \tag{2.31}$$

where $S(f,\theta)$ is the directional spectral density function. Therefore, average wave power can be expressed as

$$P = \frac{\rho g^2}{4\pi} \int_0^{\infty} \int_0^{2\pi} \frac{S(f,\theta)}{f} \left[1 + \frac{2k_f h}{\sinh 2k_f h}\right] \tanh k_f h \, d\theta df \qquad (2.32)$$

which for deep water conditions, reduces to

$$P = \frac{\rho g^2}{4\pi} \int_0^{\infty} \int_0^{2\pi} \frac{S(f,\theta)}{f} \, d\theta df \qquad (2.33)$$

Integrating S(f,θ) over the limits of 0 to 2π, reduces equations 2.32 and 2.33 to the expressions obtained by Baird and Mogridge. Therefore, depending upon the type of measured spectral density function (S(f) or S(f,θ)) available, either approach is acceptable for the determination of average wave power in a random sea state. Pontes et al. (1995) have recently compiled an atlas of the wave energy resource in Europe based on the relationship given in Equation 2.33 and a deep water wave forecasting model.

As an example, directional wave data obtained during the Canadian Atlantic Storm Program (CASP) for January 28, 1986, 18:00 - 24:00 GMT, is used to determine the average wave power by the methods described above. The completed form of the data are represented by discrete directional spectral densities extending from 0.035 Hz to 0.500 Hz in equal increments of 0.005 Hz and from 0 degrees to 360 degrees in equal increments of 22.5 degrees. A three-dimensional plot of the directional wave energy spectrum (S(f,θ)) is presented in Figure 2.2. The corresponding frequency and directional wave energy spectra (S(f) and S(θ)) are shown in Figures 2.3 and 2.4, respectively. The advantage of a three-dimensional plot is that the fractional distribution of energy for all directions and frequencies is completely described and viewed pictorially. From Figure 2.2, a dominant peak energy of 35 m^2/Hz rad occurs at a peak direction and frequency of 162 degrees and 0.08 Hz, respectively. The frequency spectrum is narrow banded with the majority of energy close to the peak frequency, whereas the directional

spectrum depicts a greater spread of energy over the various wave directions. By discretizing

Equation 2.33, the average wave power was calculated to be 119.6 kW/m.
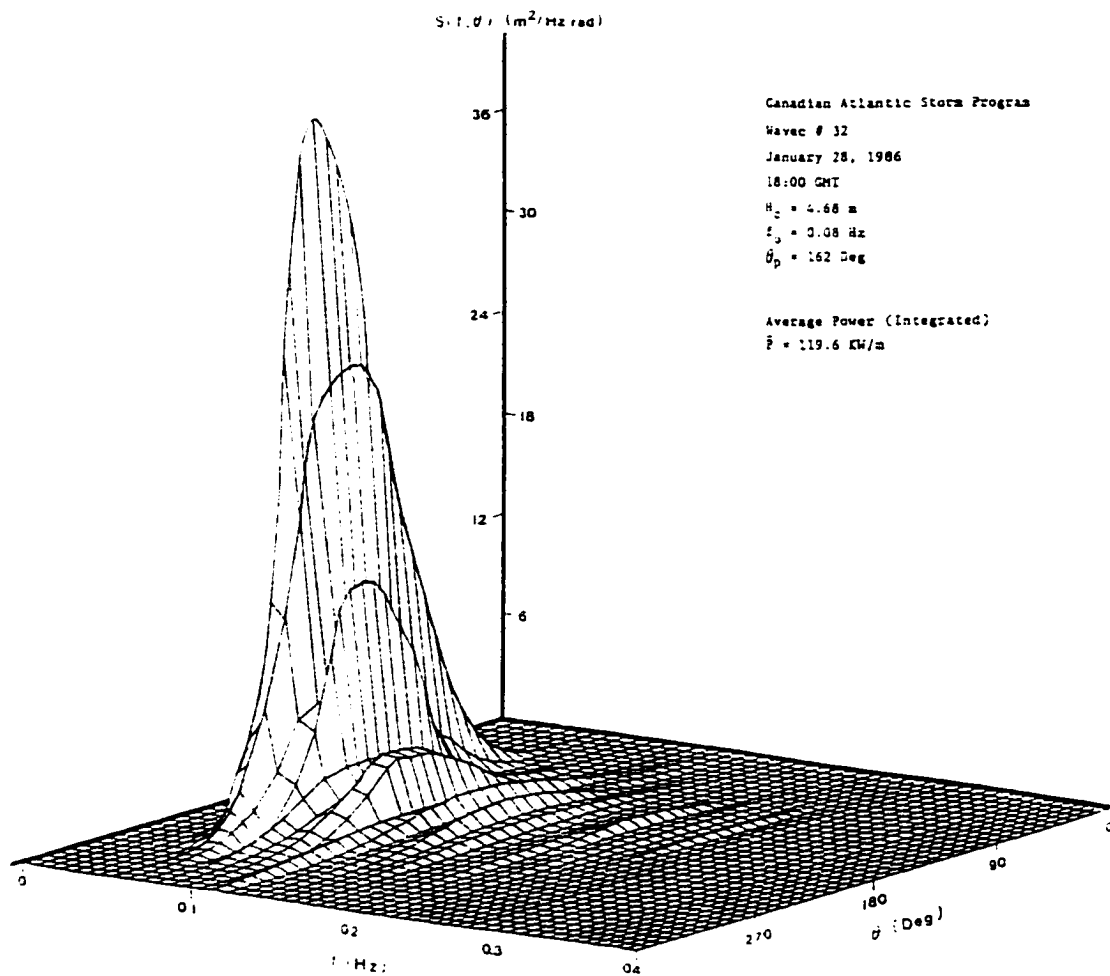
Figure 2.2. 3-Dimensional Directional Wave Energy Spectrum for the Period
18:00-24:00 GMT, January 28, 1986 (Unpublished data obtained
from the Canadian Atlantic Storm Program (1986).)
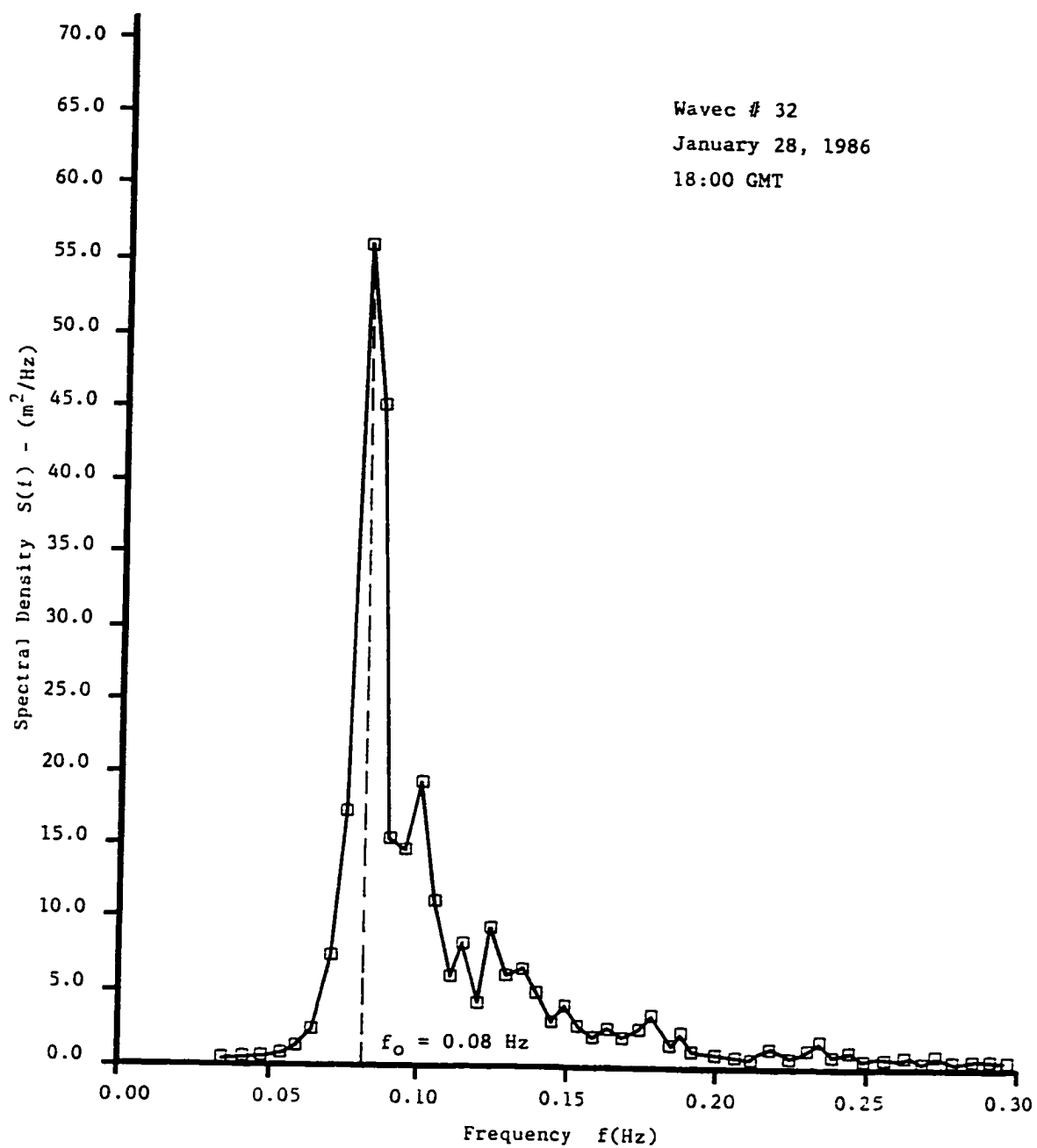
Figure 2.3. Frequency Wave Energy Spectrum for the Period 18:00-24:00 GMT, January 28, 1986 (Data obtained from the Canadian Atlantic Storm Program (1986).)
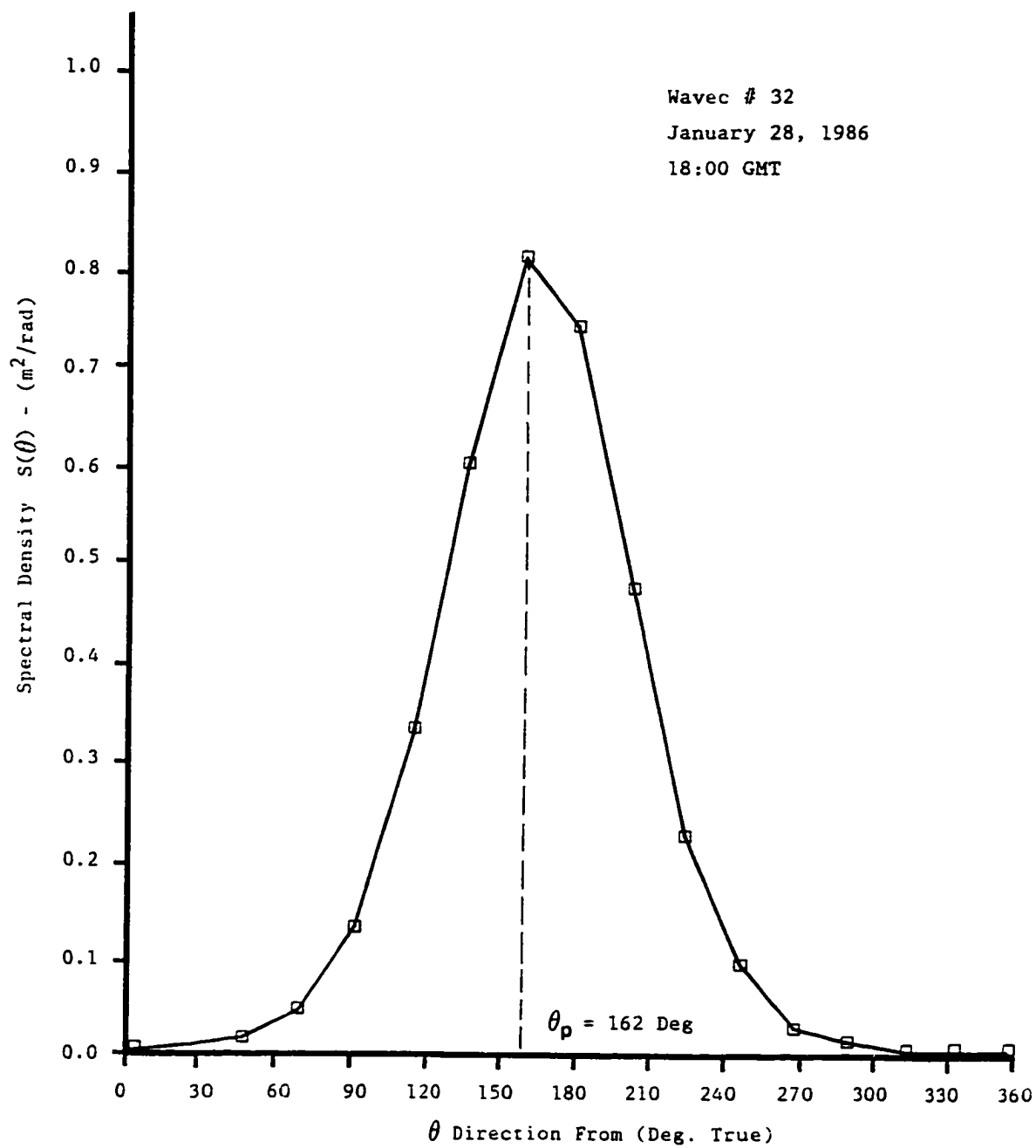
Figure 2.4. Directional Wave Energy Spectrum for the Period 18:00-24:00 GMT,
January 28, 1986 (Data obtained from the Canadian Atlantic
Storm Program (1986).)

In many cases, spectral wave data in the form of S(f) and S(f,θ) are unavailable and alternative methods must be used to determine the average wave power in a random sea. These methods are only approximations to average wave power and incorporate constant statistical wave parameters as being representative of random wave distributions. Statistical parameters of wave height are often represented by the significant wave height, $H_{1/3}$, defined as the average of the highest one-third waves, $H_{z_{1/3}}$ the average of the highest one-third of the zero up-crossing wave heights and the characteristic wave height, H_c, defined as 4 times the square root of the area under the spectral density function. The statistical wave period parameters are the peak period, T_p, which represents the wave period of maximum spectral density, T_z, the average zero crossing period and average periods obtained from spectral moments given by

$$T_{m_{01}} = \frac{m_o}{m_1} \tag{2.34}$$

$$T_{m_{02}} = \sqrt{\frac{m_o}{m_2}} \tag{2.35}$$

where m_n are the moments of the spectral density function. Another statistical average wave period commonly used in the literature for defining average wave power (Pontes et al. (1995), Count et al. (1983), Funke and Mansard (1979), and others) is the energy period T_e defined by

$$P = \frac{\rho g^2}{4\pi} \int_0^\infty \frac{S(f)}{f} df = \frac{\rho g^2}{4\pi} m_o T_e = \frac{\rho g^2}{64\pi} H_c^2 T_e \tag{2.36}$$

The use of statistical parameters in determining approximate values for average wave power are summarized by Mogridge (1980) and given in Table 2.2 for transitional and deep water conditions. For comparative purposes, the method developed by Baird and Mogridge (1976) and Funke and Mansard (1979) is referred to as Method 1.

The approximate methods given in Table 2.2 are similar to the linear approximation for wave power derived in Section 2.2 with the exception of the statistical parameters for wave height and period and the proportionality factor $\rho g^2/64\pi$. By assuming a Rayleigh distribution with a narrow-banded wave spectrum, the characteristic wave height is defined by

$$H_c = 4\sqrt{\overline{\eta^2(x,y,t)}} \qquad (2.37)$$

or

$$H_c^2 = 16 \sum_{i=1}^{\infty} \frac{(\alpha_o)_i^2}{2} = 2 \sum_{i=1}^{\infty} H_i^2 \qquad (2.38)$$

Method 2 is determined by substituting equation 2.38 into Equation 2.24 and assuming T_i to be constant and equal to the peak period (T_p). Methods 3 through 7 are obtained by replacing the characteristic wave height and peak period in Method 2 by various pairs of statistical wave height and period parameters and assuming the proportionality factor to be the same.

Table 2.2. Methods for the Determination of Average
Wave Power in a Random Sea State

METHOD	TRANSITIONAL WATER	DEEP WATER
Method #1	$\dfrac{\rho g^2}{4\pi} \int \dfrac{S(f)}{f} \left[1 + \dfrac{2k_f h}{\sinh 2k_f h} \right] \tanh k_f h\, df$ $\dfrac{\rho g^2}{4\pi} \int \int \dfrac{S(f,\theta)}{f} \left[1 + \dfrac{2k_f h}{\sinh 2k_f h} \right] \tanh k_f h\, d\theta df$	$\dfrac{\rho g^2}{4\pi} \int \dfrac{S(f)}{f}\, df$ $\dfrac{\rho g^2}{4\pi} \int \int \dfrac{S(f,\theta)}{f}\, d\theta df$
Method #2	$\dfrac{\rho g^2}{64\pi} H_c^2 T_p \left[1 + \dfrac{2k_p h}{\sinh 2k_p h} \right] \tanh\, k_p h$	$\dfrac{\rho g^2}{64\pi} H_c^2 T_p$
Method #3	$\dfrac{\rho g^2}{64\pi} H_{1/3}^2 T_p \left[1 + \dfrac{2k_p h}{\sinh 2k_p h} \right] \tanh\, k_p h$	$\dfrac{\rho g^2}{64\pi} H_{1/3}^2 T_p$
Method #4	$\dfrac{\rho g^2}{64\pi} H_{z1/3}^2 T_z \left[1 + \dfrac{2k_z h}{\sinh 2k_z h} \right] \tanh\, k_z h$	$\dfrac{\rho g^2}{64\pi} H_{z1/3}^2 T_z$
Method #5	$\dfrac{\rho g^2}{64\pi} H_c^2 T_{m01} \left[1 + \dfrac{2k_{m01} h}{\sinh 2k_{m01} h} \right] \tanh\, k_{m01} h$	$\dfrac{\rho g^2}{64\pi} H_c^2 T_{m01}$
Method #6	$\dfrac{\rho g^2}{64\pi} H_c^2 T_{m02} \left[1 + \dfrac{2k_{m02} h}{\sinh 2k_{m02} h} \right] \tanh\, k_{m02} h$	$\dfrac{\rho g^2}{64\pi} H_c^2 T_{m02}$
Method #7	$\dfrac{\rho g^2}{64\pi} H_c^2 T_e \left[1 + \dfrac{2k_e h}{\sinh 2k_e h} \right] \tanh\, k_e h$	$\dfrac{\rho g^2}{64\pi} H_c^2 T_e$

Spectral wave data from Osborne Head, Nova Scotia is used as an example for determining average wave power by the various methods listed in Table 2.2. Figure 2.5 presents the one-dimensional wave energy spectrum for the northeastern storm on October 30, 1991. The figure presents a complicated broad-banded spectra with numerous peaks of energy at various frequencies. Also shown are the theoretical Pierson-Moscowitz (1964), Scott (1965).
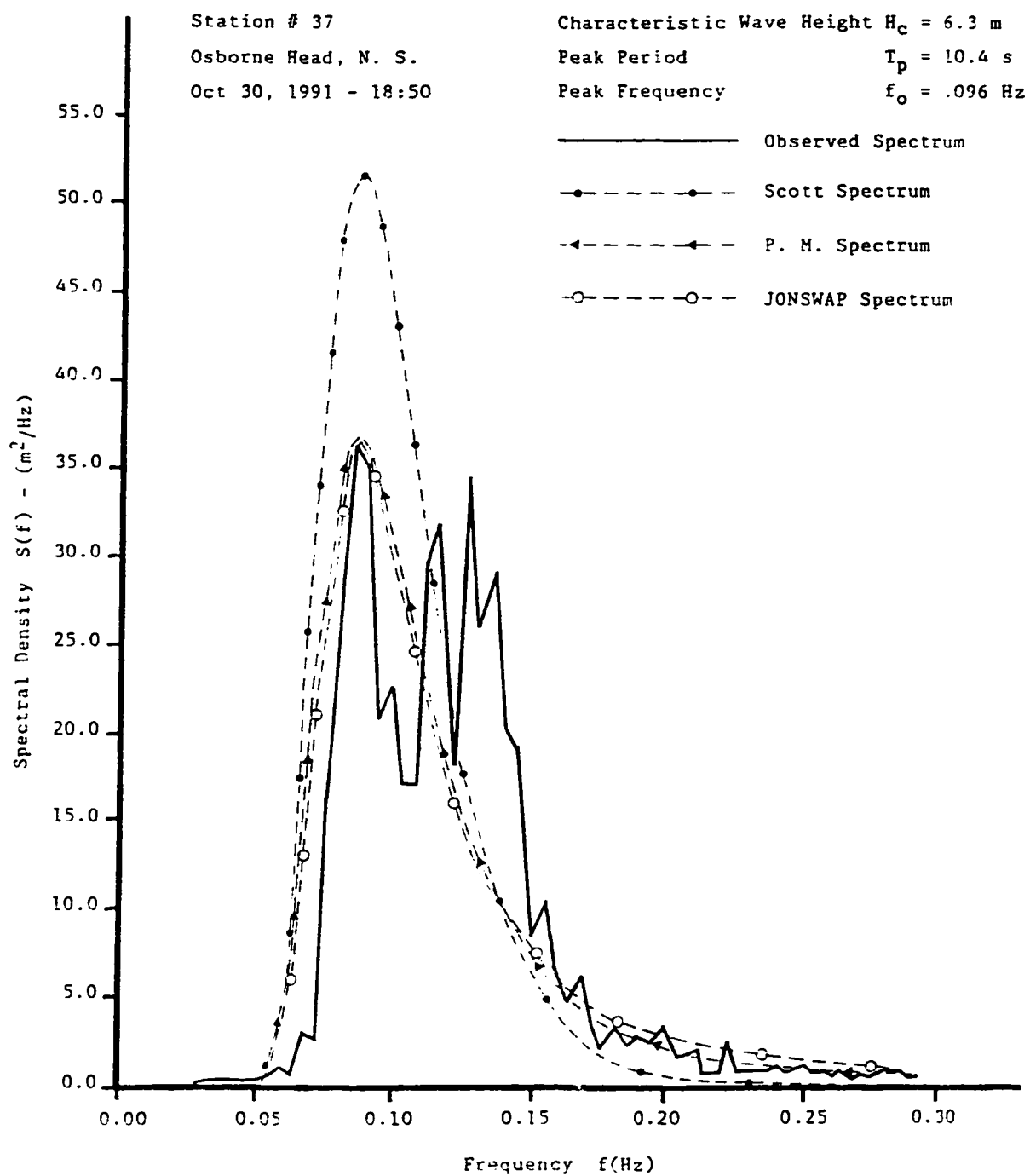
Figure 2.5. Wave Energy Spectrum for Osborne Head, NS (MEDS, 1991)).

JONSWAP spectra (Hasslemann et al., 1973) which are described in Table 2.1. The average wave power determined by the seven methods, with the exception of Methods 3 and 4, are listed in Table 2.3. The statistical wave parameters required for Methods 3 and 4 must be determined by the free-surface elevation time-series which was not available for this spectrum.

Although Methods 2 through 7 are approximate methods, the average wave power values give reasonably good approximations to the Method 1 value of 175.4 kW/m. The average wave power values for the theoretical spectra were determined by substituting the analytical spectra density functions (S(f)) into Method 1. Methods for determining average wave power in a random sea by a probabilistic approach are described in Chapter 3.

2.5   Determination of Seasonal and Long-Term Wave Power Averages

To assess the potential for wave energy extraction at nearshore or offshore locations, a wave data collection program to measure the short and long-term temporal variability of ocean wave power is essential. Variations in average wave power of over 1-Megawatt per metre for severe storm conditions to less than 10 Kilowatts per metre during fair weather conditions are not uncommon. Seasonal or long-term averages of ocean wave power are the most common deterministic values for estimating the magnitude of ocean wave power. Seasonal wave power estimates give insight into the magnitude and duration of wave power levels from month to month and typically shows a pattern of relatively low average wave power for the summer months and high average power levels during winter months. Because historical wave data is often in the form of wave records of 20-minute durations every 3-hours, a large number of calculations are required to estimate the long-term temporal variability of average wave power. By applying the

Table 2.3. Average Wave Power Values for the Osborne Head
Wave Spectrum of October 30, 1991

Location:	
Station #37	October 30, 1991
Osborne Head, Nova Scotia	18:50 GMT

Wave Spectra Characteristics:	
Characteristic Wave Height (H_c)	6.30 m
Peak Period (T_p)	10.40 sec
Peak Frequency (f_o)	0.096 sec^{-1}

Moments:	
m_{-1}	21.205
m_0	2.475
m_1	0.337
m_2	0.052

Average Periods:	
T_{m01}	7.34 sec
T_{m02}	6.90 sec
T_e	8.56 sec

Average Power:	
Method #1	175.4 kW/m
Method #2	194.2 kW/m
Method #3	———————
Method #4	———————
Method #5	167.9 kW/m
Method #6	159.8 kW/m
Method #7	190.1 kW/m
Scott Spectra	225.1 kW/m
P.M. Spectra	179.4 kW/m
JONSWAP Spectra	178.3 kW/m

spectral approximation (Method 1) to each wave energy spectrum of constant duration, the long-term average wave power can be determined by

$$P_{n-year} = \frac{1}{N} \sum_{i=1}^{N} \frac{\rho g^2}{4\pi} \int_0^\infty \frac{S(f)}{f} \left[1 + \frac{2kh}{\sinh 2kh} \right] \tanh kh \, df \qquad (2.39)$$

where N equals the total number of wave energy spectrums for the n years of data analyzed. Approximately 3,000 wave energy spectra of 3-hour duration need to be analyzed to determine the average wave power for 1-year.

An alternative approach, which reduces the computational requirement greatly, is to graphically represent the number of observations of wave spectra within a particular range of statistical wave heights and periods by a scatter diagram. As an example, twenty years (1970-1990) of statistical wave data in the form of characteristic wave height (H_c) and peak period (T_p) from Osborne Head, Nova Scotia, has been analyzed to determine the seasonal and long-term wave power averages. The H_c and T_p values were computed directly from the wave spectrum for measured wave records at intervals of 3-hours.

Figure A.1 in Appendix A presents the scatter diagram of characteristic wave height and peak period for 20-years of wave data at Osborne Head, Nova Scotia. A total of 56,600 observations of 3-hour duration are tabulated within H_c and T_p intervals of 0.3048 metres (1 foot) and 1 second, respectively. Baird and Mogridge (1976) have analyzed 3-years (1970-1973) of wave data from Western Head, Nova Scotia and have presented their results in a scatter diagram of the same form. For comparative purposes, their method of determining long-term average wave power has been adopted in the following calculations. By expressing the mean value of the characteristic wave height and peak period in the given ranges considered in the scatter diagram

by H_{c_i} and T_{p_j}, where i and j represent the rows and columns of the scatter diagram, respectively, the expression for average wave power in a given element can be expressed by

$$P_{ij} = \frac{\rho g^2}{64\pi} H_{c_i}^2 T_{p_j} \qquad (2.40)$$

If a_{ij} represents the number of observations in a given element of the matrix and N_{tot} is the total number of observations, then each element in the matrix contains the average wave power given by $P_{ij} a_{ij}/N_{tot}$. Figure A.2 in Appendix A presents the scatter diagram of average wave power for the 20 years of wave data at Osborne Head, Nova Scotia. The average wave power is then determined by

$$P_{n-year} = \sum_{j=1}^{m} \sum_{i=1}^{k} \frac{P_{ij} a_{ij}}{N_{tot}} \qquad (2.41)$$

for n years of data analyzed, and m and k are the total number of columns and rows, respectively. By summing the total number of elements in the scatter diagram and correcting for shallow water effects, the 20-year average wave power for Osborne Head, Nova Scotia is estimated at 15.8 kW/m. A similar value for average wave power of 12.1 kW/m has been determined for Western Head, N.S. by Baird and Mogridge (1976).

The seasonal average wave power for Osborne Head, Nova Scotia has been determined by tabulating the 20-years of wave data in monthly scatter diagrams. Figure 2.6 presents the seasonal average wave power for Osborne Head, Nova Scotia. It is apparent from the figure that the typical pattern of high average wave power during the winter months and low average wave power for the summer months exists for Eastern Canada. In fact, the average power levels during winter months are five to six times greater than summer months.
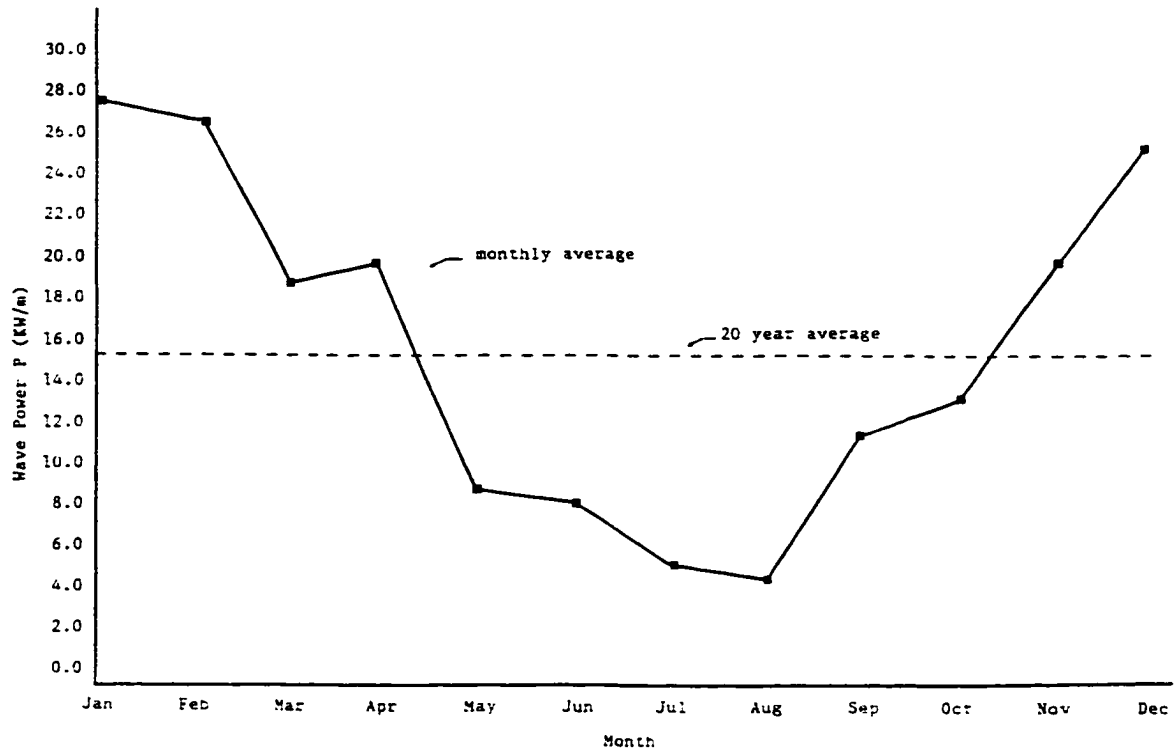
Figure 2.6. Seasonal Average Wave Power for Osborne Head, Nova Scotia (1970-1990)

CHAPTER 3

PROBABILISTIC METHODS FOR THE DETERMINATION OF
WAVE POWER IN A RANDOM WAVE SEA STATE

3.1   The Development of Two Probabilistic Models for Wave Power

As described in the previous chapter, numerous methods exist for the approximation of

average wave power in a random wave sea state. These methods utilize statistical parameters of

the wavefield (i.e. H_c, $H_{1/3}$, $T_{m_{01}}$, $T_{m_{02}}$, T_p) which can be determined by spectral moments of

the wave energy spectrum or direct measurements of the free surface elevation time series.

Because these methods are only approximations of the average wave power, considerable errors

may arise if applied outside the bounds of the assumed conditions. Mansard (1978) carried out

a comparative study showing these different methods for evaluating average wave power for five

energy spectra along the Canadian East Coast and the errors of Methods 2 through 6 relative to

Method 1 were shown to be as high as 43%. There has been considerable spread in the estimated

values of wave power in the oceans using the existing deterministic predictors. The methods

have generally used a single value to represent the physical parameters of interest (e.g. root-mean

square or significant wave height (H_{rms}, $H_{1/3}$) and average or peak wave period ($T_{m_{01}}$, T_p)).

Substitution of these average values into a general equation of wave power does not necessarily

produce corresponding average values of wave power. There is, in fact, considerable variation

in the physical parameters of relevance in wave power and a single deterministic value is most

often not an appropriate value for describing a wave parameter. For example, the wave height

is better described by a Rayleigh distribution, and wave height and period can be related by Longuet-Higgins (1983) joint probability density function. Therefore, it may prove to be more effective to describe these physical parameters as representative distributions rather than mean values when estimating wave power.

In this chapter, two probabilistic models of varying complexity are developed for wave power based on theoretical probability density functions of wave heights (pdf(H)) and wave heights and periods (pdf(H,T)). These random variables will be transformed to the probability density functions of wave power (pdf(P)) by establishing the functional relationship between H, T, and P. The resultant probability distributions of wave power not only allows one to predict the probability that power exceeds a certain level, but also allows for the determination of probabilistic predictions of wave power such as the average (P_l) and averages of the highest one-third $(P_{l/3})$ and one-tenth $(P_{l/10})$ wave power values. These various statistical averages, computed using the distributions of physical parameters, can then be compared with previous methods of estimating average wave power with single values of the input physical parameter. The probabilistic models are also verified with wave spectra data obtained from wave buoys in the nearshore and offshore region of the Canadian Atlantic and Pacific Coasts.

3.2   Theoretical Probability Distributions of Wave Heights and Periods

Although numerous theories have been developed to describe linear and non-linear regular waves, it is important to recognize that regular waves are almost non-existent in the real ocean. Wind-generated disturbances of different intensities, locations, and directions, produce exceedingly complicated random waves with highly irregular and nonrepeatable sea surfaces.

Longuet-Higgins (1951) showed that the Rayleigh probability distribution for the amplitude of sound waves derived from many independent sources compared reasonably well with the observed distribution and theoretical relations for wave heights in the ocean. Rayleigh's probability density function for wave height (pdf(H)) is described according to

$$pdf(H) = \frac{2H}{H_{rms}^2} \exp \left\{-\left[\frac{H^2}{H_{rms}^2}\right]\right\} \tag{3.1}$$

where H and H_{rms} are the wave height and root-mean square wave height, respectively.

Longuet-Higgins (1983) realized, however, that waves in the real ocean possess a random behaviour in both wave height and period. This brought about the development of his well-known joint probability density function for normalized wave height and period pdf (R,τ) which can be expressed by

$$pdf(R,\tau) = C_1 \frac{R^2}{\tau^2} \exp \left\{-R^2[1 + \frac{1}{v^2} (1-\frac{1}{\tau})^2]\right\} \tag{3.2}$$

where

R   = Normalized Wave Height = H/H_{rms} = $H/\sqrt{8m_0}$

τ = Normalized Wave Period = T/T_{m01} = $T \ m_1/m_0$

C_1 = Constant Coefficient = $4\pi^{-1/2}v^{-1}[1+(1+v^2)^{-1/2}]^{-1}$

v   = Bandwidth parameter = $[m_0m_2/m_1^2-1]^{1/2}$

m_0 = Area Under the Measured Spectrum

m_1,m_2 = First and Second Moments of the Spectrum

The derivations for both of these distributions invoke the assumptions that waves possess a Gaussian distribution with a narrow-banded spectral density function. These probability distributions have been verified extensively by researchers and were found to represent random wave sea conditions very well.

Figure 3.1 presents Longuet-Higgins joint probability density function for normalized wave height and period for a spectral width parameter ν of 0.4. In the real ocean, the spectral width parameter can vary between 0.1 to 0.7, with the majority of spectra in the range of 0.2 to 0.6. As can be seen from this figure, a high density of normalized wave heights are close to the mean wave period (i.e. $\tau = 1.0$). Longuet-Higgins also found a statistical dependence between normalized wave height and period such that large waves occur with a high period. Obviously this must be the case in the real ocean because large waves would otherwise become unstable and break.
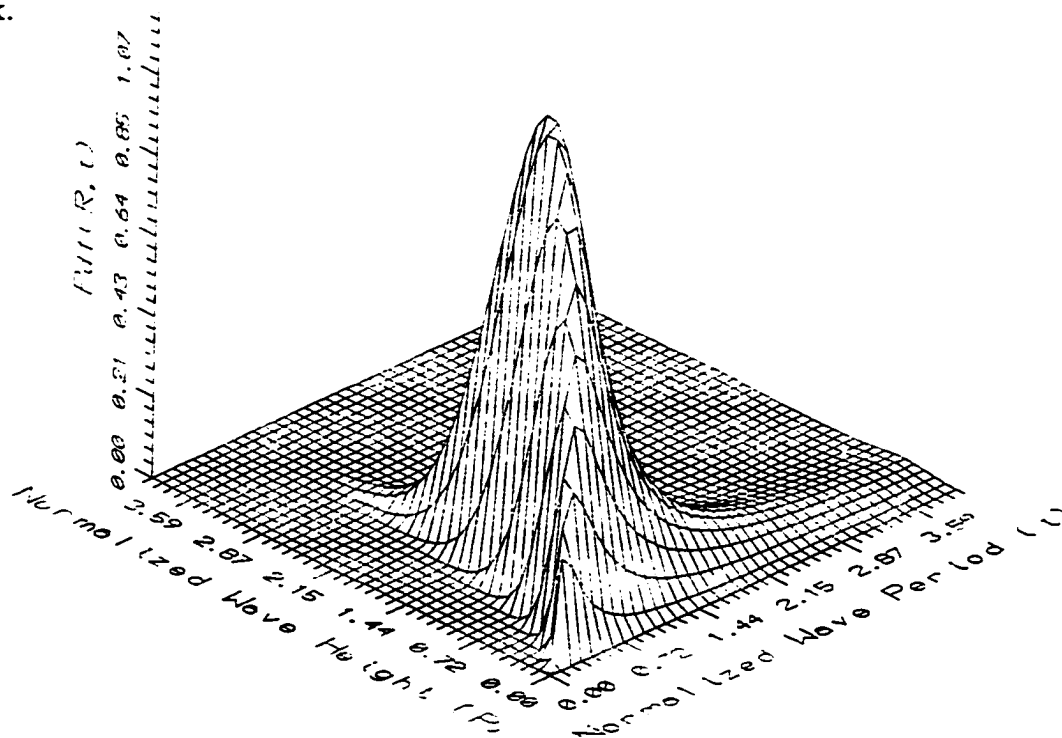
Figure 3.1. Longuet-Higgins Joint Probability Distribution of Normalized Wave Height and Period (Spectral Width Parameter, $\nu=0.4$)

3.3   Standard Transformation of Random Variables

Based upon the two theoretical probability distributions described in the previous section and applying a standard transformation of random variables for a given functional relationship (described in the subsequent section), probability density functions of wave power can be derived.

In order to develop probability density functions of wave power for the two models, a standard transformation of random variables is applied. The transformation is given by (Walpole eand Myers (1978))

$$(X_1, X_2, ... X_N) = [pdf \; (Y_1, Y_2, ... Y_N)] \cdot |J| \tag{3.3}$$

$$Y_1 = h_1(X_1, X_2, ... X_N)$$
$$Y_2 = h_2(X_1, X_2, ... X_N)$$
$$\cdot \qquad \cdot \quad \cdot \quad \cdot \qquad \cdot$$
$$\cdot \qquad \cdot \quad \cdot \quad \cdot \qquad \cdot$$
$$Y_N = h_n(X_1, X_2, ... X_N)$$

where $|J|$ is the Jacobian matrix expressed as

$$|J| = \begin{vmatrix} \partial Y_1/\partial X_1 & \partial Y_1/\partial X_2 & \ldots & \partial Y_1/\partial X_N \\ \partial Y_2/\partial X_1 & \partial Y_2/\partial X_2 & \ldots & \partial Y_2/\partial X_N \\ \cdot & \cdot & & \cdot \\ \cdot & \cdot & & \cdot \\ \partial Y_N/\partial X_1 & \partial Y_N/\partial X_2 & \ldots & \partial Y_N/\partial X_N \end{vmatrix} \tag{3.4}$$

and h_n is the functional relationship of the random variables X_N and Y_N.

3.4 Formulation of the Model for One-Random Variable - Model A

The first model (Model A) assumes Rayleigh's probability density function for wave height (pdf(H)) with constant wave period (T_{m01}) to represent the wave conditions. The pdf(H) is transformed to the probability density function of wave power (pdf(P)) by knowing the functional relationship between wave height (H) and wave power (P). For simplicity, H is normalized by letting

$$R = H/H_{rms} \qquad (3.5)$$

Therefore, the probability density function of normalized wave height (pdf(R)) can be expressed by

$$pdf(R) = [pdf(H)]_{H=h(R)} \cdot |J| \qquad (3.6)$$

Because only one random variable changes, the Jacobian matrix becomes $|\partial H/\partial R|$ and the probability density function is transformed to

$$pdf(R) = \left[\frac{2H}{H_{rms}^2} \exp\left\{-\left\{\frac{H^2}{H_{rms}^2}\right\}\right\}\right]_{H=H_{rms}R} \cdot |\partial H/\partial R| \qquad (3.7)$$

and

$$|\partial H/\partial R| = H_{rms} \qquad (3.8)$$

which yields

$$pdf(R) = 2R \exp{-R^2} \qquad (3.9)$$

Figure 3.2 depicts the probability density function of normalized wave height.

```
1.00

0.75

pdf(R)  0.50                                    2·R·exp(- R²)

0.25

0.00
        0.0    0.5    1.0    1.5    2.0    2.5    3.0
```

Normalized Wave Height R = H/H_rms
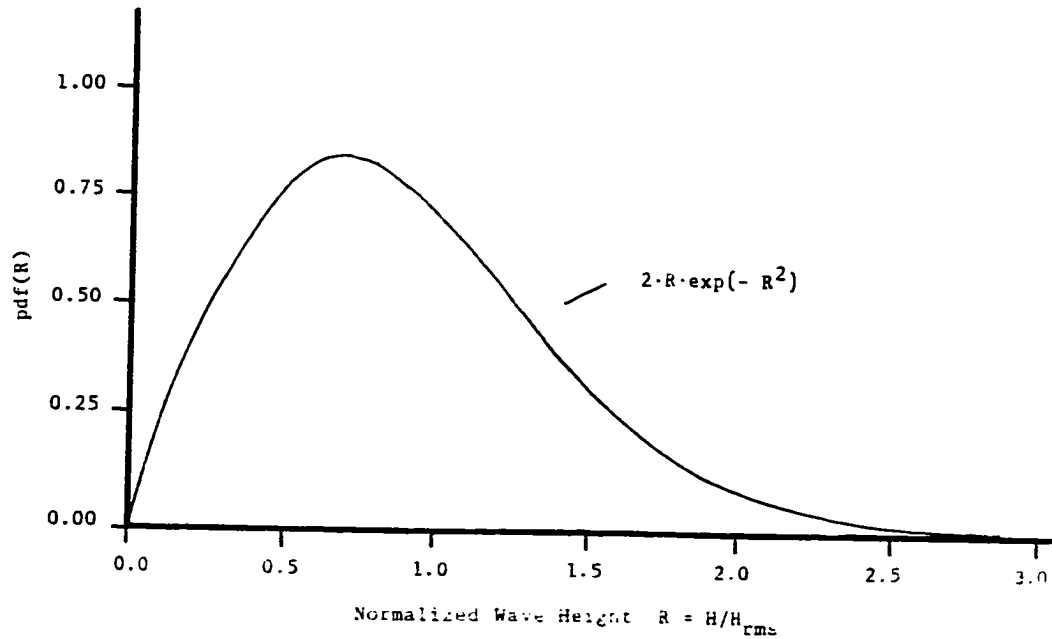
Figure 3.2. Probability Density Function of Normalized Wave Height (pdf(R))

The functional relationship between the random variables H,T and P is based upon the linear wave theory approximation derived in Section 2.2 and expressed

$$P = \frac{\rho g^2}{32\pi} H^2 T \qquad (3.10)$$

For Model A, the wave height in the above expression is normalized by the root-mean square wave height (H_{rms}) and wave period is assumed to be constant. Therefore, the normalized wave power (P_N) is given by

$$P_N = \frac{P}{(\frac{\rho g^2}{32\pi} H^2_{rms} T_{m01})} = R^2 \qquad (3.11)$$

and the pdf(R) can be transformed to the pdf(P_N) by the expression

$$\text{pdf}(P_N) = [\ \text{pdf}(R)\ ]_{R=P_N^{1/2}} \cdot |\partial R/\partial P_N| \tag{3.12}$$

where

$$|\partial R/\partial P_N| = \frac{1}{2}\ P_N^{-1/2} \tag{3.13}$$

$$\text{pdf}(P_N) = [2R\ \exp{-R^2}]_{R=P_N^{1/2}} \cdot \frac{1}{2}\ P_N^{-1/2} \tag{3.14}$$

which gives

$$\text{pdf}(P_N) = \exp\left(-P_N\right) \tag{3.15}$$

Moments of the $\text{pdf}(P_N)$ can be performed to determine statistical parameters such as the average normalized wave power P_{N_1} or the averages of the highest one-third $P_{N_{1/3}}$ and one-tenth $P_{N_{1/10}}$ normalized wave power values. The average normalized wave power is defined as

$$P_{N_1} = \frac{\int_0^\infty P_N\ \text{pdf}(P_N)\ dP_N}{\int_0^\infty \text{pdf}(P_N)\ dP_N} \tag{3.16}$$

where

$$\int_0^\infty \text{pdf}(P_N)dP_N = \int_o^\infty (\exp{-P_N})\ dP_N = 1.0 \tag{3.17}$$

by definition of a probability density function (i.e. the area under the probability density function must equal 1.0). Therefore

$$P_{N_1} = \int_0^\infty P_N \ (exp-P_N) \ dP_N \qquad (3.18)$$

which can be integrated by parts to yield

$$P_{N_1} = \frac{P_1}{\frac{\rho g^2}{32\pi} H^2_{rms} T_{m_{01}}} = 1.0 \qquad (3.19)$$

where P_1 is the dimensional average wave power, such that

$$P_1 = \frac{\rho g^2}{32\pi} H^2_{rms} T_{m_{01}} \qquad (3.20)$$

For wave heights that are Rayleigh distributed, the root-mean square wave height squared is defined as 8 times the area under the energy spectrum (m_0) or 1/2 times the characteristic wave height squared. Therefore, the above expression for wave power becomes

$$P_1 = \frac{\rho g^2}{64\pi} H^2_c T_{m_{01}} \qquad (3.21)$$

and which is equivalent to one of the expressions for average wave power given by Mogridge (1980). However, model A allows for the determination of not only the average normalized wave power (P_{N_1}) but averages of the highest 1/3, 1/10, or 1/n normalized wave power values. The average of the highest 1/n normalized wave power values is derived in Appendix B and can be expressed as

$$P_{N_{1/n}} = 1 - \ln(1/n) \qquad (3.22)$$

From this equation, the average, average of the highest 1/3 and 1/10 normalized wave power values are 1.00, 2.10, 3. 30, respectively.

3.5   Formulation of the Model for Two Random Variables - Model B

The second model (Model B) incorporates Longuet-Higgins (1983) joint probability density function or normalized wave height and period (pdf(R,τ)). The pdf (R,τ) is transformed to the joint probability density function of normalized wave power and period (pdf(P_N,τ) by knowing the functional relationship between the three random variables, P_N, R, and τ. The random variable τ is then integrated out to obtain the probability density functions of normalized wave power (pdf(P_N)). This model is more realistic than Model A or the other approximate methods described in the previous section because of the physical representation of both wave height and period distributions in a random sea state. Also, the spectral bandwidth parameter, ν, which is a measure of the width of the spectrum, is included in this model. This parameter is a function of the first three moments (m_0, m_1, m_2) of the energy spectrum and therefore leads to a more detailed description of the spectrum than previous models.

The functional relationship between the three normalized random variables (P_N, R, τ) can be written as

$$P_N = \frac{P}{\frac{\rho g^2}{32\pi} H_{rms}^2 T_{m01}} = R^2 \tau \tag{3.23}$$

and applying a standard transformation of random variables, the pdf (R,τ) is transformed to the pdf (P_N,τ) by

$$pdf(P_N,\tau) = [\ pdf(R,\tau)]_{R = h(P_N,\tau)} \cdot |J| \tag{3.24}$$

Because only one random variable changes, the Jacobian matrix $|J|$ becomes

$$|J| = |\partial R/\partial P_N| = \frac{1}{2} \tau^{-1/2} P_N^{-1/2} \qquad (3.25)$$

Therefore

$$pdf(P_N,\tau) = \left[C_1 \frac{R^2}{\tau^2} \exp\left\{-R^2[1+\frac{1}{v^2}(1-\frac{1}{\tau})^2]\right\}\right]_{R=\tau^{-1/2}P_N^{1/2}} \cdot \frac{1}{2}\tau^{-1/2}P_N^{-1/2} \qquad (3.26)$$

and the joint pdf of normalized wave power and period is transformed to

$$pdf(P_N,\tau) = \frac{1}{2} C_1 \frac{P_N^{1/2}}{\tau^{7/2}} \exp\left[-\frac{P_N}{\tau}(1+\frac{1}{v^2}(1-\frac{1}{\tau})^2)\right] \qquad (3.27)$$

The $pdf(P_N)$ is determined by integrating the $pdf(P_N,\tau)$ according to

$$pdf(P_N) = \int_0^\infty pdf(P_N,\tau)d\tau \qquad (3.28)$$

substituting the joint $pdf(P_N,\tau)$ into this expression yields

$$pdf(P_N) = \frac{1}{2}C_1 P_N^{1/2}\int_0^\infty \frac{1}{\tau^{7/2}}\exp\left[-\frac{P_N}{\tau}(1+\frac{1}{v^2}(1-\frac{1}{\tau})^2)\right]d\tau \qquad (3.29)$$

Because no analytic solution exists for the above expression, the integration must be performed numerically. To remove the singularity τ^{-1} we let

$$x = \frac{1}{v}(1-\frac{1}{\tau}) \qquad (3.30)$$

and

$$dx = \frac{1}{v}\frac{1}{\tau^2}d\tau \qquad (3.31)$$

The $pdf(P_N)$ now becomes

$$\text{pdf}(P_N) \;=\; \frac{1}{2}vC_1P_N^{1/2}\int_{-\infty}^{\frac{1}{v}}(1-vx)^{3/2}\,\exp-\!\left[P_N(1-vx)(1+x^2)\right]\!dx \qquad (3.32)$$

The solution to the pdf(P_N) is shown in Figure 3.3 for various spectral bandwidth parameters. Physically, as the spectral bandwidth parameter, v, becomes small, the distribution of wave periods are more peaked about the mean wave period ($T_{m_{01}}$). As v approaches zero, the pdf(P_N) converges to the analytic solution (exp-P_N) of Method A. As v becomes large, the distribution of wave periods becomes wider which allows for a greater probability density of higher P_N values than in Model A. The average normalized wave power for two random variables is determined by the expression

$$P_{N_1} \;=\; \frac{\int_0^{\infty}\int_0^{\infty} P_N\,\text{pdf}(P_N,\tau)\,d\tau dP_N}{\int_0^{\infty}\int_0^{\infty}\text{pdf}(P_N,\tau)\,d\tau dP_N} \qquad (3.33)$$

where

$$\int_0^{\infty}\int_0^{\infty}\text{pdf}(P_N,\tau)d\tau dP_N \;=\; 1.0 \qquad (3.34)$$

by definition of a joint probability density function.

Substituting the pdf(P_N,τ) into equation 3.33 and removing the singularity τ^{-1} by substitution, the average normalized wave power becomes
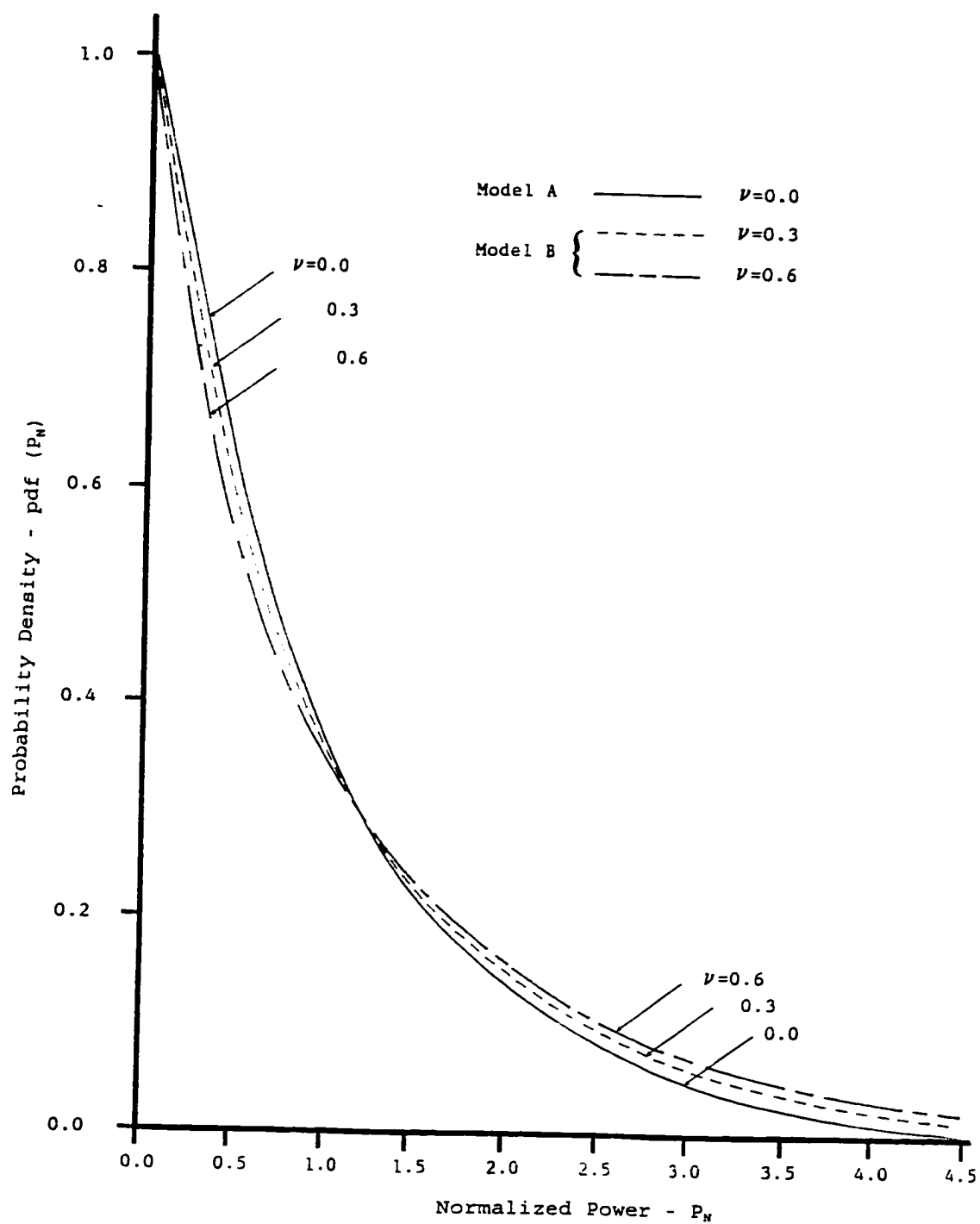
Figure 3.3. Probability Density Function of Normalized Wave Power
for Various Spectral Bandwidth Parameters

$$P_{N_1} = \frac{1}{2}\nu C_1 \int_0^\infty P_N^{3/2} \int_{-\infty}^{1/\nu} (1-\nu x)^{3/2} \exp\left[-P_N(1-\nu x)(1+x^2)\right] dx dP_N \qquad (3.35)$$

and must be numerically integrated over the limits. The final solution for average normalized wave power for Model B is a function of the spectral width parameter (ν) only, and can be expressed as

$$P_{N_1} = \beta(\nu) \qquad (3.36)$$

or, in dimensionalized form, the expression for average power is

$$P_1 = \beta(\nu) \frac{\rho g^2}{32\pi} H_{rms}^2 T_{m01} \qquad (3.37)$$

The numerically integrated function $\beta(\nu)$ as well as the expression for theoretical average wave power for Models A and B are verified in the subsequent section.

3.6   Verification of the Probabilistic Wave Power Models

The random wave analytic model (Model A) and the random wave numerical model (Model B) were tested against actual wave data obtained from wave buoys in the nearshore and offshore region of the Canadian East and West Coasts. A substantial quantity of measured wave data has been collected in a joint program between the Federal Department of Public Works and the Wave Climate Study section of the Marine Environmental Data Service (MEDS). The wave records used in the verification of Models A and B have already been analyzed by MEDS using a fast fourier transform to produce the required wave energy spectrum.

Figure 3.4 presents the verification of average normalized wave power determined by Models A and B with wave energy spectrum data collected by the Canadian Marine Environmental Data Service (Leblond et al. (1982)).

As can be seen from the Figure, $\beta(\nu)$ encompasses the expected bounds (0.2-0.6) of ν for a real random sea. Also shown in the figure is the analytic solution for average normalized wave power determined by Method A. Because Method A assumes a constant wave period for all wave conditions, the average normalized wave power remains constant and equal to 1.0 for all values of ν. As would be expected for Model B, as ν approaches zero, the distribution of wave periods become more peaked about the mean wave period $(T_{m_{01}})$ and the solution to average normalized wave power converges to the solution obtained from Method A.

The verification of Models A and B were carried out by analyzing 14 energy spectra along Canada's East and West Coasts, with characteristic wave heights ranging between 1.0 metre fair weather conditions and 13.0 metre storm conditions. The first three moments (m_0, m_1, m_2) of each energy spectrum were calculated for the required statistical input parameters $(H_{rms}, T_{m_{01}}, \nu)$ of models A and B. The actual average power for the spectra were calculated by Method 1, which integrates discretely over the upper and lower frequency limits of the measured wave energy spectrum.

Although Model A underpredicts all of the actual data points, the range of error is within 5 to 16 percent. The main reason for this error is in the assumption that the wave period is constant for all wave conditions. Model B includes the random behaviour of wave periods and fits the actual data points very well. In fact, of the 14 energy spectrums analyzed, Model B predicts the average normalized wave power within 3.5 percent and an average error of 1.1 percent.
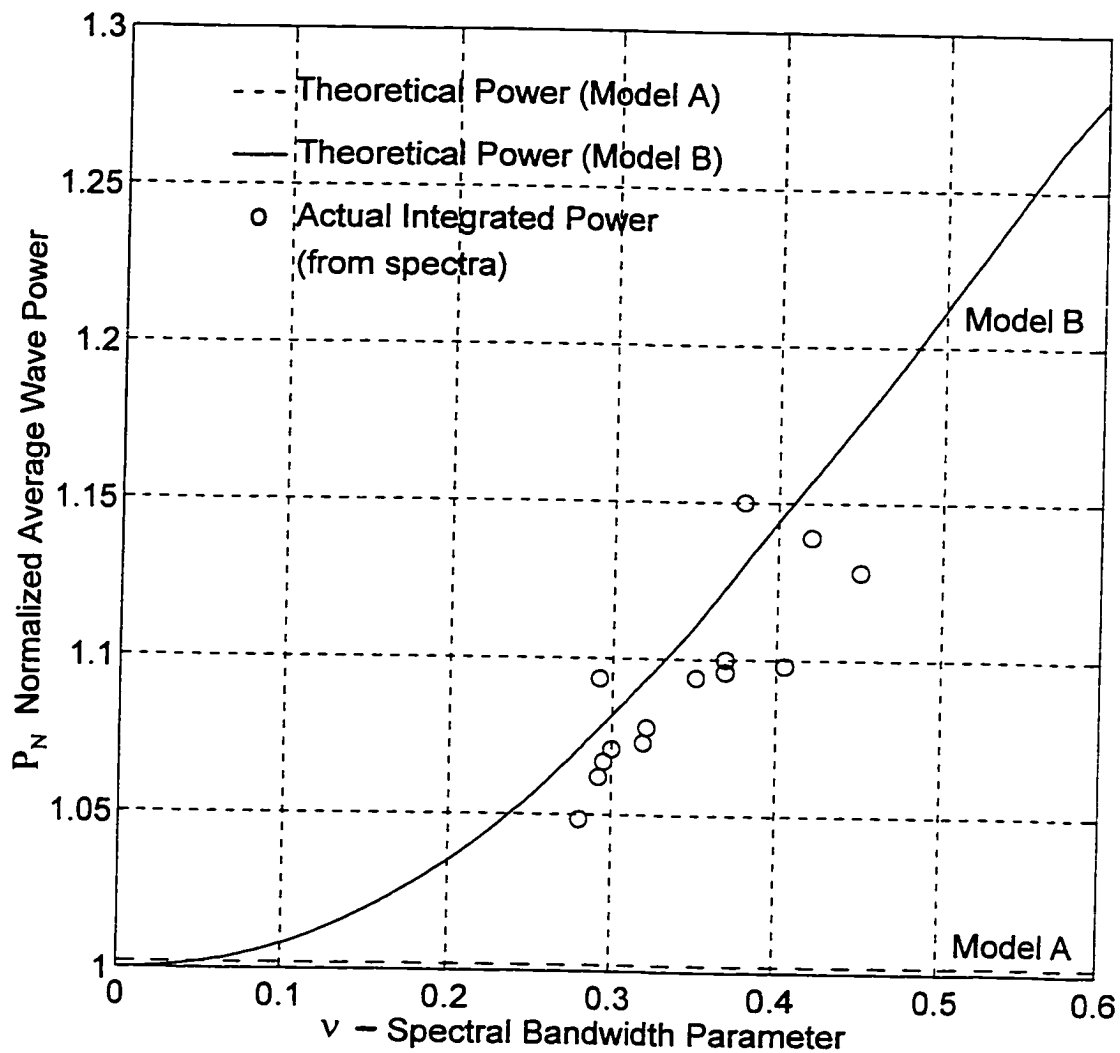
Figure 3.4. Verification of Average Normalized Wave Power for Models A and B (Wave data obtained from MEDS, Leblond et al. (1982).)

Models A and B are also compared in Table 3.1 with the different methods used in Mansard's (1978) comparative study for evaluating wave power in a random sea state. Five different sea states were analyzed along the Canadian East Coast. The spectral bandwidth parameter, ν for models A and B can be calculated by algebraic manipulation of the statistical parameters H_c, T_{m01}, and T_{m02}. The numerically integrated function $\beta(\nu)$ can then be determined from Figure 3.4. This gives all of the parameters necessary for input to the probabilistic models A and B. Mansard uses H_c, the characteristic wave height $(4 \cdot \sqrt{m_0})$, in calculating average wave power for Method 5. For waves that are Rayleigh distributed, the relationship between characteristic wave height and root-mean square wave height is given by $H_{rms}^2 = 1/2 \ H_c^2$. By substituting this equation into the analytical model A for average wave

power, the average wave power calculated by both Method 5 (the most accurate of Mansard's six methods) and Model A are the same. Using Model A however, one can calculate further representative values of wave power such as average of the highest 1/3, 1/10, and 1/n wave power values, thus giving much more information for analysis. Since an even more accurate representation of the wave power characteristics is given by a two parameter probability distribution, this representation, used in Model B, gives an improved value of average wave power than the previous methods, with an error of less than 2 percent. In addition, the average of the highest 1/n wave power values can be determined from a joint probability distribution as well as the probability that wave power exceeds a given level.

Table 3.1. Verification of Average Wave Power For Models A and B
(Data obtained from Mansard (1978)

Station Identification	Gabarus Bay NFLD.	Osborne Head N.S.	Gabarus Bay NFLD.	Coleson Cove N.B.	Sedco J. NFLD.
H_s(m)	1.55	3.08	3.59	5.39	8.82
T_{m01} (sec)	7.29	6.70	8.08	10.27	12.86
T_{m02} (sec)	6.87	6.44	7.63	9.78	12.34
ν	0.364	0.287	0.344	0.322	0.295
β	1.119	1.074	1.106	1.094	1.079
Wave Power [1] (kW/m)	9.26	32.42	54.79	153.99	489.53
Wave Power [2] (kW/m)	10.68	34.42	60.76	177.57	480.53
Wave Power [3] (kW/m)	13.28	35.77	67.72	177.36	502.25
Wave Power [4] (kW/m)	7.88	28.85	45.02	138.57	419.49
Wave Power [5] (kW/m)	8.36	30.41	49.93	142.84	458.27
Wave Power [6] (kW/m)	7.87	29.21	47.15	136.08	439.66
Wave Power [A] (kW/m)	8.36	30.41	49.93	142.84	458.27
Wave Power [B] (kW/m)	9.35	32.66	55.22	156.27	494.47
Diff. $\frac{[2]-[1]}{[1]}$	15.33%	6.17%	10.90%	15.31%	-1.84%
Diff. $\frac{[3]-[1]}{[1]}$	43.37%	10.32%	23.58%	15.18%	2.59%
Diff. $\frac{[4]-[1]}{[1]}$	-14.91%	-11.01%	-17.82%	-10.00%	-14.30%
Diff. $\frac{[5]-[1]}{[1]}$	-9.71%	-6.20%	-8.85%	-7.00%	-6.38%
Diff. $\frac{[6]-[1]}{[1]}$	-15.01%	-9.91%	-13.92%	-11.58%	-10.18%
Diff. $\frac{[A]-[1]}{[1]}$	-9.71%	-6.20%	-8.85%	-7.00%	-6.38%
Diff. $\frac{[B]-[1]}{[1]}$	+1.02%	+0.74%	+0.79%	+1.48%	+1.01%

CHAPTER 4

THREE-DIMENSIONAL MATHEMATICAL MODELLING OF

THE OSCILLATING WATER COLUMN WAVE ENERGY DEVICE

4.1   Introduction

Physically the oscillating water column device is a rigid, hollow, fixed or floating structure open at the immersed side or bottom (depending on the geometric configuration of the device) that traps a volume of air above it (Figure 4.1). The incoming wave field produces an oscillating hydrodynamic pressure distribution causing the internal fluid mass within the device to rise and fall. This oscillation drives the volume of air through a constriction containing an air turbine which is connected to a generator for direct energy conversion. Previous investigators have shown that the entrained fluid mass within the device responds well to both regular and irregular sea states that have frequencies close to the resonant frequency, amplifying the response and ultimately improving the efficiency of the device. However, this amplified response is narrow banded and generally does not respond well to frequencies outside the natural frequency of the device.

In this research, further detail is given into the performance of the OWC device by:

(1)   numerically modelling the fluid structure interaction by the hybrid finite element method;

Wells Air Turbine — — Electrical Generator

Terminator Type
OWC

Air

Water Depth

Seafloor

Wells Air Turbine — — Electrical Generator

Attenuator Type
OWC

Air

Water Depth

Seafloor
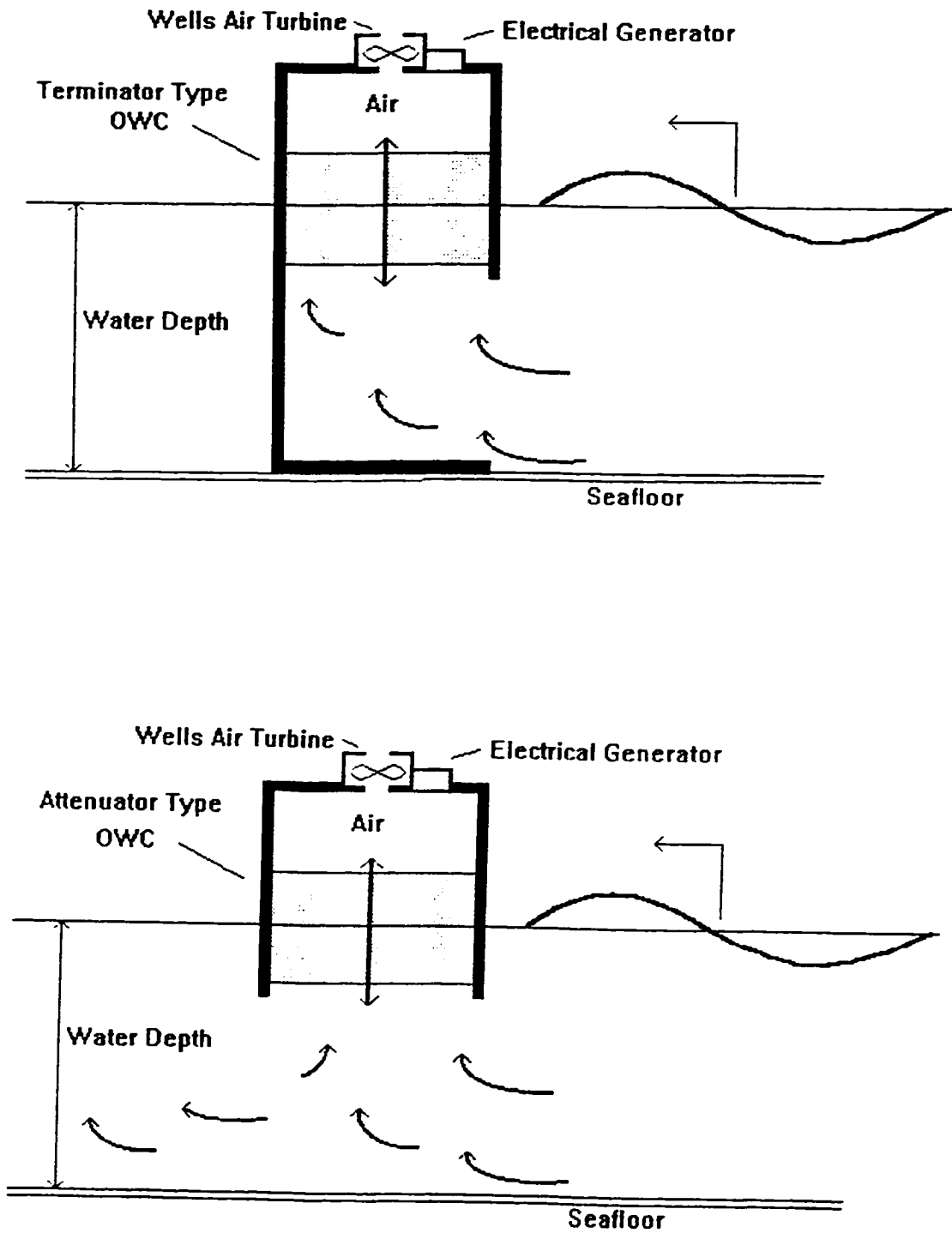
Figure 4.1. Attenuator and Terminator Type Oscillating Water Columns

(2)   determining the effects of various geometrical configurations on the hydrody-

namic coefficients of added mass, radiation damping and diffraction;

(3)   optimizing device performance and determining the natural frequency and peak

performance of the device and variations between device types;

(4)   assessing the effects of wave directionality on device performance and the

variations in frequency and directional bandwidths between device types;

(5)   assessing the device(s) with the most favourable performance in regular seas and

to determine through probabilistic methods (described in Chapter 6), the

performance in random seas with various wave spectra bandwidths; and

(6)   carrying out an experimental program that will supplement and assist in the

verification of the numerical models.

4.2   Development of a Mathematical Model

In this research, a three-dimensional radiation-diffraction finite element model (hybrid

method) and an analytical model are coupled together to describe the physical behaviour of the

OWC device. When excited by an incoming wave field, the entrained mass of fluid within the

oscillating water column device oscillates vertically with a frequency response dependent on the

geometrical configuration of the device, hydrodynamic pressure field, and the applied pressure

at the internal air/water interface.

Numerous researchers (McCormick (1981), Robinson (1982), Watts et al. (1985), Maeda

et al. (1985), and others) have modelled the interior of the OWC as a floating rigid body to

describe the physical behaviour and determine wave power extraction and efficiency. By

replacing the water column with a floating rigid body with the same displaced volume and mass as the fluid, and capable of oscillating vertically in the heave mode due to the excitation of incident waves, an equation of motion can be formulated based on a single force balance of the body.

Evans (1978), Count et al. (1981), Chen and Chen (1987) and Ma (1995) have given a more realistic approximation for the interior of the OWC by modelling the free-surface by a rigid surface condition (rigid plate) of prescribed vertical velocity in response to an incoming wave. It is argued that for long waves the pressure distribution on the interior free-surface reduces to a rigid surface condition. Evans (1981) compared the resonant conditions of rigid body wave energy devices and showed that only slight differences occur for device size/wave length ratios within the range of practical interest, suggesting that the use of such rigid body approximations for OWC devices with internal surface pressures will provide satisfactory results.

Count (1983) and Evans and McIver (1988) also modelled the terminator type OWC by approximating the side opening (below the front submerged wall) as a rigid plate oscillating with prescribed horizontal velocity (i.e.similar to Wavemaker Theory).

Studies involving fixed three dimensional oscillating water columns are limited. Table 4.1 summarizes the theoretical investigations of fixed three dimensional oscillating water columns and the types of devices studied.

Table 4.1

Investigations of Fixed Three-Dimensional Oscillating Water Columns

Date	Author(s)	Type of Device
1974	McCormick	Attenuator
1975	Budal and Falnes	Attenuator
1978	Evans	Terminator
1979	Evans	Attenuator
1980	Budal,Falnes, Kyllingstad and Oltedal	Attenuator
1981	Whittaker, Robinson and Murray	Attenuator/Terminator
1982	Ambli, Bonke, Malmo and Reltan	Multi Resonant
1982	Evans	Attenuator
1982	Robinson	Attenuator
1982	Moody and Elliot	Terminator
1983	Count, Fry, and Haskell	Multi Resonant/Terminator
1985	Sarmento and Falcao	Attenuator/Terminator
1987	Tzong, Wu and Leung	Terminator
1988	McIver and Evans	Multi Resonant
1990	Greenberg	Attenuator
1991	Whittaker	Terminator
1995	Curran et al.	Terminator
1995	Koola et al.	Multi Resonant

In this research, the interior of the oscillating water column is modelled by finite elements and the interior free-surface as a thin rigid plate. The advantage of modelling the interior free-surface as a thin rigid plate is that the radiation condition appropriate to the forced motion of the plate and diffraction condition appropriate to a fixed OWC can be evaluated by well-known ship hydrodynamic theory with the appropriate modifications. In addition, because the hydrodynamic

flow field within the OWC is still modelled as a fluid, the interior fluid/structure interaction will allow for a more accurate determination of the forces on the rigid surface plate.

The fluid forces acting on the heaving plate consist of

(1)   excitation forces due to the incident and diffracted waves;

(2)   hydrodynamic forces due to waves radiated by the motions of the plate;

(3)   hydrostatic forces due to hydrostatic pressures;

(4)   applied forces due to the pressure differential across the turbine

The excitation forces due to the incident and diffracted waves are determined by solving the diffraction problem, while the hydrodynamic inertial and radiation damping forces due to the motion of the plate are calculated from the radiation problem. The hydrodynamic forces due to the motions of the plate are commonly described in terms of added mass and radiation damping coefficients. The hydrostatic force can be described in terms of a hydrostatic restoration coefficient associated with the plate. The applied force due to the extraction of energy from the air turbine/generation system produces an oscillating air pressure on the top face of the plate which is expressed as an additional damping force. Studies (Whittaker et al. (1981), Maeda et al. (1985)) concerning the pressure/air flow ($\Delta P/Q$) characteristics of the Wells self rectifying air turbine have shown a linear relationship between volume air flow and pressure or between velocity of the internal free-surface and force. Recent experimental studies (Curran et al. (1995)) on the performance of the Wells turbine at the operational OWC wave power plant on the Island of Islay, Scotland have verified that this linear relationship exists. Their results show that the linear damping characteristic of the Wells turbine produces a relatively smooth supply of pneumatic power and electrical output. Hence, in the present research, the applied damping force will be assumed to vary linearly with the internal free surface velocity.

The dynamic equation of motion of the oscillating water column is determined by a simple force balance on the rigid plate. Figure 4.2 presents these forces as a free body diagram and the equivalent vibration model of this dynamic system.
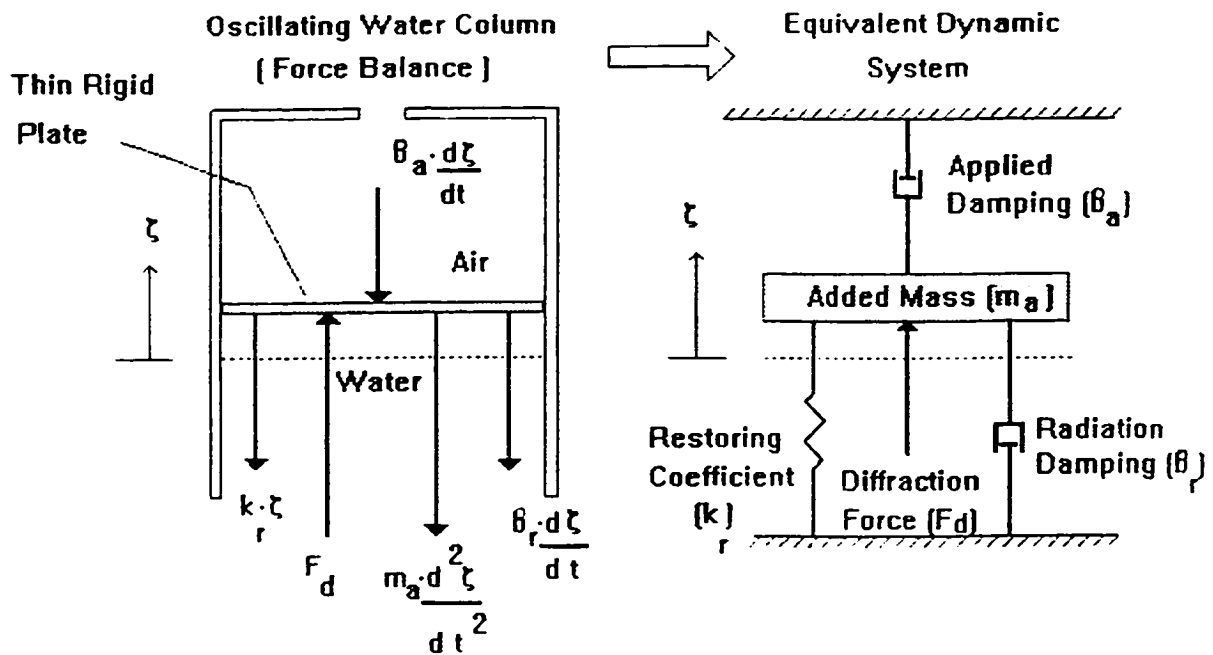
Figure 4.2. Free-Body Diagram and Equivalent Vibration Model
of the Oscillating Water Column

The resulting equation of motion is a linear second order differential equation described by

$$m\frac{d^2\xi}{dt^2} + B_a\frac{d\xi}{dt} + k_r\xi = F_d(t) + F_r(t) \qquad (4.1)$$

where

m	=	mass of thin rigid plate
B_a	=	applied damping coefficient
k_r	=	restoring force coefficient
$F_d(t)$	=	harmonic force due to the scattering of the incident and diffracted wave problem
$F_r(t)$	=	harmonic force due to the radiation wave problem
$\xi, \dfrac{d\xi}{dt}, \dfrac{d^2\xi}{dt^2}$	=	displacement, velocity, and acceleration of the plate

$F_r(t)$ is comprised of the frequency dependent added mass (m_a) and radiation damping (B_r) terms

such that $F_r(t) = -\left(m_a \dfrac{d^2\xi}{dt^2} + B_r \dfrac{d\xi}{dt} \right)$ and the resulting equation of motion becomes

$$(m+m_a)\frac{d^2\xi}{dt^2} + (B_a+B_r)\frac{d\xi}{dt} + k_r\xi = F_d(t) \qquad (4.2)$$

The motion displacement $\xi(t)$ represents a simple harmonic oscillation in the form

$$\xi(t) = \xi_o \sin(\omega t - \psi) \qquad (4.3)$$

where ξ_o is the amplitude of oscillation, ψ is the phase angle between the displacement and the

exciting force and ω is the frequency of the oscillation. Differentiating equation 4.3 with respect

to time and substituting into equation 4.2 gives

$$-(m+m_a)\omega^2\xi_o\sin(\omega t-\psi) + (B_a+B_r)\omega\xi_o\cos(\omega t-\psi) + k_r\xi_o\sin(\omega t-\psi) = F_d\sin\omega t \quad (4.4)$$

where

$$\sin(\omega t - \psi) = \sin \omega t \cos \psi - \cos \omega t \sin \psi$$

$$\cos(\omega t - \psi) = \cos \omega t \cos \psi + \sin \omega t \sin \psi$$

By equating the coefficients of $\sin \omega t$ and $\cos \omega t$, two equations are formulated

$$-(m+m_a)\omega^2 \xi_o \cos \psi + (B_a + B_r)\omega \xi_o \sin \psi + k_r \xi_o \cos \psi = F_d \qquad (4.5)$$

$$(m+m_a)\omega^2 \xi_o \sin \psi + (B_a + B_r)\omega \xi_o \cos \psi - k_r \xi_o \sin \psi = 0 \qquad (4.6)$$

Solving for ξ_o and ψ from these equations gives the following expression for the amplitude of oscillation of the thin rigid plate

$$\xi_o = \frac{F_d}{((k_r - \omega^2(m+m_a))^2 + \omega^2(B_a + B_r)^2)^{1/2}} \qquad (4.7)$$

and phase angle by

$$\psi = \tan^{-1}\left(\frac{\omega(B_a + B_r)}{k_r - \omega^2(m+m_a)}\right) \qquad (4.8)$$

The amplitude response of the oscillating water column resembles the harmonically excited motion of a single-degree of freedom system similar to vibration theory. Where the design of mechanical systems avoid the resonance or natural frequency of the device and to prevent large vibration amplitudes to develop, the oscillating water column device is designed to operate as closely to the resonant frequency as possible. By examining equation 4.7 it can be seen that the maximum amplitude of oscillation occurs when the terms k_r and $\omega^2(m+m_a)$ balance, such that

$$k_r - \omega_n^2(m+m_a) = 0 \qquad (4.9)$$

and the natural frequency, ω_n, of the OWC device is given by

$$\omega_n = \sqrt{\frac{k_r}{m+m_a}} \qquad (4.10)$$

By assuming a rigid plate mass (m) much less than the added mass (m_a), the natural frequency of the OWC device reduces to $\omega_n = \sqrt{k_r/m_a}$. Figure 4.3 depicts a frequency response analysis carried out experimentally in the TUNS wave tank for an attenuator type OWC (with no applied damping) to characterize this amplification and narrow bandwidth of the water column.
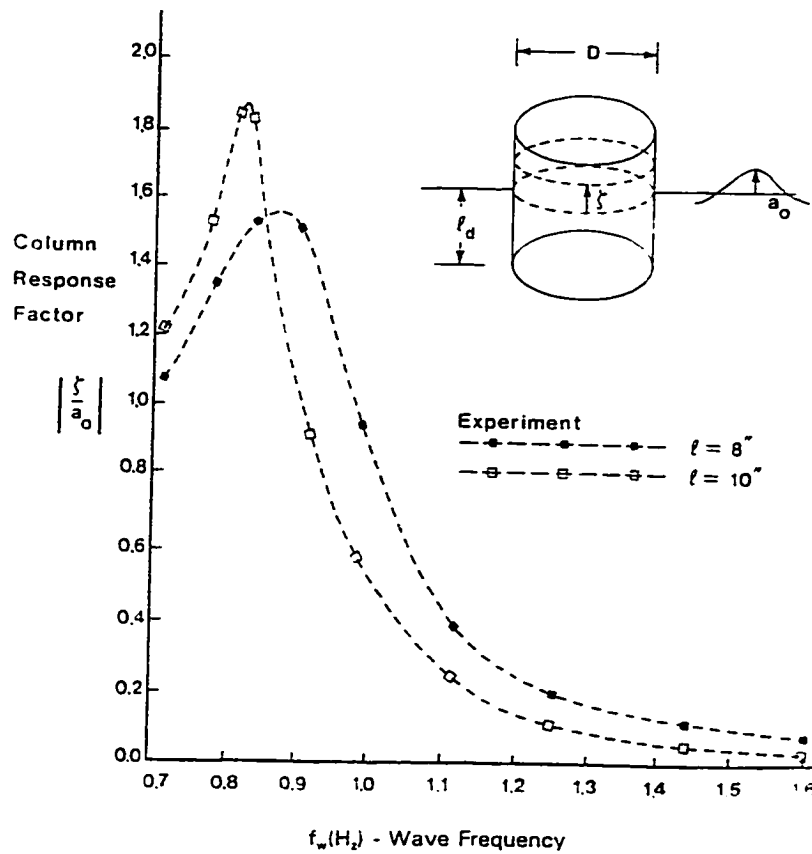
Figure 4.3. Frequency Response of an Attenuator Type OWC

4.3   Determination of Wave Power Extraction

Wave power extraction of the OWC device can be defined mathematically as the product of the applied damping force, $B_a \, d\xi/dt$ (a force on the entrained water column produced by the pressure differential across the turbine), and the velocity of the internal surface, $d\xi/dt$. Accordingly, the instantaneous wave power extraction is described by

$$P_e(t) = \left(B_a \frac{d\xi}{dt}\right) \cdot \left(\frac{d\xi}{dt}\right) = B_a\left(\frac{d\xi}{dt}\right)^2 \qquad (4.11)$$

where the velocity, determined by differentiating the motion displacement, $\xi(t)$, is given as

$$\frac{d\xi}{dt} = -\omega \xi_o \cos(\omega t - \psi) \qquad (4.12)$$

therefore

$$P_e(t) = B_a \omega^2 \xi_o^2 \cos^2(\omega t - \psi) \qquad (4.13)$$

The average power extraction per cycle is given by time-averaging the above equation such that

$$P_e = \frac{1}{\left(\frac{2\pi}{\omega}\right)} \int_0^{\frac{2\pi}{\omega}} P_e(t)dt = \frac{1}{2}B_a \omega^2 \xi_o^2 = \frac{1}{2}B_a \omega^2 \alpha_o^2 \left(\frac{\xi_o}{\alpha_o}\right)^2 \qquad (4.14)$$

where α_o is the wave amplitude. Substituting the expression for ξ_o (Equation 4.7) into Equation 4.14 results in

$$P_e = \frac{\frac{1}{2}B_a \omega^2 F_d^2}{(k_r - \omega^2(m_a))^2 + \omega^2(B_a + B_r)^2} \qquad (4.15)$$

At resonant conditions $k_r - \omega^2(m_a) = 0$ and the expression for average wave power extraction reduces to

$$(P_e)_{res} = \frac{\frac{1}{2}B_a F_d^2}{(B_a + B_r)^2}$$

(4.16)

from which the maximum average power extraction for a device can be determined by optimizing the time-averaged power extraction $(P_e)_{res}$ with respect to the applied damping (B_a) such that

$$\frac{\partial(P_e)_{res}}{\partial B_a} = \frac{\partial}{\partial B_a}\left(\frac{\frac{1}{2}B_a F_d^2}{(B_a + B_r)^2}\right) = 0$$

(4.17)

and exists when the applied damping equals the radiation damping, i.e. $B_a = B_r$. Therefore, the maximum average power extraction can be described by

$$(P_e)_{max} = \frac{1}{8}\frac{F_d^2}{B_a}$$

(4.18)

The determination of the hydrodynamic coefficients of heave added mass (m_a), radiation damping (B_r), and diffraction force (F_d) for various geometrical configurations of the OWC device is carried by a three-dimensional radiation-diffraction finite element model (Hybrid Method) described in the next section. The finite element results coupled together with the analytical model described in this section are used to describe the physical behaviour of the OWC device.

4.4   Radiation-Diffraction Finite Element Method

Two major classes of methods have been developed to solve for the 3-dimensional radiation diffraction effects of waves on complicated structures: (a) Integral Equation Method and (b) Hybrid Finite Element Method.

The method of boundary integral equations involves Green functions that satisfy the governing and boundary equations (with the exception of the body surface boundary equation). An integral equation or system of algebraic equations represented by surface elements are developed for the strengths of singularity on the body surface and by solving for the strengths, a solution to the velocity potential can be obtained through quadrature methods.

The hybrid finite element method uses finite elements to surround the near-field region (including the body surface and bottom boundary) and an analytical expression in the far field region. In this method, the boundary value problem is reformulated in terms of a variational principle which is solved by matching the solutions in the finite element and analytical regions on an artificial cylindrical boundary. All the unknown parameters in both regions can be determined by solving a set of equations simultaneously.

Both methods are powerful tools for solving the radiation diffraction problem for complicated bodies, each with their own advantages and disadvantages for a particular problem application. It has been fairly well documented in the literature (Mei (1978) and Eatock Taylor and Zietsman (1982)) that the boundary integral equation often fails to give finite solutions for certain frequencies. Although these irregular frequencies are generally above the frequency range of engineering interest (Eatock Taylor and Zietsman (1982)), problems may arise for certain complicated body geometries or engineering problems. In addition, curved body surfaces which

are represented by quadrilateral or triangular flat panels allows for leaks between panels which are prevented by either a large number of panels on the body surface or the application of a higher-order element method (Teng and Eatock Taylor (1995)). Count et al. (1983) applied the boundary integral method to the oscillating water column (with projecting front sidewalls) by partitioning the internal OWC surface into small plane elements and assumed that the integrals were constant over these elements. By prescribing a normal velocity on the internal surface, convergent solutions were not obtainable by this method and they attribute this to the rapid variation in velocity potential from the interior and exterior regions of the device. Chen and Chen (1989) and Ma (1995) have applied the boundary integral method to the two-dimensional terminator type OWC and have also avoided partitioning the interior free surface by boundary elements. They solve the scattering problem by separating the computational domain into two regions in which the solutions are matched at the side wall opening (i.e. below the submerged front wall) where the face is described by a boundary element with an unknown source distribution at the centre.

The finite element method has the advantage of modelling complicated structures in finite depth with a relatively small number of elements and, in particular, involve algebraic manipulations with elementary and regular functions (Mei (1978)). However, the main disadvantage of this method is the large computational requirement for applications in deep water. To effectively model deep water conditions (i.e. for linear wave theory the depth of wave influence is approximately half the wavelength) a large number of finite element layers through depth are required, particularly for low frequency waves.

Because the oscillating water column devices modelled in this research are in finite depth, the hybrid finite element method was chosen as the appropriate technique to determine the 3-

dimensional fluid structure interactions. A hybrid finite element program for computing the scattering of waves was developed by Yue et al. (1976). This original version, which was limited to the calculation of diffraction forces only, was modified by Pawlowski (1985) to include the calculation of radiation forces on floating structures. This Radiation Diffraction Finite Element (RDFE) method is used in the present research, with the appropriate modifications to include for the interior OWC fluid and boundary faces, for accurately determining the hydrodynamic coefficients of added mass, radiation damping, and diffraction forces for various OWC geometrical configurations. The theoretical background of the RDFE method developed by Pawlowski is described in the following subsections.

4.4.1 Definition of Domain and Boundaries

The three dimensional linear scattering problem of the oscillating water column device (radiation and diffraction of water waves in finite depth) is solved by means of a hybrid variational formulation. The formulation uses the domains and boundaries of an ideal fluid defined in Figure 4.4 A cartesian coordinate system is defined with the z-axis directed vertically upward and the x and y axes on the free-surface. A cylindrical coordinate system (r,θ,z) is also employed such that the radius r and the angle θ from the x-axis in the xy plane is defined by

$$r = \sqrt{x^2+y^2}$$
$$x = r\cos\theta \qquad y = r\sin\theta$$

(4.19)

The fluid domain D is bounded by the free-surface ∂F, the wetted surface of the rigid body ∂B_a, and the sea bottom ∂B. The sea bottom corresponds to a constant depth h outside an artificial

cylindrical boundary ∂S of radius R and both the wetted surface of the body and the sea bottom are assumed to be impermeable.
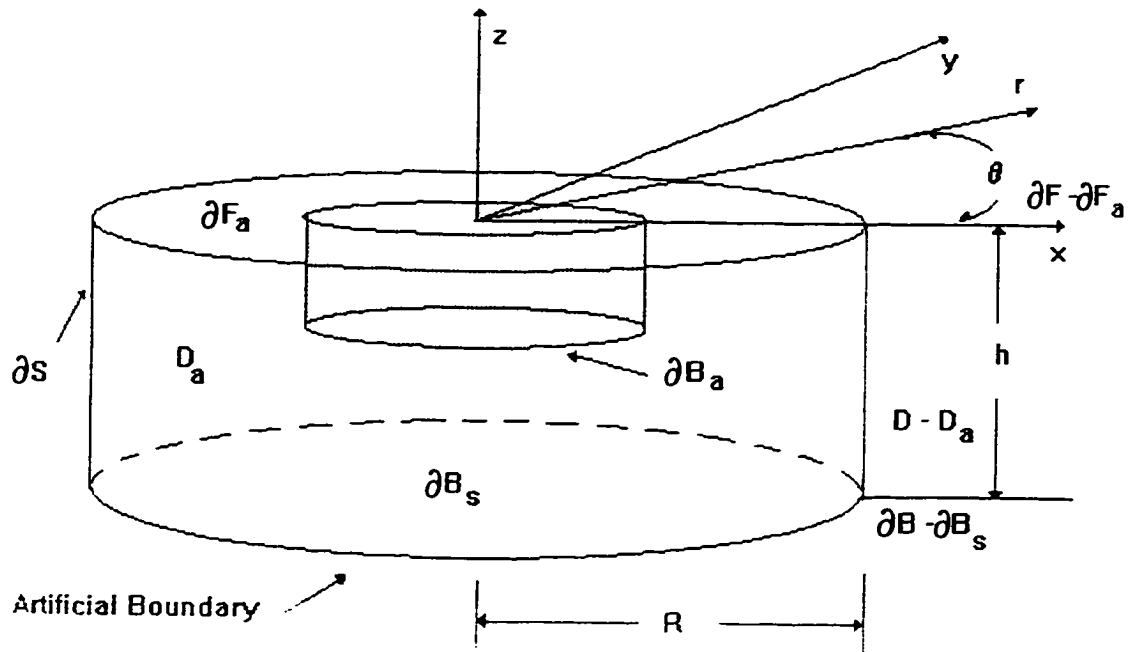
Figure 4.4. Definition Sketch of Domains, Boundaries, and Coordinate Systems

The fluid domain D is unbounded in any horizontal direction and the boundary ∂D of D can be expressed in the form $\partial D = \partial F + \partial B_a + \partial B$ whereas the artificial control fluid domain D_a is defined by the boundary $\partial D_a = \partial B_a + \partial F_a + \partial B_s + \partial S$, where ∂F_a and ∂B_s indicate the parts of ∂F (free-surface) and ∂B (sea bottom), respectively that are contained within ∂S (artificial cylindrical boundary).

4.4.2 Boundary Value Problem

The fluid domain D is regarded as an incompressible, inviscid and ideal fluid. Since the flow is assumed to be irrotational and harmonic, the velocity potential $\Phi(x,y,z,t)$ exists, such that the velocity field in D is described by

$$\bar{u} = \frac{\partial}{\partial \bar{x}} \, \Phi(\bar{x},t) \qquad (4.20)$$

where $\bar{x} = (x,y,z)$ denotes the radius vector in the cartesian coordinate system and t denotes the time variable. The corresponding free-surface displacement and dynamic pressure field are respectively

$$\eta(x,y,t) = -\frac{1}{g} \frac{\partial \Phi}{\partial t} \Big|_{z=0} \qquad (4.21)$$

$$p(x,y,z,t) = -\rho \frac{\partial \Phi}{\partial t} \qquad (4.22)$$

Within the linear approximation, the flow can be described by the velocity potential $\Phi(x,y,z,t)$ which satisfies the following boundary value problem:

Laplace Equation

$$\nabla^2 \Phi = \left(\frac{\partial}{\partial \bar{x}}\right)^2 \Phi = 0 \qquad \text{for} \bar{x} \epsilon D \qquad (4.23)$$

Dynamic Free-Surface Boundary Condition

$$\eta(x,y,t) = -\frac{1}{g} \frac{\partial \Phi}{\partial t} \qquad \text{for} \bar{x} \epsilon \partial F \qquad (4.24)$$

Kinematic Free-Surface Boundary Condition

$$\frac{\partial \eta}{\partial t}(x,y,t) = \frac{\partial \Phi}{\partial z} \qquad \text{for} \bar{x} \epsilon \partial F \qquad (4.25)$$

Combined Kinematic-Dynamic Free-Surface Boundary Condition

$$\frac{\partial^2 \Phi}{\partial t^2} + g\frac{\partial \Phi}{\partial z} = 0 \qquad \text{for} \bar{x} \epsilon \partial F \qquad (4.26)$$

<u>Impermeability Boundary Condition</u> $\qquad \left(\dfrac{\partial}{\partial n}\right)\Phi = V \qquad\qquad \text{for } \bar{x} \epsilon \partial B \qquad$ (4.27)

where: $\quad \dfrac{\partial}{\partial n} = \bar{n}\dfrac{\partial}{\partial \bar{x}}$

$\bar{n}$ = unit normal on $\partial B_a + \partial B$

V = normal velocity distribution

on $\partial B_a + \partial B$

and $V=0$ on the seafloor (∂B). Because the exterior walls of the OWC device are considered to be infinitely thin and the only projected area of the device in the x-y plane is that due to the internal plate, the radiation force (i.e. added mass and radiation damping) on the internal plate is approximated by solving the radiation condition with the device structure moving in the heave direction.

The velocity potential Φ can be expressed in the form

$$\Phi = \Phi_o + \Phi_s \qquad (4.28)$$

where, Φ_o is the velocity potential of the incident wave system and Φ_s is the velocity potential of the scattered waves from the device. The velocity potential of the incident wave system is

$$\Phi_o = \alpha_o \phi_o(\bar{x})e^{-i\omega t} \qquad (4.29)$$

where,

$$\phi_o(\overline{x}) = -\left(\frac{ig}{\omega}\right)\left(\frac{\cosh k(h+z)}{\cosh kh}\right)e^{ikr\cos(\theta_w)} \qquad \text{(Cylindrical Coordinates)} \qquad (4.30)$$

$$\phi_o(\overline{x}) = -\left(\frac{ig}{\omega}\right)\left(\frac{\cosh k(h+z)}{\cosh kh}\right)e^{ik(x\cos\theta_w - y\sin(\theta_w))} \qquad \text{(Cartesian Coordinates)} \qquad (4.31)$$

and θ_w is the direction of wave propagation, α_o is the wave amplitude, ω is the wave frequency and k is the wave number, defined by the dispersion relationship

$$\omega^2 = gk\tanh kh \qquad (4.32)$$

The velocity potential of the scattered waves Φ_s (second component in equation 4.28) is assumed to be of similar form to the incident wave velocity potential, such that

$$\Phi_s = \phi_s(\overline{x})e^{-i\omega t} \qquad (4.33)$$

Upon substituting equations 4.28, 4.29, 4.30, and 4.33 into the boundary conditions for Φ (equations 4.23, 4.26, and 4.27), it is found that Φ_s satisfies the following boundary conditions

$$\left(\frac{\partial}{\partial \overline{x}}\right)^2 \phi_s = 0 \text{ for } \overline{x}\in D \quad , \quad \left(\frac{\partial}{\partial z}-\frac{\omega^2}{g}\right)\phi_s = 0 \qquad \text{for } \overline{x}\in \partial F \qquad (4.34)$$

$$\frac{\partial}{\partial n}\phi_s = V \text{ for } \overline{x}\in \partial B + \partial B_a$$

The scattered potential must also satisfy the radiation condition which restricts the scattered waves to outgoing waves.

$$\underline{\text{Radiation Boundary Condition}} \qquad \sqrt{kr}\left(\frac{\partial}{\partial r} + ik\right)\phi_s = 0 \quad \text{for } kr\to\infty \qquad (4.35)$$

Based on the assumption that the structure oscillates harmonically with a small amplitude of motion, the six modes of oscillation ξ_j (surge, sway, heave, roll, yaw and pitch) may be written in the form

$$\xi_j = \alpha_j e^{-i\omega t} \quad \text{for } j=1,2,...6 \tag{4.36}$$

and the normal velocity distribution V on ∂B_a formulated by

$$V = -\alpha_o\left(\frac{\partial}{\partial n}\right)\phi_o - i\omega \sum_{j=1}^{3} \left[\alpha_j \overline{n}_j + \alpha_{j+3}(\overline{x} \times \overline{n})_j\right] \quad \text{for } \overline{x}\epsilon\partial B_a \tag{4.37}$$

where $(\alpha_1,\alpha_2,\alpha_3)$ denotes the complex amplitudes of displacements, $(\alpha_4,\alpha_5,\alpha_6)$ represents the complex amplitudes of angular displacements and $\overline{n}_j$ are the directional cosines. For a structure at rest (i.e. six modes of oscillation equal to zero), the normal velocity distribution reduces to the body surface boundary condition, $V = -\alpha_o\left(\frac{\partial}{\partial n}\right)\phi_o = \frac{\partial}{\partial n}\phi_s$ and the scattered velocity potential ϕ_s is expressed by

$$\phi_s = -i\omega \sum_{j=1}^{6} \alpha_j \phi_j + \alpha_7 \phi_7 \tag{4.38}$$

where $\alpha_7=\alpha_0$. As result of the linearity assumptions, seven independent scattering problems can be written in the form which satisfy the following boundary conditions

$$\left(\frac{\partial}{\partial \overline{x}}\right)^2 \phi_j = 0 \quad \text{for } \overline{x}\epsilon D \tag{4.39}$$

$$\left(\frac{\partial}{\partial z} - \frac{\omega^2}{g}\right)\phi_j = 0 \quad \text{for } \overline{x}\epsilon\partial F \tag{4.40}$$

$$\sqrt{kr}\left(\frac{\partial}{\partial r} - ik\right)\phi_j = 0 \quad \text{for } kr\rightarrow\infty \tag{4.41}$$

$$\left(\frac{\partial}{\partial n}\right)\phi_j = V_j \quad \text{for } \overline{x}\epsilon\partial B + \partial B_o \tag{4.42}$$

where V_j is simplified in the form of

$$V_j = (\bar{n}, \bar{x} \times \bar{n})_j \qquad\qquad j=1,2,...6 \qquad\qquad (4.43)$$

$$V_j = -\left(\frac{\partial}{\partial n}\right)\phi_o \qquad\qquad j=7 \qquad\qquad (4.44)$$

and $j=1,2,3,4,5,6,7$

The seven scattering problems are defined by taking in turn all but the j-th of the amplitudes $\alpha_1,\alpha_2...\alpha_7=\alpha_0$ equal to zero and assigning $\alpha_j=1$. The potential $\phi_1,\phi_2...\phi_6$ are referred to as the radiation potentials corresponding to the respective degrees of freedom of rigid body motion and ϕ_7 is the diffraction potential.

4.4.3 Variational Principle

The hybrid variational formulation uses three-dimensional finite elements in the region near the OWC device (nearfield) and assumes an analytical representation in a region away from the device (far field). In this method, the boundary value problem is reformulated in terms of a variational principle. Solutions in the finite element nearfield and the analytical farfield are required to satisfy matching conditions on the artificial cylindrical boundary, ∂s, so that all the unknown parameters in both regions can be solved.

The scattered wave velocity potential ϕ_j can be expressed in terms of the near and far fields, such that

$$\phi_j = \phi_j^{(a)} \quad \text{(nearfield)} \qquad \text{for } \bar{x} \epsilon D_a \tag{4.45}$$

$$\phi_j = \phi_j^{(1)} \quad \text{(farfield)} \qquad \text{for } \bar{x} \epsilon D\text{-}D_a \tag{4.46}$$

The farfield velocity potential $\phi_j^{(1)}$ obtained by solving the Laplace equation in cylindrical coordinates and boundary and radiation conditions is given by

$$\phi_j^{(1)} = \sum_{n=0}^{\infty} \left[\alpha_{on} \cos(n\theta) + \beta_{on} \sin(n\theta) \right] \cosh[k(z+h)] H_n^{(1)}(kr)$$

$$+ \sum_{n=0}^{\infty} \sum_{n=0}^{\infty} \left[\alpha_{mn} \cos(n\theta) + \beta_{mn} \sin(n\theta) \right] \cos[k_m(z+h)] K_n(k_m r) \tag{4.47}$$

where $H_n^{(1)}$ is the Hankel function of the first kind of order n, K_n is the modified Bessel function of the second kind of order n, h is the constant water depth and k_m denotes the positive real roots of

$$\omega^2 = -gk_m \tan(k_m h) \tag{4.48}$$

The coefficients α_{mn} and β_{mn} are unknown constants to be determined when combining with the near field equation.

The boundary conditions for the near field velocity potential $\phi_j^{(a)}$ are determined by substituting Equation 4.45 into the governing boundary conditions, such that

$$\left(\frac{\partial}{\partial z} \right)^2 \phi_j^{(a)} = 0 \qquad \qquad \text{for } \bar{x} \epsilon D_a$$

$$\left(\frac{\partial}{\partial z} - \frac{\omega^2}{g} \right) \phi_j^{(a)} = 0 \qquad \qquad \text{for } \bar{x} \epsilon \partial F \tag{4.49}$$

$$\left(\frac{\partial}{\partial n}\right)\phi_j^{(a)} = V_j \qquad \text{for } \overline{x}\epsilon\partial B_a + \partial B_s$$

The functions $\phi_j^{(a)}$ and $\phi_j^{(1)}$ are also required to satisfy the following matched conditions on the artificial cylindrical boundary ∂S

$$\phi_j^{(a)} = \phi_j^{(1)} \qquad \text{for } \overline{x}\epsilon\partial S$$

$$\left(\frac{\partial}{\partial r}\right)\phi_j^{(a)} = \frac{\partial}{\partial r}\phi_j^{(1)} \qquad \text{for } \overline{x}\epsilon\partial S$$

(4.50)

The potential ϕ_j satisfies the above governing equations if the following variation δJ_j remains equal to zero for all appropriate variations, $\delta\phi_j$ of ϕ_j

$$\delta J_j = \int_{D_a}\left(\frac{\partial}{\partial \overline{x}}\right)^2 \phi_j^{(a)}\delta\phi_j^{(a)}dD + \int_{\partial F_a}\left[\left(\frac{\partial}{\partial z} - \frac{\omega^2}{g}\right)\phi_j^{(a)}\right]\delta\phi_j^{(a)}dF$$

$$+ \int_{\partial B_a + \partial B_s}\left(\frac{\partial}{\partial n}\phi_j^{(a)} - V_j\right)\delta\phi_j^{(a)}dB \qquad (4.51)$$

$$+ \int_{\partial S}\left[\left(\frac{\partial}{\partial r}\phi_j^{(a)} - \frac{\partial}{\partial r}\phi_j^{(1)}\right)\delta\phi_j^{(a)} + \left(\phi_j^{(1)} - \phi_j^{(a)}\right)\frac{\partial}{\partial r}\delta\phi_j^{(1)}\right]dS$$

By first applying Gauss theorem and then Green's Identity, δJ_j is recognized as the variation of the function J_j which is defined as

$$J_j\left(\phi_j^{(a)},\phi_j^{(1)}\right) = (1/2)\int_{D_a} \left[\left(\frac{\partial}{\partial\overline{x}}\right)\phi_j^{(a)}\right]^2 dD_a \;-\; \frac{\omega^2}{2g}\int_{\partial F_a}\left[\phi_j^{(a)}\right]^2 dF_a$$

$$-\int_{\partial B_a - B_s} V_j\phi_j^{(a)}dB \;+\; (1/2)\int_{\partial S}\phi_j^{(1)}\left(\frac{\partial}{\partial r}\right)\phi_j^{(1)}dS \qquad\qquad (4.52)$$

$$-\int_{\partial S}\phi_j^{(a)}\left(\frac{\partial}{\partial r}\right)\phi_j^{(1)}dS$$

The functions $\left(\phi_j^{(1)},\phi_j^{(a)}\right)$ which make the function J_j stationary provide the solution of the j-th scattering problem. The velocity potentials $\left(\phi_j^{(a)},\phi_j^{(1)}\right)$ are determined by applying the conditions for stationarity of the functional (described in the next section) and solving the resulting linear equations.

4.4.4 Velocity Potential Solution

The functional J_j described by Pawlowski (1985) can be written in the form

$$J_j = \left(\frac{1}{2}\right)\int_{D_a}\left(\frac{\partial\phi_j^{(a)}}{\partial\overline{x}}\right)^2 dD \;-\; \frac{\omega^2}{2g}\int_{\partial F_a}\left(\phi_j^{(a)}\right)^2 dF$$

$$-\int_{\partial B_o} V_j\phi_j^{(a)}dB_a \;-\; \int_{\partial B_s} V_j\phi_j^{(a)}dB_s \;+\; \left(\frac{1}{2}\right)\int_{\partial S}\phi_j^{(1)}\frac{\partial\phi^{(1)}}{\partial r}dS \qquad (4.53)$$

$$-\int_{\partial S}\phi_j^{(a)}\frac{\partial\phi_j^{(1)}}{\partial r}dS$$

The six integrals in the functional J_j are determined by approximating the near field fluid domain D_a by finite elements. The finite element mesh uses 20 node hexahedral elements with numbered nodes as shown in Figure 4.5.

ELEMENT FACE NUMBER	CORNER NODES
1	1 , 3 , 5 , 7
2	13 , 15 , 17 , 19
3	1 , 3 , 15 . 13
4	7 , 5 , 17 , 19
5	3 , 5 . 15 . 17
6	1 , 13 , 19 , 7
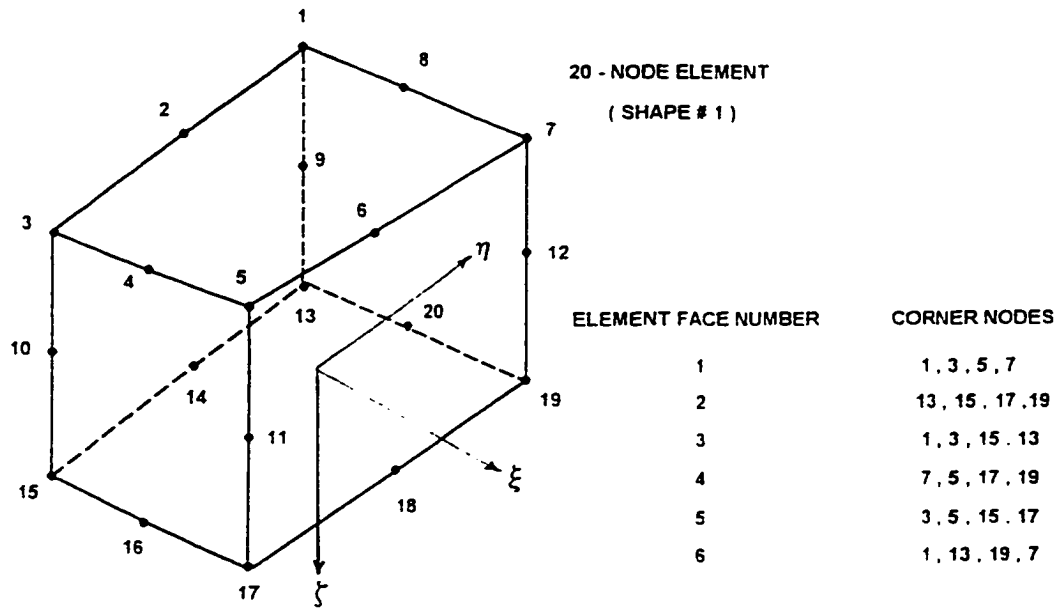
Figure 4.5. Local Coordinate System for 20 Node Hexahedral Elements

The nodal coordinates ξ_i, η_i, ζ_i, where the index i indicates the number of the node (i.e. 1 to 20), may have values value 0, -1 or +1, depending on the location of the node. Points $\overline{\xi} = (\xi, \eta, \zeta)$ are mapped from the local ξ, η, ζ space into points $\overline{x} = (x, y, z)$ in the global x,y,z space (i.e. finite element mesh) by a transformation composed of interpolation functions.

These interpolation functions are used (Yue et al. (1976)) and Pawlowski (1985)) as approximating functions for the scattering potential $\phi_j^{(a)}$ in the functional J_j. By defining

$$\hat{\phi}_j^{(a)} = \text{approximation of } \phi_j^{(a)} \text{ in } D_a$$

$$_e\hat{\phi}_j^{(a)} = \text{approximation of } \phi_j^{(a)} \text{ in the elements } D_a$$

(4.54)

Numerical integration in the finite element interior region is performed using the local coordinate system where the approximations used for the transformation of volume and surfaces of the elements are given in Pawlowski (1985). The integrals of the functional J_j, can then be approximated by finite elements or their sides by

$$\hat{J}_{1j}^{(a)} = \left(\frac{1}{2}\right) \int_{D_a} \left(\frac{\partial}{\partial x} \,_e\hat{\phi}_j^{(a)}\right)^2 dD^a$$

(4.55)

$$\hat{J}_{2j}^{(a)} = \left(\frac{-\omega^2}{2g}\right) \int_{\partial F_a} \left(\,_e\hat{\phi}_j^{(a)}\right)^2 dF_a^{(a)}$$

(4.56)

$$\hat{J}_{4j}^{(a)} = - \int_{\partial S^a} \,_e\hat{\phi}_j^{(a)} \frac{\partial}{\partial r} \phi_j^{(1)} \, dS^a$$

(4.57)

$$\hat{J}_{5j}^{(a)} = - \int_{\partial B_a} V_j \,_e\hat{\phi}_j^{(a)} dB_a^{(a)}$$

(4.58)

$$\hat{J}_{6j}^{(a)} = -\int_{\partial B_e^a} V_j \, _e\hat{\phi}_j^{(a)} dB_s^{(a)}$$

(4.59)

and the integral on the artificial control surface by

(4.60) $\quad \hat{J}_{3j}^{(a)} = \dfrac{1}{2}\int_{\partial S} \hat{\phi}_j^{(1)} \dfrac{\partial}{\partial r}\hat{\phi}_j^{(1)} \, dS$

The evaluation of the integrals are given in Pawlowski (1985). The approximate functional can be written in terms of the assembled matrices and vectors as

$$\hat{J}_j = \left(\frac{1}{2}\right)\langle\hat{\phi}_j^a(\bar{x}_n)\rangle([K_1]+[K_2])\{\hat{\phi}_j^a(\bar{x}_n)\}$$

$$+ \left(\frac{1}{2}\right)\langle U_j\rangle[K_3]\{U_j\} + \langle U_j\rangle[K_4]^T\{\hat{\phi}_j^a(\bar{x}_n)\}$$

(4.61)

$$- \langle Q_{pj}\rangle\{\hat{\phi}_j^a(\bar{x}_n)\} - \delta(j,7)\langle Q_r\rangle\{\hat{\phi}_j^a(\bar{x}_n)\}$$

where $\delta(j,7)=0$, unless $j=7$, $K_j(j=1,2,3,4)$ are the assembled matrices, Q_{pj} ($j=1,2,...7$) and Q_r are the assembled vectors, and $\{U_j\}$ vector of coefficient unknowns. The condition to make $\hat{J}_j$ stationary is

$$\frac{\partial \hat{J}_j}{\partial\{\hat{\phi}_j^a(\bar{x}_n)\}_i} = 0 \quad \text{for } i = 1,2,...nnod$$

(4.62)

$$\frac{\partial \hat{J}_j}{\partial\{U_j\}_i} = 0 \quad\quad \text{for } i = 1,2,...ncof \ \{U_j\}$$

(4.63)

where

nnod   =   number of finite element nodes in D_a

ncof{U_j} = total number of unknown coefficients in the exterior analytical representation

These conditions give two sets of linear equations and when combined yields the following expression

$$\left([K_1] + [K_2] - [K_4][K_3]^{-1}[K_4]^T\right)\left\{\hat{\phi}_j^a(\bar{x}_n)\right\} = \left\{Q_{pj}\right\} + \delta(j,7)\left\{Q_r\right\} \qquad (4.64)$$

which when solved gives the velocity potential at every finite element nodal point in the near field for a particular j-th scattering problem.

4.4.5 Hydrodynamic Forces

The hydrodynamic forces on the internal oscillating water column surface are determined by integrating the fluid pressures acting on the plate. In general, the dynamic pressure field $P(x,y,z,t)$ in the fluid domain is given by the linearized Bernoulli equation $P(x,y,z,t) = -\rho \partial \Phi / \partial t$, where the total velocity potential Φ, comprised of the incident wave potential (ϕ_o) radiation potentials ϕ_j and diffraction potential ϕ_7 is

$$\Phi = \left[\alpha_o \phi_o - i\omega \sum_{j=1}^{6} \alpha_j \phi_j + \alpha_o \phi_7 \right] e^{-i\omega t} \qquad (4.65)$$

Substituting Φ into the dynamic pressure equation and differentiating with time yields

$$P(x,y,z,t) = P(x,y,z)e^{-i\omega t} \qquad (4.66)$$

where

$$P(x,y,z) = \rho i \omega \left[\alpha_o \phi_o - i \omega \sum_{j=1}^{6} \alpha_j \phi_j + \alpha_o \phi_7 \right] \qquad (4.67)$$

Based on this pressure distribution, Pawlowski (1985) derives the resultant hydrodynamic forces and moments on the body for the six degrees of freedom. Because translational motions are particularly relevant to the present research (i.e. heave motions), the resultant forces due to translational motions only are presented in this section. The linearized time dependent hydrodynamic resultant force for translational motions can be expressed by

$$\bar{F} = \bar{f}_k e^{-i\omega t} \qquad (4.68)$$

where the linearized hydrodynamic resultant force $\bar{f}_k$ (k = 1,2,3 are the force components) is given by

$$\bar{f}_k = \rho i \omega \left(\alpha_o \int_{\partial B_a} \phi_o \bar{n}_k dB_a - i \omega \sum_{j=1}^{3} \alpha_j \int_{\partial B_a} \phi_j \bar{n}_k dB_a + \alpha_o \int_{\partial B_a} \phi_7 \bar{n}_k dB_a \right)$$

$$= \rho i \omega \alpha_o \int_{\partial B_a} \phi_o \bar{n}_k dB_a + \rho \omega^2 \sum_{j=1}^{3} \alpha_j \int_{\partial B_a} \phi_j \bar{n}_k dB_a + \rho i \omega \alpha_o \int_{\partial B_a} \phi_7 \bar{n}_k dB_a \qquad (4.69)$$

The three force terms are defined as

First Term (Froude-Krylov Force)

$$\bar{f}_{k0} = \rho i \omega \alpha_o \int_{\partial B_a} \phi_o \bar{n}_k dB_a \qquad (4.70)$$

Second Term (Radiation Force)

$$\bar{f}_{kj} = \rho \omega^2 \alpha_j \int_{\partial B_a} \phi_j \bar{n}_k dB_a \quad \text{for } j=1,2,3 \qquad (4.71)$$

Third Term (Diffraction Force)

$$\bar{f}_{k7} = \rho i \omega \alpha_o \int_{\partial B_a} \phi_7 \bar{n}_k dB_a \qquad (4.72)$$

The Froude-Krylov force and diffraction forces can be normalized (~) by defining

$$\phi_j = -\left(\frac{ig}{\omega}\right)\bar{\phi}_j \qquad \text{for } j = 0,7$$

$$\bar{f}_{k0} = \rho g \alpha_o a^2 \bar{f}_{k0} \qquad (4.73)$$

$$\bar{f}_{k7} = \rho g \alpha_o a^2 \bar{f}_{k7}$$

Combining $\bar{f}_{k0}$ and $\bar{f}_{k7}$ yields the following normalized force expression

$$\bar{f}_{k(0+7)} = \int_{\partial B_a} (\bar{\phi}_o + \bar{\phi}_7)\bar{n}_k dB \qquad (4.74)$$

where, $\bar{f}_{k(0+7)} = \dfrac{(\bar{f}_{k0} + \bar{f}_{k7})}{\rho g \alpha_o a^2} = \dfrac{\bar{f}_{k(0+7)}}{\rho g \alpha_o a^2}$. The radiation forces are defined by

$$\bar{f}_{kj} = \rho \omega^2 \alpha_j \int_{\partial B_a} \phi_j \bar{n}_k dB_a \qquad \text{for } j = 1,2,3 \qquad (4.75)$$

However since $(\bar{n})_j = V_j = \dfrac{\partial}{\partial n}\phi_j$

$$\bar{f}_{kj} = \rho \omega^2 \alpha_j \int_{\partial B_a} \phi_j \frac{\partial}{\partial n}\phi_k dB_a \qquad \text{for } j = 1,2,3 \qquad (4.76)$$

The real added mass A_{kj} and radiation damping B_{kj} coefficients are defined such that

$$\rho \int_{\partial B_a} \phi_j \frac{\partial}{\partial n}\phi_k dB_a = A_{kj} - \left(\frac{1}{i\omega}\right)B_{kj} \qquad \text{for } j = 1,2,3 \qquad (4.77)$$

Substituting equation 4.77 into 4.76 gives

$$\bar{f}_{kj} = \omega^2 \alpha_j \left[A_{kj} - \left(\frac{1}{i\omega} \right) B_{kj} \right] \qquad \text{for } j=1,2,3$$

$$\frac{\bar{f}_{kj}}{\omega \alpha_j} = \omega A_{kj} + i B_{kj}$$

(4.78)

where, $\dfrac{\bar{f}_{kj}}{\omega \alpha_j}$ = force per unit velocity

A_{kj} = coefficients of added mass matrix

B_{kj} = coefficients of radiation damping matrix

In normalized form, the radiation force can be written as

$$\tilde{f}_{kj} = \left(\tilde{\omega}^2 \tilde{A}_{kj} + i \tilde{\omega} \tilde{B}_{kj} \right) \tilde{\alpha}_j , \qquad j=1,2,3$$

(4.79)

where $\tilde{f}_{kj} = \dfrac{\bar{f}_{kj}}{\rho g \alpha_o a^2}$ $\qquad \tilde{B}_{kj} = \dfrac{B_{kj}}{\rho a^3 \sqrt{\dfrac{g}{a}}}$

$\tilde{\alpha}_j = \dfrac{\alpha_j}{\alpha_0} ,$ $\qquad \tilde{\omega} = \dfrac{\omega}{\sqrt{\dfrac{g}{a}}}$

$\tilde{A}_{kj} = \dfrac{A_{kj}}{\rho a^3}$

In reference to the oscillating water column device, the hydrodynamic forces of importance are the vertical (k=3) diffraction force (including the Froude-Krylov force) and heave (j=3,k=3) radiation force. In terms of the normalized hydrodynamic coefficients, these are

$$\tilde{A}_{kj} = \tilde{A}_{33} = \frac{A_{33}}{\rho a^3}$$

$$\tilde{B}_{kj} = \tilde{B}_{33} = \frac{B_{33}}{\rho a^3 \sqrt{\dfrac{g}{a}}}$$

$$\tilde{f}_{k(0 \cdot \eta)} = \tilde{f}_{3(0 \cdot \eta)} = \frac{\bar{f}_{3(0 \cdot \eta)}}{\rho g \alpha_o a^2}$$

(4.81)

For convenience in later sections, these terms are referred to as the normalized coefficients of

added mass ($\mu = \tilde{A}_{33}$), radiation damping ($b_r = \tilde{B}_{33}$), and vertical diffraction force ($C_z = \dfrac{F_d}{\rho g \alpha_o a^2} = \bar{f}_{3(0 \cdot \eta)}$).

4.5   Radiation-Diffraction Test Cases

Two test cases were used as examples to verify the hydrodynamic results of the Radiation

Diffraction Finite Element (RDFE) program:

Test Case I   -   Floating Square Dock numerically modelled by Yue et al. (1976)

$(\theta_w = 45°)$

Test Case II   -   Floating Cylindrical Dock numerically modelled by Rahman and

Bhatta (1992) $(\theta_w = 0°)$

The numerical method developed by Yue et al. (1976) is similar to the Finite Element Hybrid

method described in the previous sections with the exception of solving the wave scattering

problem for diffraction only.   Rahman and Bhatta (1992) used the method of separation of

variables to solve analytically the velocity potentials for the near field (below the cylindrical dock)

and far field fluid regions and matched the solutions at the artificial cylindrical boundary. The unknown coefficient for the interior and exterior regions were then solved numerically to determine expressions for the forces and moments on the structure.

The finite element grids used to model the nearfield fluid domain (i.e. within the artificial cylindrical boundary) for both test cases are given in Figure 4.6 and consist of elements distributed over 3 radial and 2 vertical layers. The characteristics of the finite element grids are given in Table 4.2.

Table 4.2   Finite Element Grid Characteristics for
Test Cases I and II

FE Grid	Test Case I (Floating Square Dock)	Test Case II (Floating Cylindrical Dock)
Elements	56	56
Nodes	435	435
Free Surface Faces	16	16
Body Faces	40	40
Artificial Boundary Faces	32	32
Characteristic Water Depth	1.0a	2.0a

The vertical diffraction force C_z (i.e. $\bar{f}_{3(0-7)}$) was computed for the normalized wave lengths (ka) between 0.1 to 6.0 and compared to the numerical results of Yue et al. (1976) and Rahman and Bhatta (1992) in Figure 4.7. The results show good agreement for the entire range of computed wave frequencies.
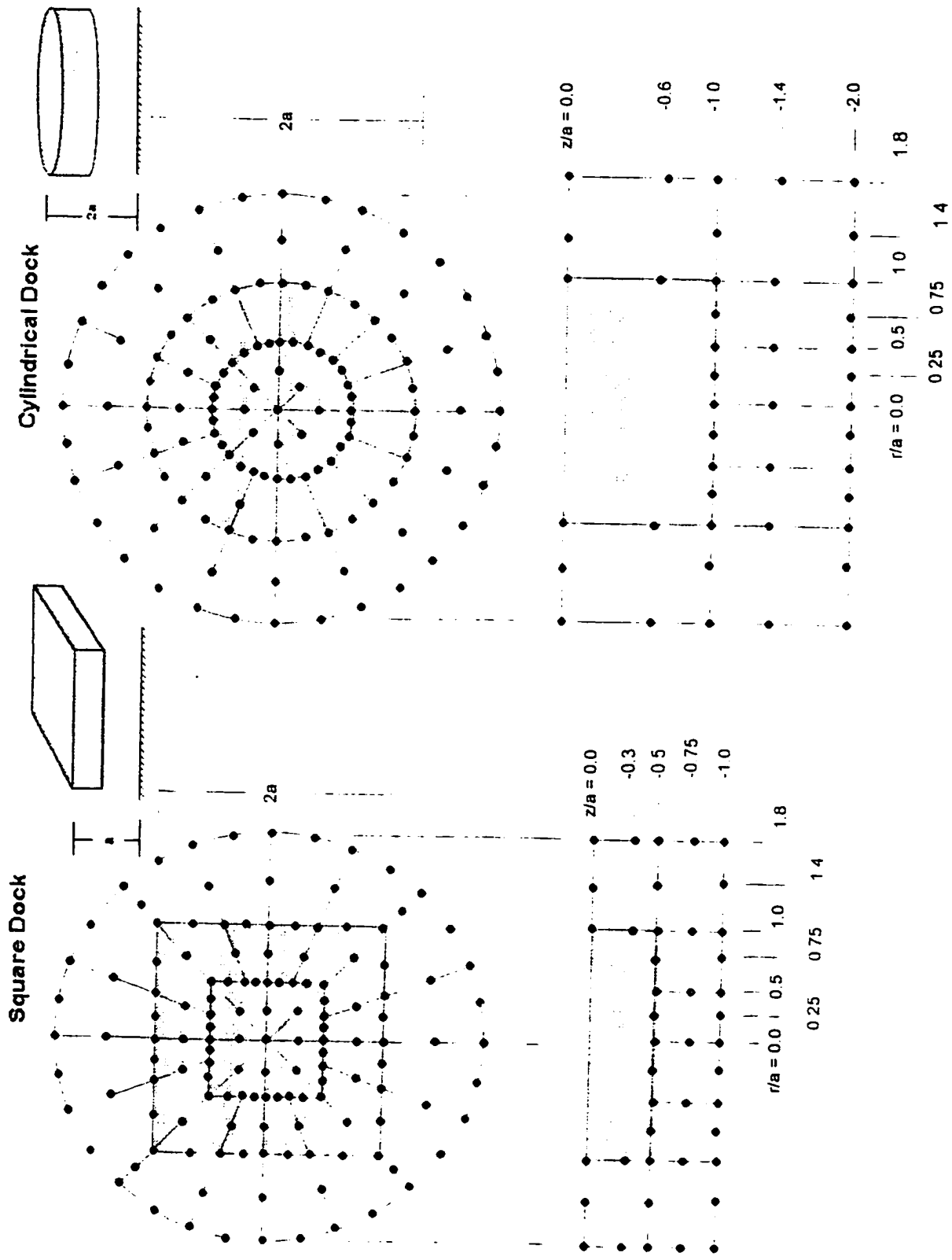
Figure 4.6. Finite Element Grids for Test Cases I and II
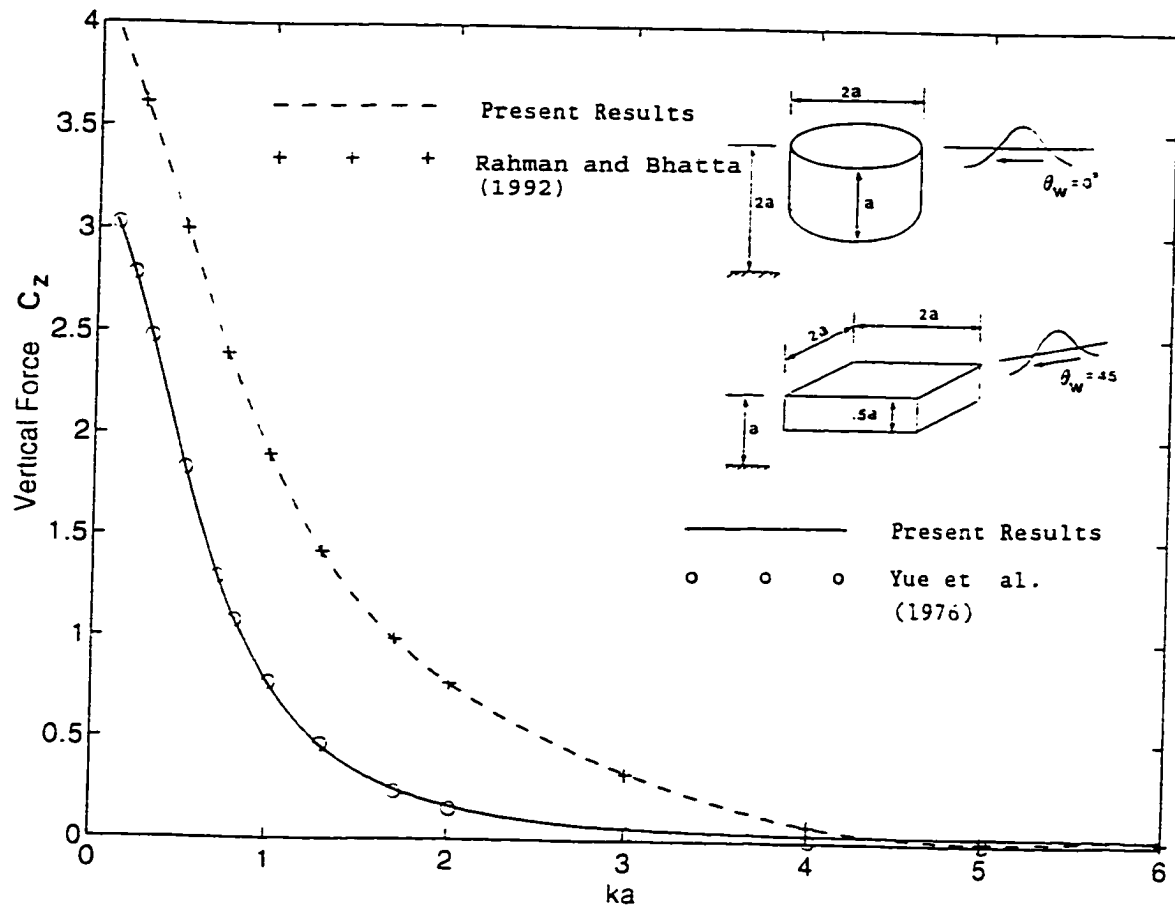
Figure 4.7. Comparison of Vertical Diffraction Force C_z Results
with Numerical Results of Yue et al. (1976) (Square Dock)
and Rahman and Bhatta (1992) (Cylindrical Dock)

CHAPTER 5

PERFORMANCE OF THE OSCILLATING WATER COLUMN DEVICE

IN MONOCHROMATIC SEAS

5.1   Oscillating Water Column Device Types

The 3-dimensional numerical results for various geometrical configurations of the OWC

device in monochromatic seas are presented in this Chapter. Figure 5.1 depicts the various OWC

device types modelled by the finite element and analytical methods for the determination of

average wave power extraction. The rationale for choosing the various geometrical configur-

ations was based on the following:

(1)   Previous investigators have studied the 3-dimensional effects of OWC devices

        with a similar geometrical configuration as device Type 1 (Robinson (1982),

        McCormick (1974), and others), device Type 4 (Count et al. (1983), Sarmento

        and Falcao (1985)), and device Type 6 (Count et al. (1983), Ambli et al. (1982)

        and Koola et al. (1995)), but a relative comparison of the frequency and

        directional bandwidths has not been thoroughly investigated.

(2)   In the past, no consideration was given in extending only a back wall (device type

        2), a back wall and two half sidewalls (device type 3), or a back wall and one

        sidewall (device type 5) to determine the effects on device performance for a

        range of wave frequencies and incident wave directions.

TYPE 1

TYPE 2

TYPE 3

TYPE 4

TYPE 5
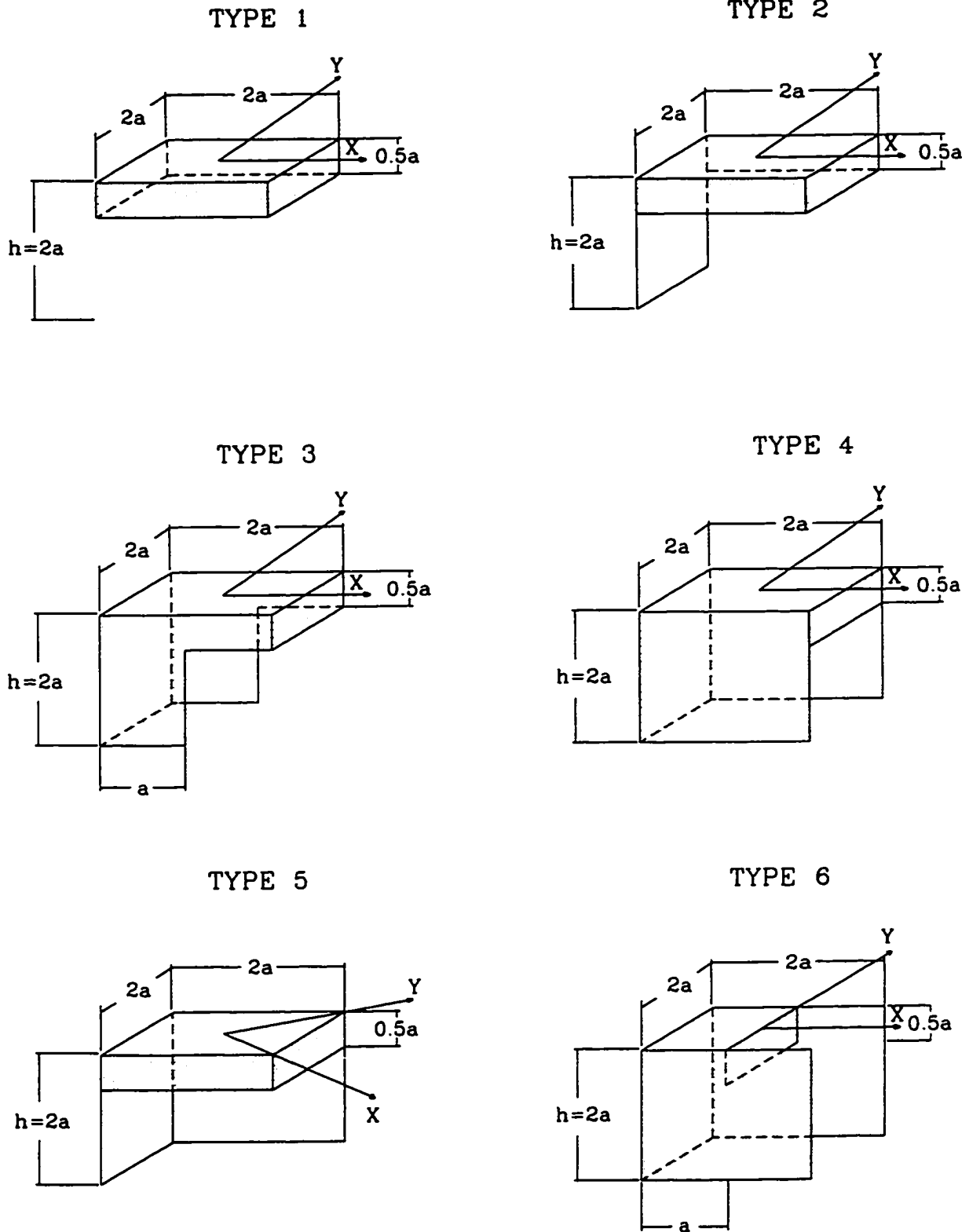
TYPE 6

Figure 5.1. Oscillating Water Column Device Types 1 through 6

(3)   Device type 6, with two protruding walls from the front of the device, has been shown (Count et al. (1983)) to improve the frequency response significantly by creating an additional resonance with the incident waves. Determining this additional resonance by the method of Finite Elements (Hybrid Method) would be a numerical verification of the mathematical approach used in this research.

(4)   By determining the variations in natural frequency and peak performance between device types, a quantitative assessment can be made into the effects of wall geometry on wave power extraction.

(5)   All of the device types are modelled in finite depth (h=2a) with dimensions of 2ax2a and a draft equal to 0.5a. These dimensions are considered reasonable to carry out a comparative analysis for the performance of an OWC device type in coastal waters. The dimensions do not represent an optimized design. Device optimization (for a particular finite depth) would require site specific data on many variables (e.g. statistical wave heights, periods, and directions).

In addition to the OWC device types 1 through 6, given in Figure 5.1, other geometrical configurations are modelled in later sections for verification procedures, including a cylindrical attenuator OWC device similar to device type 1.

5.2   Capture Width Ratio

For isolated three-dimensional devices the appropriate quantity to define an efficiency of power absorption is a capture width ratio (Evans (1981)), defined as the ratio of the average wave

power absorbed (P_e) to the incident mean wave power (P) per device length. In this research the Capture Width Ratio (CWR) is defined as

$$CWR = \frac{P_e}{P(2a)}, \qquad \text{for a cylindrical internal surface}$$

$$CWR = \frac{P_e}{P(l_y a)}, \qquad \text{for a rectangular internal surface}$$

where the terms in brackets ( ) represent the device length for a cylindrical OWC device (2a) and a rectangular OWC device ($l_y a$). The average power extraction (P_e) and incident mean wave power (P) were derived earlier and are given by

$$P_e = \frac{1}{2} B_a \omega^2 \xi_o^2 = \frac{1}{2} B_a \omega^2 \alpha_o^2 \left(\frac{\xi_o}{\alpha_o}\right)^2 \tag{5.1}$$

$$P = \frac{\rho g^2 \alpha_o^2 T}{8\pi} \left[1 + \frac{2kh}{\sinh 2kh}\right] \tanh kh \tag{5.2}$$

The capture width ratio can be expressed in terms of the non-dimensional coefficients of vertical diffraction force (C_z), heave added mass (μ) and radiation damping (b_r) and dimension-alized applied damping (b_a) by substituting

$$C_z = \frac{F_d}{\rho g \alpha_o a^2}, \quad \mu = \frac{m_a}{\rho a^3}, \quad b_r = \frac{B_r}{\rho a^3 \sqrt{\dfrac{g}{a}}} \quad \text{and} \quad b_a = \frac{B_a}{\rho a^3 \sqrt{\dfrac{g}{a}}} \tag{5.3}$$

into the amplitude of oscillation ξ_o (Equation 4.7) gives

$$\xi_o = \frac{\rho g \alpha_o a^2 C_z}{\left(\left(k_r - \omega^2 (\rho a^3 \mu)\right)^2 + \left(\omega \rho a^3 \sqrt{\frac{g}{a}}(b_a + b_r)\right)^2\right)^{1/2}}$$ (5.4)

The hydrostatic restoring coefficient (k_r) is related to the area (A) of the interior OWC surface and can be expressed by

$$k_r = \rho g A = \rho g \pi a^2 \quad \text{for a cylindrical internal surface}$$

and

$$k_r = \rho g A = \rho g (l_x a \cdot l_y a) = \rho g l_x l_y a^2 \quad \text{for a rectangular internal surface}$$

Based on these relationships and replacing the angular wave frequency ω by a normalized wave period $W_T = \dfrac{2\pi}{\omega \sqrt{\dfrac{a}{g}}}$ gives a non-dimensional amplitude of oscillation $\left(\dfrac{\xi_o}{\alpha_o}\right)$ in the form:

$$\left(\frac{\xi_o}{\alpha_o}\right) = \frac{C_z}{\left(\left(\alpha_1 - \frac{4\pi^2}{W_T^2}\mu\right)^2 + \left(\frac{2\pi}{W_T}(b_a + b_r)\right)^2\right)^{1/2}}$$ (5.5)

where $\alpha_1 = \pi$ for a cylindrical internal surface and $\alpha_1 = l_x l_y$ for a rectangular internal surface. Expressing the CWR in terms of the dimensionless coefficients results in the expression

$$\text{CWR} = \frac{4\alpha_2 \pi^3}{W_T^3} b_a \left(\frac{\xi_o}{\alpha_o}\right)^2 \frac{1}{\left[1 + \frac{2 l_z ka}{\sinh 2 l_z ka}\right] \tanh l_z ka}$$ (5.6)

where $\alpha_2 = 2$ for cylindrical OWC devices and $\alpha_2 = l_y$ for rectangular OWC devices. This expression is used to determine the performance of a particular OWC device type for a range of dimensionless wave numbers (ka).

A convergence study was carried out to determine the proper number of finite elements and the size of finite element grid required for numerical convergence of the various device types. As discussed earlier, one of the main advantages of the Hybrid Finite Element Method is the relatively small number of finite elements required for numerical convergence (Mei (1978)). However, convergence studies into the number of elements required in the interior of the OWC device have not been previously documented. The capture width ratio was used as the parameter for estimating convergent solutions. The convergence study was carried out for Device Type 6 and consisted of determining the number of:

(1)   radial elements required for convergent solutions;

(2)   vertical elements required for convergence to a finite depth twice the characteristic dimension (a), and

(3)   interior elements, both radially and vertically.

The number of radial elements outside the device was varied between 3 to 1 without allowing the solution to diverge. The size of element for the outside radial ring (at the artificial boundary) was chosen to be 1.8 times the characteristic dimension. The solution diverges when the artificial boundary is less than this value and too close to the boundary of the device wall.

The number of vertical elements beneath the OWC chamber was varied between 4 to 2 layers without affecting the numerical convergence. However, with 1 layer beneath the chamber, the solution diverged approximately 5.5% from the 2 layer solution for dimensionless wavelength values (ka) greater than 1.2.

The interior of the OWC device was modelled with 1 layer vertically and the solution did not diverge from the original 2-layer solution. It was also found that the solution converged for

the model with either 3 or 2 radial rings in the interior region, however the solution was found to diverge for 1 radial ring.

5.3   Device Type 1 - Monochromatic Waves

Figure 5.2 presents the geometrical configuration of Device Type 1 and the finite element grid used for the radiation diffraction finite element method. The response of the device was determined not only for the water depth (h=2a) and device draft (l_d=0.5a) given in Figure 5.6, but for a number of different water depths (h=a, 2a, and 3a) and drafts (l_d=.25a, .33a, .50a, and 1.0a). The finite element grids for these additional configurations are not shown, but are similar to the one given in Figure 5.2, with the exception of the number of finite element layers used throughout the water depth. Table 5.1 summarizes the finite element grid characteristics for the different configurations. The interior of the device was discretized with 24 elements to account for the interior OWC fluid. The top face for each of these elements was identified as boundary faces which represent the interior surface plate. In addition, the side walls of the device (with draft, l_d), were accounted for by 32 boundary faces; 16 on the interior walls and 16 on the exterior walls.

For the six different configurations considered for device type 1, the finite element model was numerically run to determine the non-dimensional coefficients of C_z, μ and b_r for a range of ka values between 0.1 to 6.0 and a wave direction θ_w = 0°. Figure C.1 in Appendix C presents the non-dimensional coefficients of vertical diffraction force (C_z) for the conditions of fixed water depth (h=2a) and varying drafts (l_d=0.25a, 0.33a, 0.5a and 1.0a) and the conditions of fixed draft (l_d=0.5a) and varying water depths (h=a, 2a, and 3a). Plots for the non-dimensional
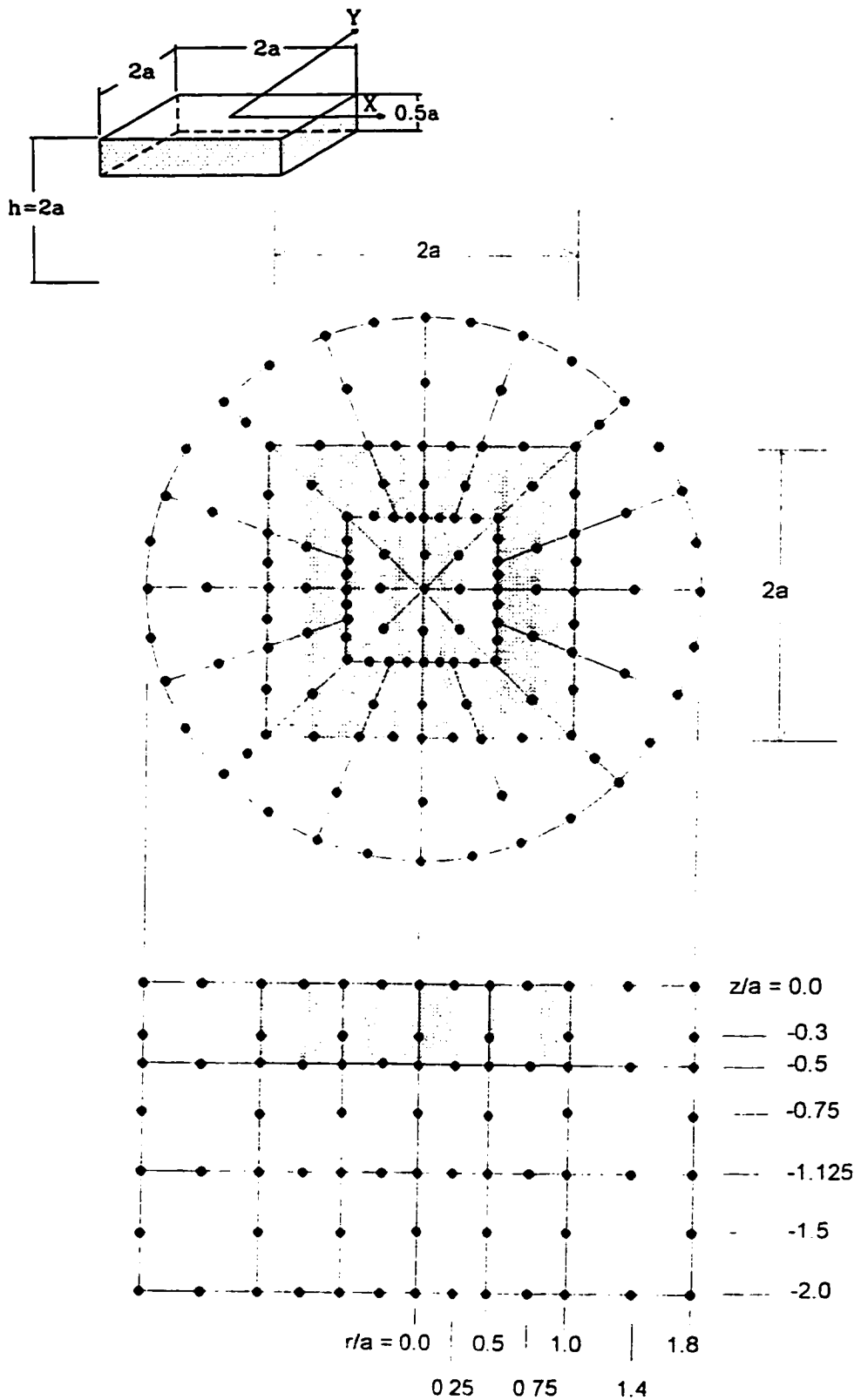
Figure 5.2. Finite Element Grid for Device Type 1
$(l_x=l_y=l_z=2.0, l_d=0.5a)$

coefficients of heave added mass (μ) and radiation damping (b_r) for the same conditions are given

in Figures C.2 and C.3, respectively.

TABLE 5.1. Finite Element Grid Characteristics for Different
Configurations of Device Type 1

Water Depth (h)	Draft (L_d)	Total No. of Elements	Total No. of Nodes	Total No. of Vertical Layers	Total No. of Radial Layers	Total No. of FE Faces on Device
1.0a	0.5a	80	557	2	3	56
2.0a	0.5a	120	743	3	3	56
2.0a	0.25a	200	1115	5	3	56
2.0a	0.33	160	929	4	3	56
2.0a	1.0a	80	557	2	3	56
3.0a	0.5a	160	929	4	3	56

The performance of the device is presented in terms of the capture width ratio CWR for

$\alpha_2 = l_y = 2.0$ and

$$CWR = \left(\frac{2\pi}{W_T}\right)^3 b_a \left(\frac{\xi_o}{\alpha_o}\right)^2 \frac{1}{\left[1 + \frac{2 l_z ka}{\sinh 2 l_z ka}\right] \tanh l_z ka} \qquad (5.7)$$

where the non-dimensional amplitude of oscillation ξ_o/α_o for $\alpha_1 = 4.0$ is given by

$$\left(\frac{\xi_o}{\alpha_o}\right) = \frac{C_z}{\left(\left(4-\frac{4\pi^2}{W_T^2}\mu\right)^2 + \left(\frac{2\pi}{W_T}(b_a+b_r)\right)^2\right)^{1/2}}$$ (5.8)

The oscillating water column is optimized for power extraction when the device is tuned to the

resonant conditions, such that $4-\frac{4\pi^2}{(W_T)_{res}^2}\mu = 0$ and $b_a=b_r$ at the resonant normalized period

$(W_T)_{res}$. The resonant normalized wave period and corresponding non-dimensional applied

damping coefficient for optimized power was determined for each configuration of device type

1. As an example, for the case of h=2a and l_d=0.5a, resonant conditions occur when ka=1.12

and μ=3.65. At this resonant frequency, the radiation damping (b_r) was set equal to the applied

damping (b_a) such that $b_a=b_r=$ 0.750. These conditions were then substituted in the above

expression for CWR and plotted for the range of ka values considered. Figure 5.3 presents the

capture width ratio for varying water depths and device drafts.

The response curves for the device configurations with a fixed water depth and varying

drafts (upper figure) show the following:

(1)   Increasing the draft (l_d) of the device has the effects of increasing the peak

performance, shifting the peak to lower ka value and reducing the frequency

bandwidth.

(2)   The relatively broad banded response for devices with shallow drafts is

advantageous for capturing energy from the higher frequency waves, but are

often not practical due to the limitation of wave heights larger than $H \approx 2l_d$.

The effects of water depth on device performance (lower figure) with a fixed draft are

the following:
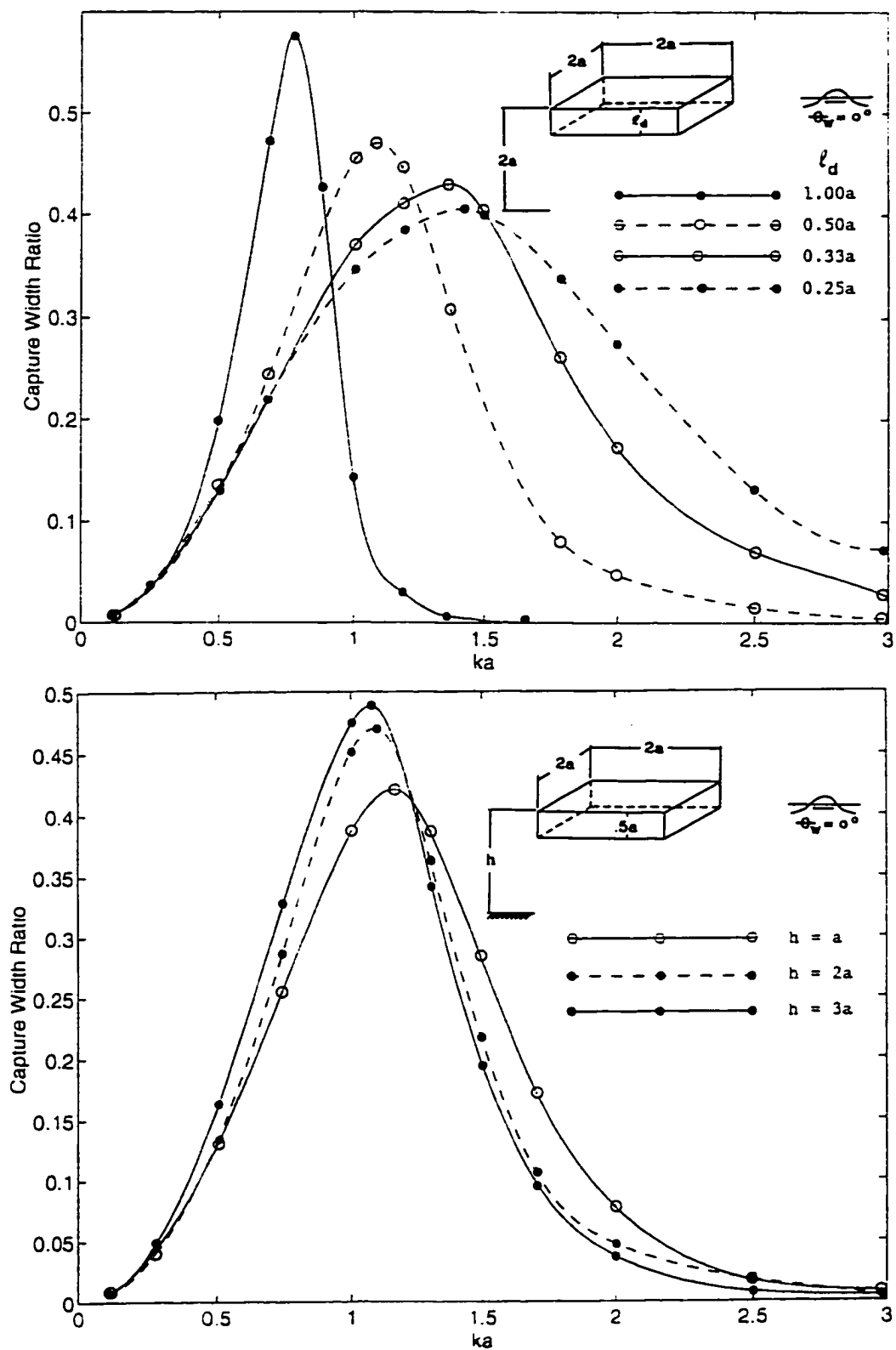
Figure 5.3. Capture Width Ratio for Device Type 1 with Varying Drafts (Upper Figure) and Varying Water Depths (Lower Figure)

(1)   Increasing the water depth has the effect of increasing the peak performance and slightly shifting the peak performance to a lower ka value.

(2)   For increased water depths, the performance of the device approaches the deep water limiting curve, which is the condition for the maximum peak capture width ratio for the device configuration.

For the case of h=2a and l_d=0.5a, additional wave directions (θ_w=22.5° and 45°) were numerically run to determine the effects of wave directionality on device performance. The curves are not presented here due to the remarkably small variation in performance from the results for θ_w=0°. The optimum capture width ratio occurs for θ_w=45°, a result originally presented by Evans (1982), which is the wave direction that produces the maximum area-averaged dynamic pressure in the water column. This maximum pressure can also be verified by simple linear wave theory, neglecting the effects of wave diffraction.

5.4   Device Type 2 - Monochromatic Waves

Figure 5.4 depicts the geometrical configuration of device type 2 and the finite element grid used. The device is very similar to device type 1 in a water depth of h=2a and draft of l_d=0.5a, with the exception of the back wall extending down to the sea floor. The finite element grid consists of 120 elements (770 nodes) distributed over three vertical and three radial layers. The interior OWC fluid (to a water depth h=0.5a) were discretized with 24 elements, including 40 device boundary faces of which 24 were used to represent the internal rigid surface and 16 for the internal walls. The exterior walls (to a water depth of h=0.5a) was represented by 16
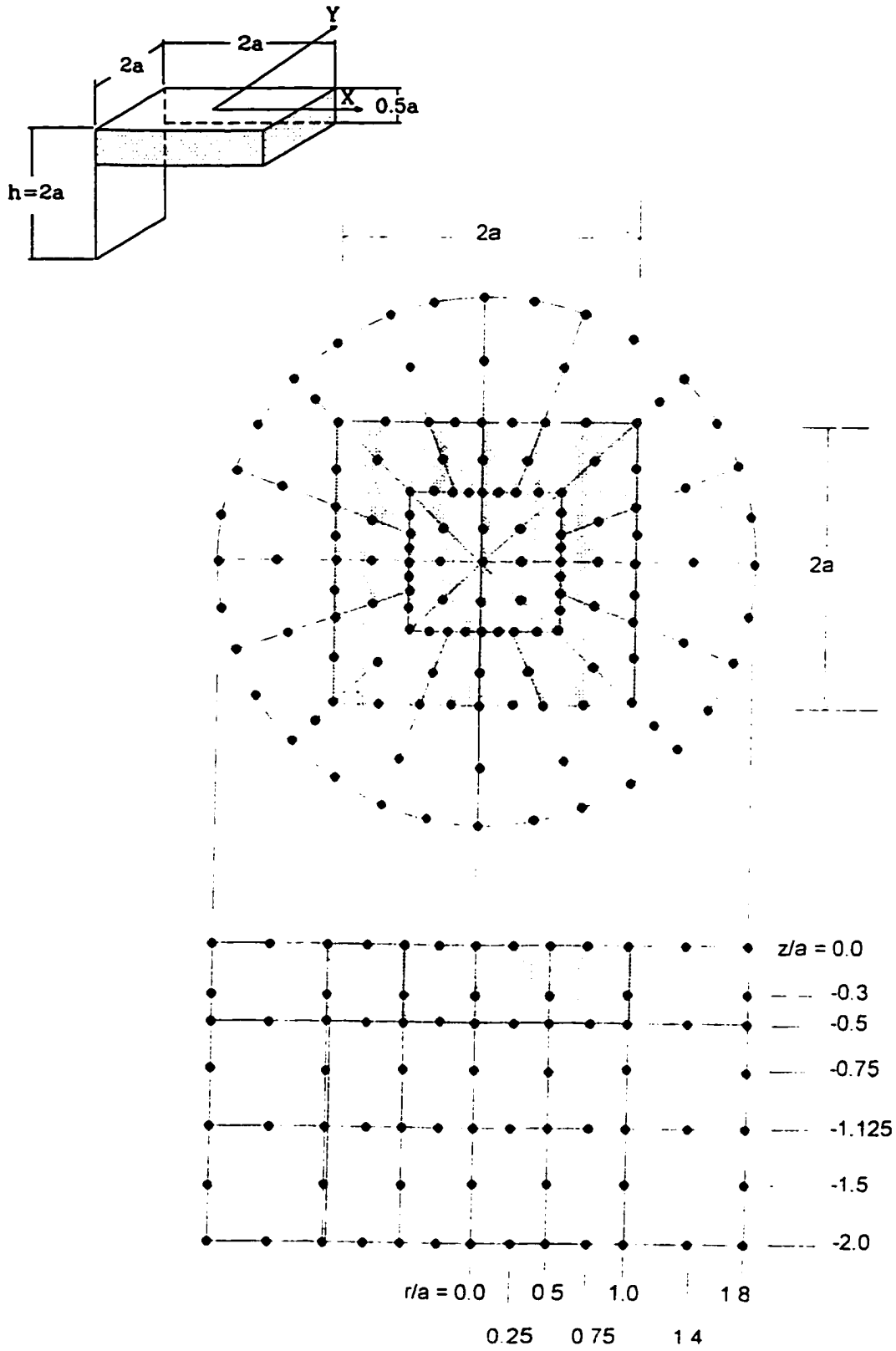
Figure 5.4. Finite Element Grid for Device Type 2
$(l_x=l_y=l_z=2.0)$

boundary faces and the addition of the back wall by 8 internal boundary faces and 8 external boundary faces.

Figure C.4 presents the finite element results for the non-dimensional coefficients of C_z (upper figure) and non-dimensional coefficients of μ and b_r (lower figure) for a range of ka values between 0.1 to 6.0. The device resonant conditions occur when the term $4 - \dfrac{4\pi^2}{(W_T)^2_{res}}\mu = 0$ and is satisfied when ka=0.985 and μ=4.2. The non-dimensional applied damping (b_a) was set equal to the non-dimensional radiation damping (b_r) at resonant conditions (i.e. $b_a = b_r = 0.91$) to optimize the power extraction and ensure the least drop in device performance.

Figure 5.5 presents the capture width ratio curves for the incident wave directions of θ_w = 0°, 22.5°, 45°, 67.5° and 90°. A comparison between the performance of the type 1 and type 2 devices clearly shows the advantage of extending the back wall to the seafloor. The back wall effectively increases the internal water column pressures by preventing a significant portion of wave energy from passing by the device. The effects of wave directionality on device performance are summarized in point form below:

(1)   The peak capture width ratio occurs for the incident wave direction of $\theta_w = 0°$ and this peak performance decreases with increased wave direction.

(2)   Incident wave directions between the range of 45° to 90° show a significant reduction in performance due to the energy lost by an attenuating wave past the device.
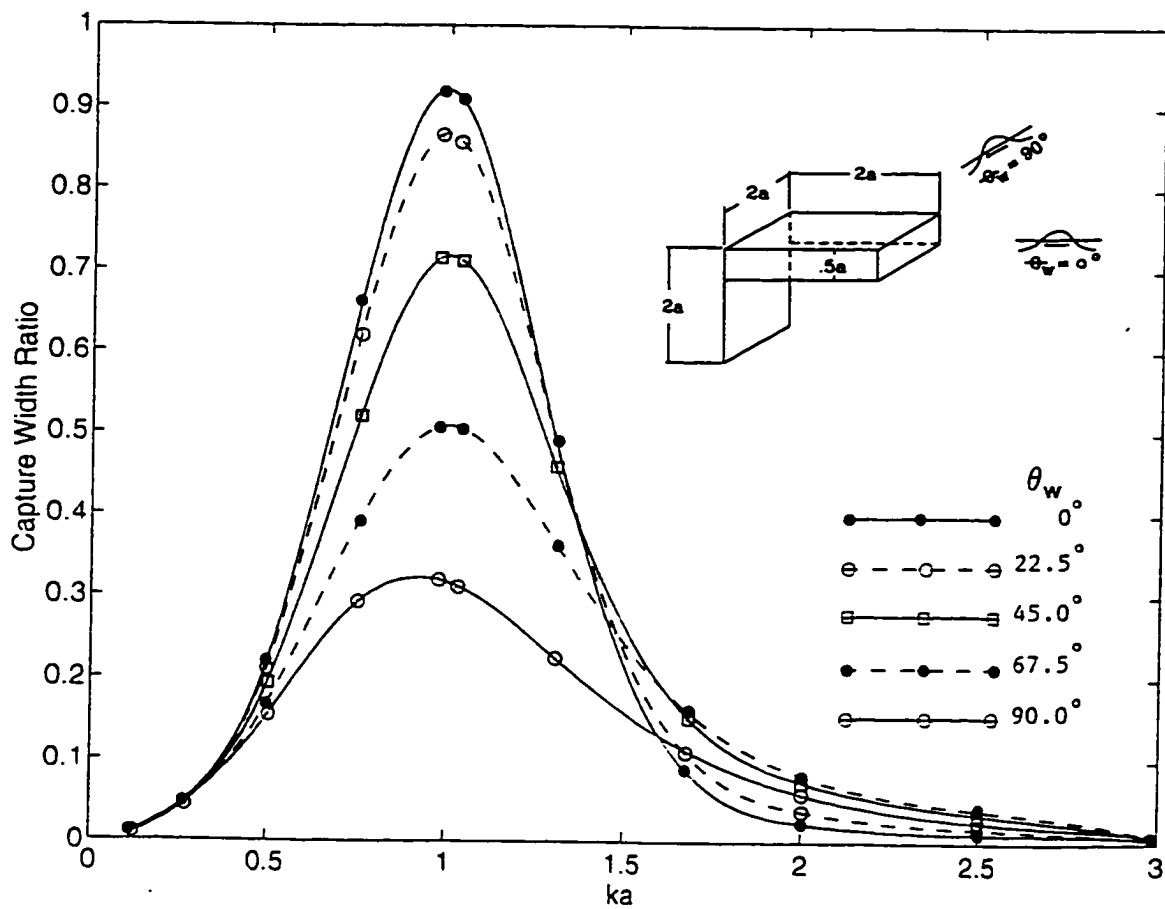
Figure 5.5. Variation in Capture Width Ratio with
Incident Wave Direction for Device Type 2

5.5   Device Type 3 - Monochromatic Waves

Device type 3 is very similar to device type 2 but with the addition of two half side walls which extend down to the seafloor. Figure 5.6 presents the geometrical configuration of device type 3 and the finite element mesh used to describe the interior and exterior fluid domain. The mesh consist of 120 elements (802 nodes distributed over 3 vertical layers and 3 radial layers. The bottom of the interior surface plate is defined by 24 boundary faces whereas both the interior and exterior walls are defined by 32 boundary faces each.

The non-dimensional coefficient of diffraction force (C_z) is presented in Figure D.5 (upper figure) for ka values between 0.1 to 6 and the incident wave directions of $\theta_w=0°$, 22.5°, 45°, 67.5° and 90°. The lower figure in Figure C.5 presents the non-dimensional coefficients of heave added mass (μ) and radiation damping (b_r).

Resonant conditions for device type 3 occur when the expression $4-\dfrac{4\pi^2}{(W_T)^2_{res}}\mu = 0$, and is satisfied for ka=0.75 and μ=5.86. For optimum device performance, the applied damping was set equal to the radiation damping at resonant conditions, such that $b_a=b_r=1.43$. Figure 5.7 presents the performance curves of device type 3 for the incident wave directions of $\theta_w = 0$, 22.5, 45, 67.5 and 90°. As can be seen from the figure, a further improvement in device performance occurs by the addition of the two half side walls. Peak capture width ratios for individual wave directions in the range of 0 to approximately 30° are in excess of unity and demonstrates the importance of wave diffraction effects for isolated 3-dimensional wave energy devices. The partial enclosure of the interior water column has the effect of not only increasing the internal water column pressures (as is evident by the comparison between device types 2 and 3 vertical diffraction force curves) but increases the added mass associated with the heaving
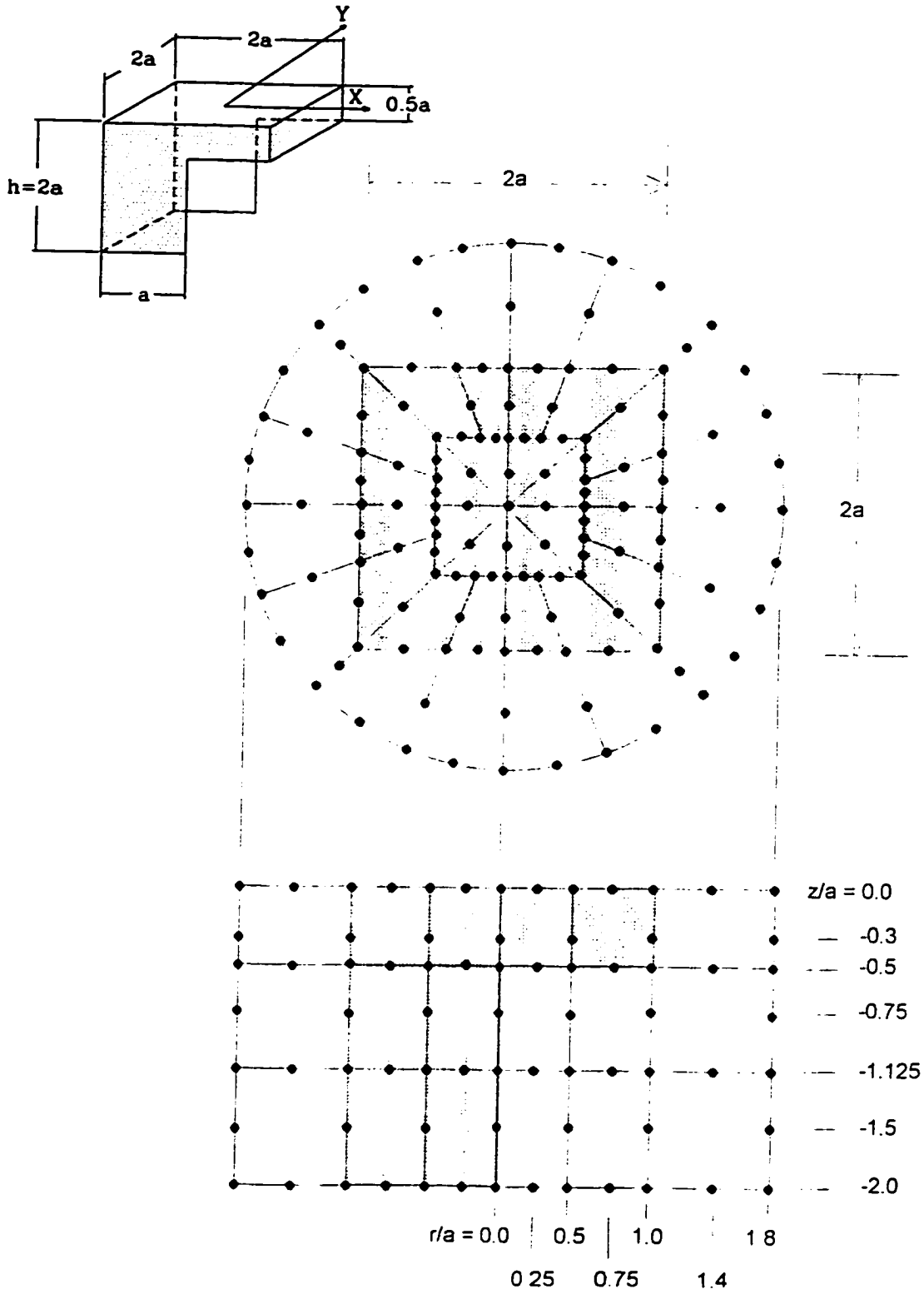
Figure 5.6. Finite Element Grid for Device Type 3
$(l_x=l_y=l_z=2.0)$
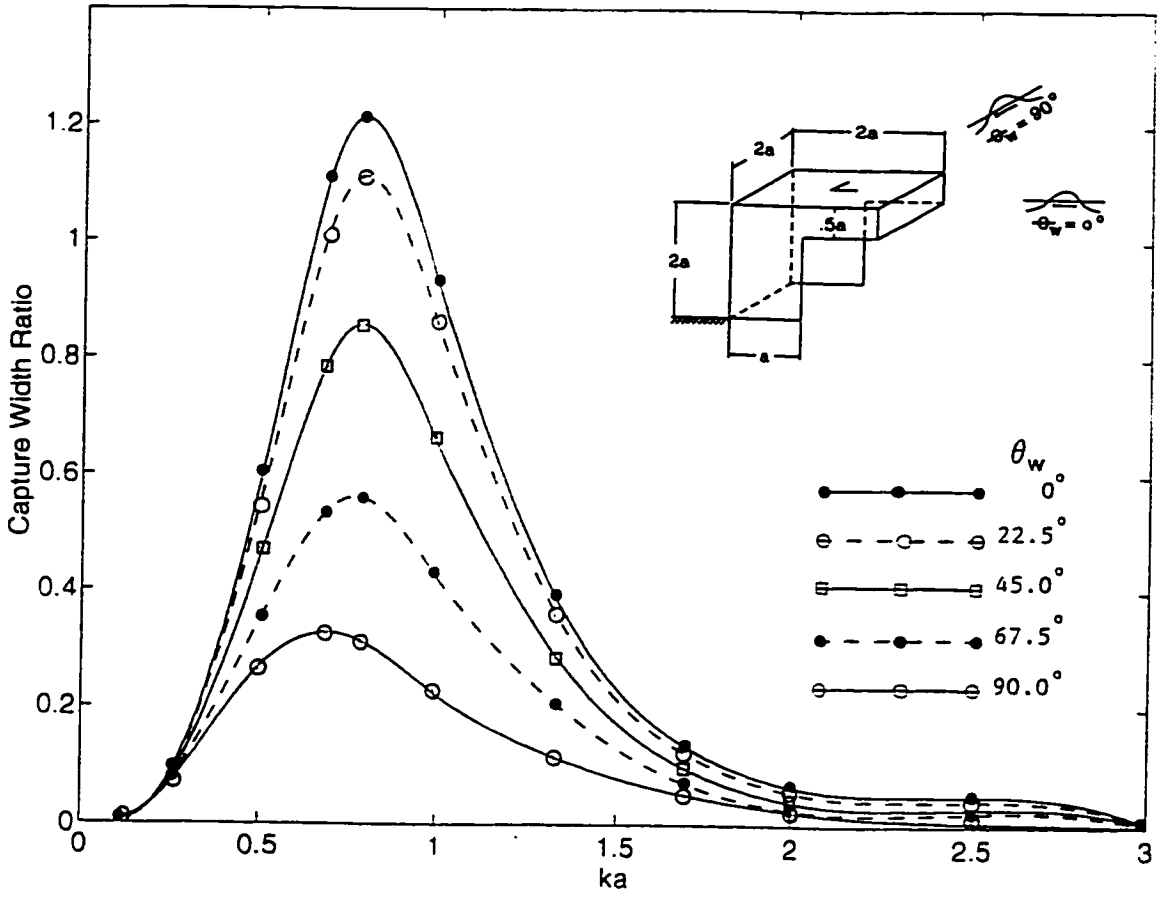
Figure 5.7. Variation in Capture Width Ratio with
Incident Wave Direction for Device Type 3

internal plate. This additional mass of fluid has the effect of shifting the resonant conditions to a lower frequency which has a positive effect on device performance because at these lower frequencies, the vertical diffraction force is greater (i.e. C_z increases with decreasing ka values).

5.6   Device Type 4 - Monochromatic Waves

Figure 5.8 presents the geometrical configuration of device type 4 and the finite element mesh used. The device consists of a back wall and two side walls which extend down to the seafloor. The finite element grid consists of 120 elements (834 nodes) distributed over 3 vertical and 3 radial layers. The interior fluid region of the device was discretized with 72 elements and 64 device boundary faces (i.e. 24 faces on the internal surface plate and 40 faces on the interior walls). The exterior fluid region (between the device and the artificial cylindrical FE boundary) consists of 48 elements with 40 boundary faces on the exterior walls of the device. Figure C.6 presents the non-dimensional coefficients of μ, b_r and C_z for the range of ka values between 0.1 to 6.0 and incident wave directions of $\theta_w = 0°$, $22.5°$, $45°$, $67.5°$ and $90°$. At resonant conditions, the expression $4 - \dfrac{4\pi^2}{(W_T)^2_{res}} \mu = 0$ is satisfied when ka=0.52 and $\mu = 9.83$. For optimum power extraction at the resonant frequency, the applied damping was set equal to the radiation damping $b_a = b_r = 2.25$. The corresponding performance curves for these conditions are presented in Figure 5.9.

Resonant conditions for device type 4 occurs at a lower ka value than previous device types due to the increased added mass associated with trapping the internal fluid by the addition of two full side walls.
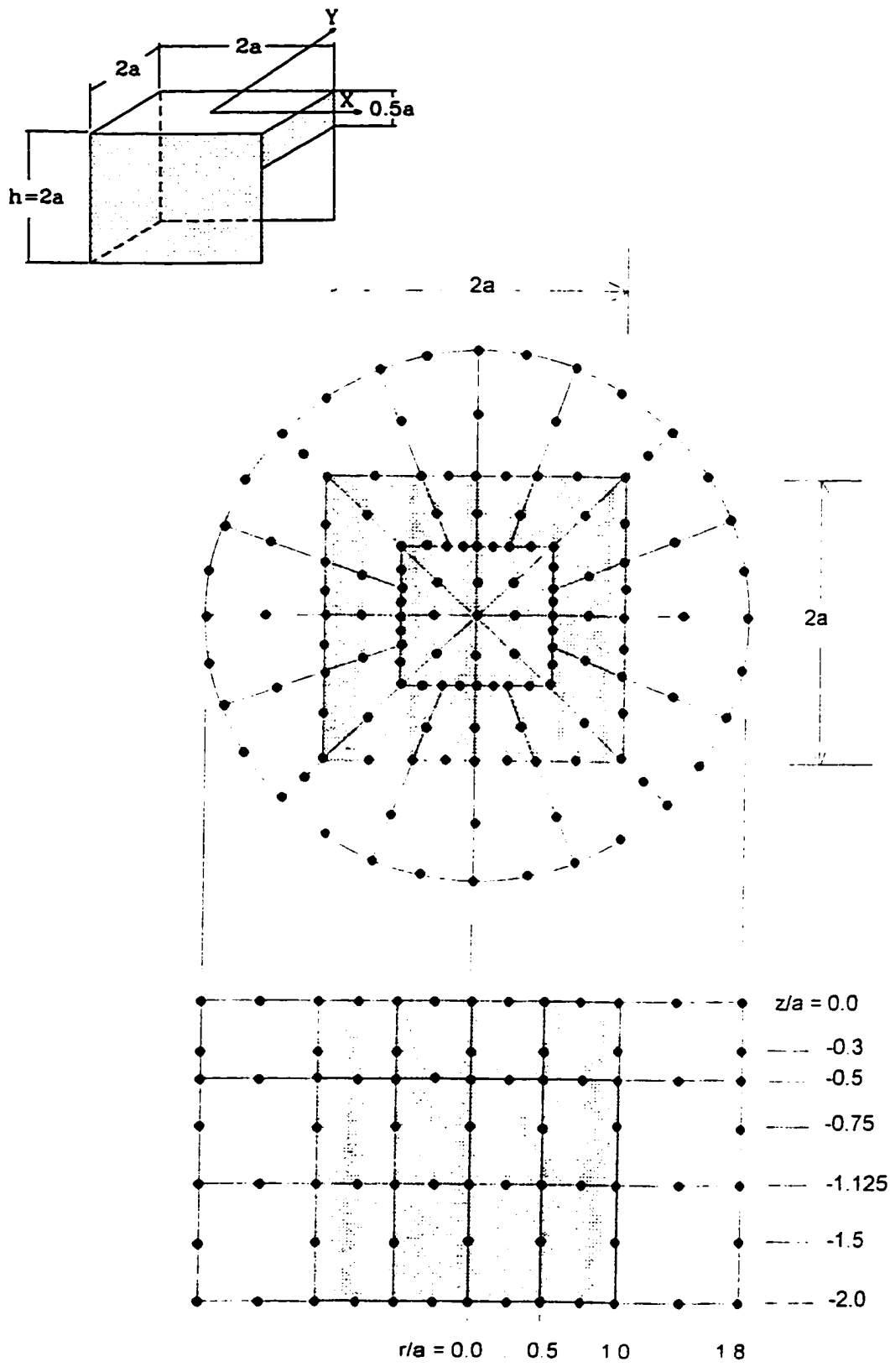
Figure 5.8. Finite Element Grid for Device Type 4
$(l_x = l_y = l_z = 2.0)$
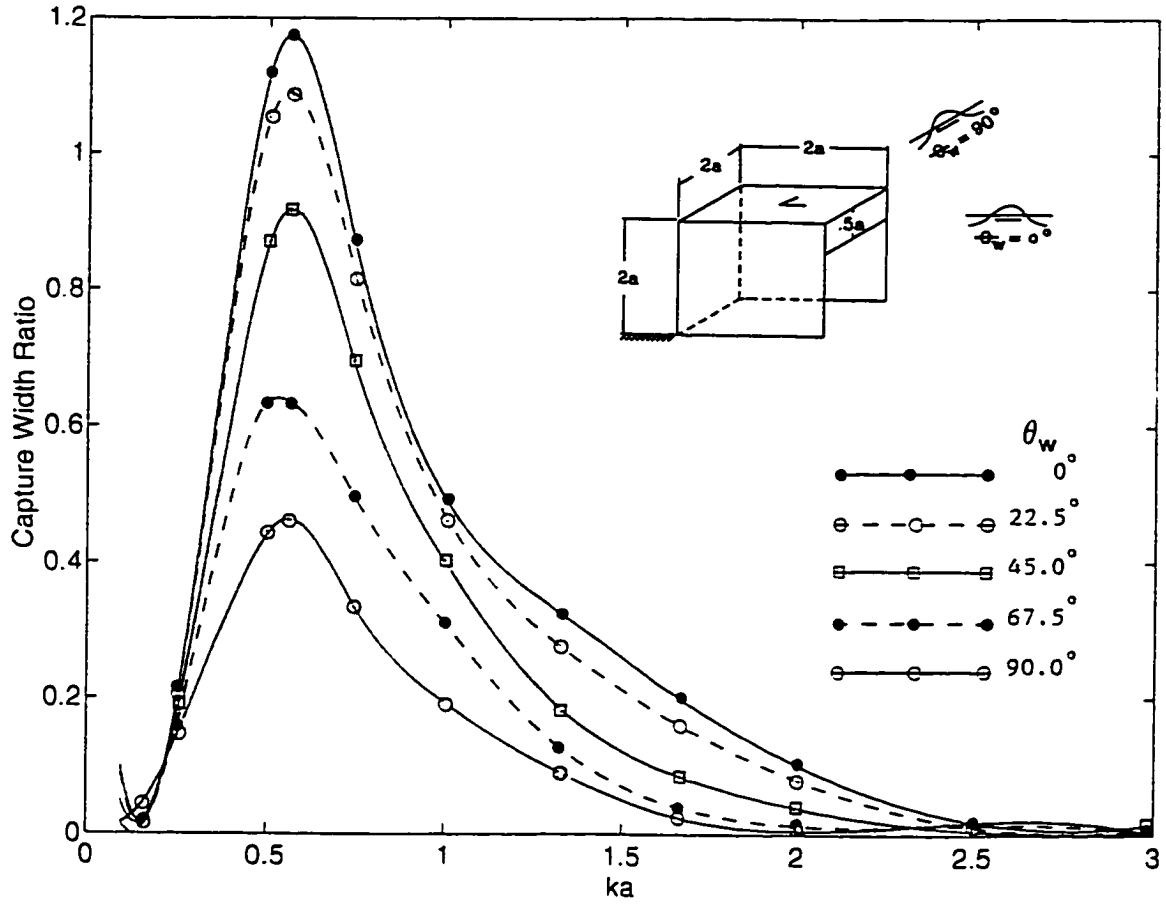
Figure 5.9. Variation in Capture Width Ratio with
Incident Wave Direction for Device Type 4

A comparison between the performance results for device type 4 and device type 3 show that the peak CWR of device type 4 is slightly lower for incident wave directions between 0 to 22.5° and larger for incident wave directions between 22.5° and 90°. These are interesting results and show that the optimum performance of a square device is not necessarily achieved by adding a back wall and two full side walls. Although the internal water column pressures at resonant conditions and incident wave directions between 0 to 22.5° are greater for device type 4 than device type 3, the peak performance of the device are controlled by both the applied damping ($b_a = b_r$) and vertical diffraction force (C_z), and the combination of these two parameters produced the reduced performance.

5.7 Device Type 5 - Monochromatic Waves

Figure 5.10 presents the geometrical configuration of device type 5 and the finite element mesh used. This type of device was chosen to further quantify the result that the optimum performance of a square OWC device is not necessarily achieved by extending the side walls to the full device length (i.e. device type 4). The finite element grid consists of 120 elements (802 nodes) with a total of 24 boundary faces on the interior surface plate, 32 boundary faces on the interior walls, and 32 boundary faces on the exterior walls of the device.

Resonant conditions for device type 5 are similar to device type 3 (due to the equal vertical wall areas) and occur when ka$=0.756$ and $\mu = 5.82$. For optimum power extraction at the resonant frequency, the applied damping was set equal to the radiation damping such that $b_a = b_r = 1.51$. The numerical radiation/diffraction results for the non-dimensional coefficients of C_z, μ, and b_r are given in Figure C.7. The corresponding performance curves for device type
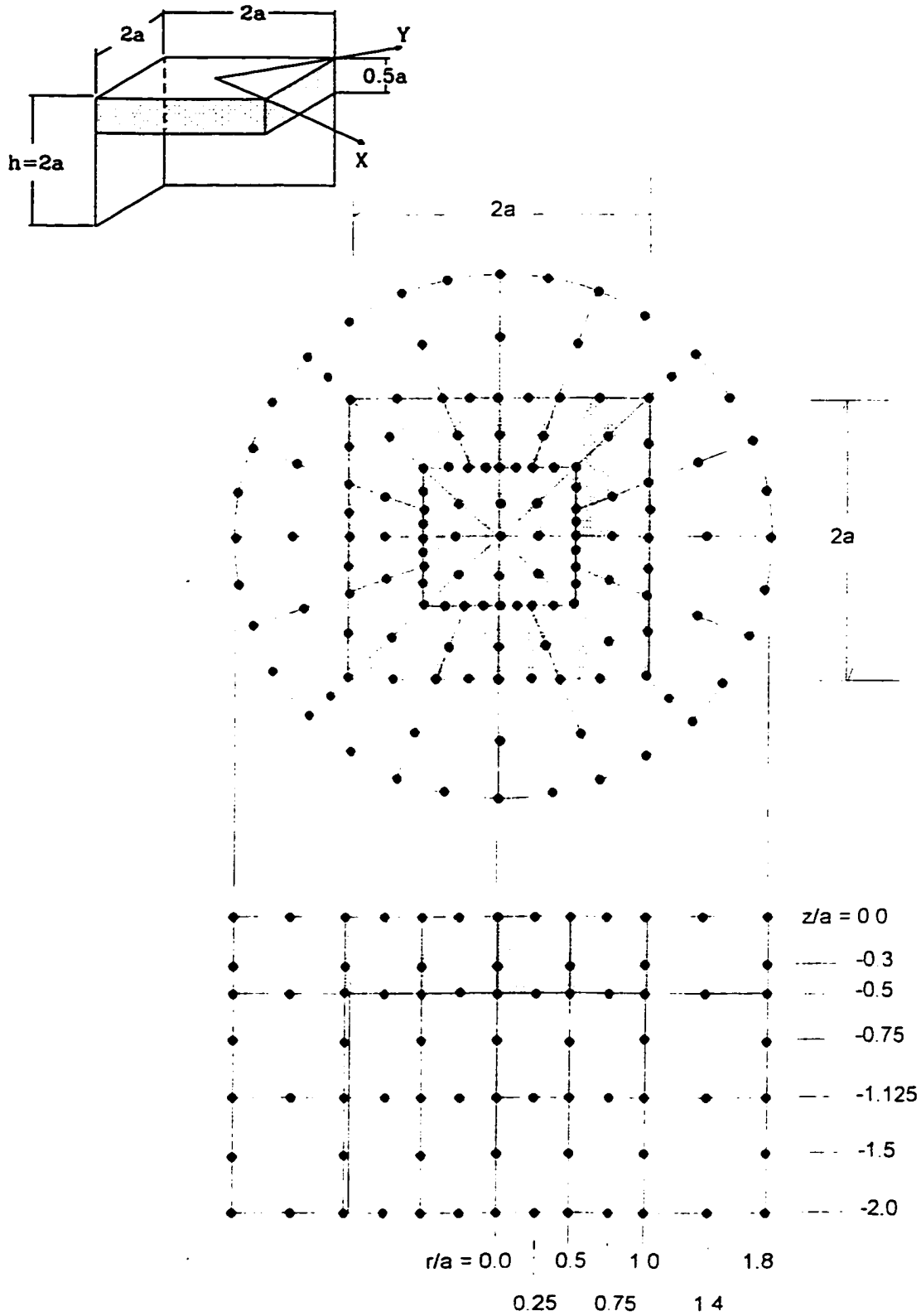
Figure 5.10. Finite Element Grid for Device Type 5
$(l_x = l_y = l_z = 2.0)$

5 are presented in Figure 5.11 for the incident wave directions of $\theta = 0°$, 22.5°, 45°, 67.5°, and 90°.

In order to compare the relative performance of the different device types, the capture width ratio given in Figure 5.11 was defined (as in previous device types) by a device length of 2a and not the projected length of 2.83a (i.e. $\sqrt{(2a)^2 + (2a)^2}$).

The performance curves depicted in Figure 5.11 clearly demonstrates that improved device performance is attainable by extending only two vertical walls to the seafloor. More importantly, a comparison between the peak performance of device types 4 and 5 shows that this improved performance occurs for incident wave directions in the range of 0° to 45°, thereby improving the response over a wider directional band.

5.8   Device Type 6 - Monochromatic Waves

Figure 5.12 presents the geometrical configuration of device type 6 and the finite element mesh used. The concept of extending the two side walls in front of the device was first proposed by Ambli et al. (1982). By projecting two parallel side walls in front of the OWC device they showed that the performance is considerably improved by introducing additional resonances that effectively broadens the frequency response.

The finite element grid consists of 120 elements (834 nodes) of which 36 elements are distributed over 3-layers below the internal surface plate and an additional 36 elements distributed over 3-layers outside of the device between the two parallel projected side walls. The radiation/diffraction results for the non-dimensional coefficients of C_z, μ, and b_r are given in Figure C.8 for the incident wave directions of $\theta_w = 0°$, 22.5°, 45°, 67.5°, and 90°.
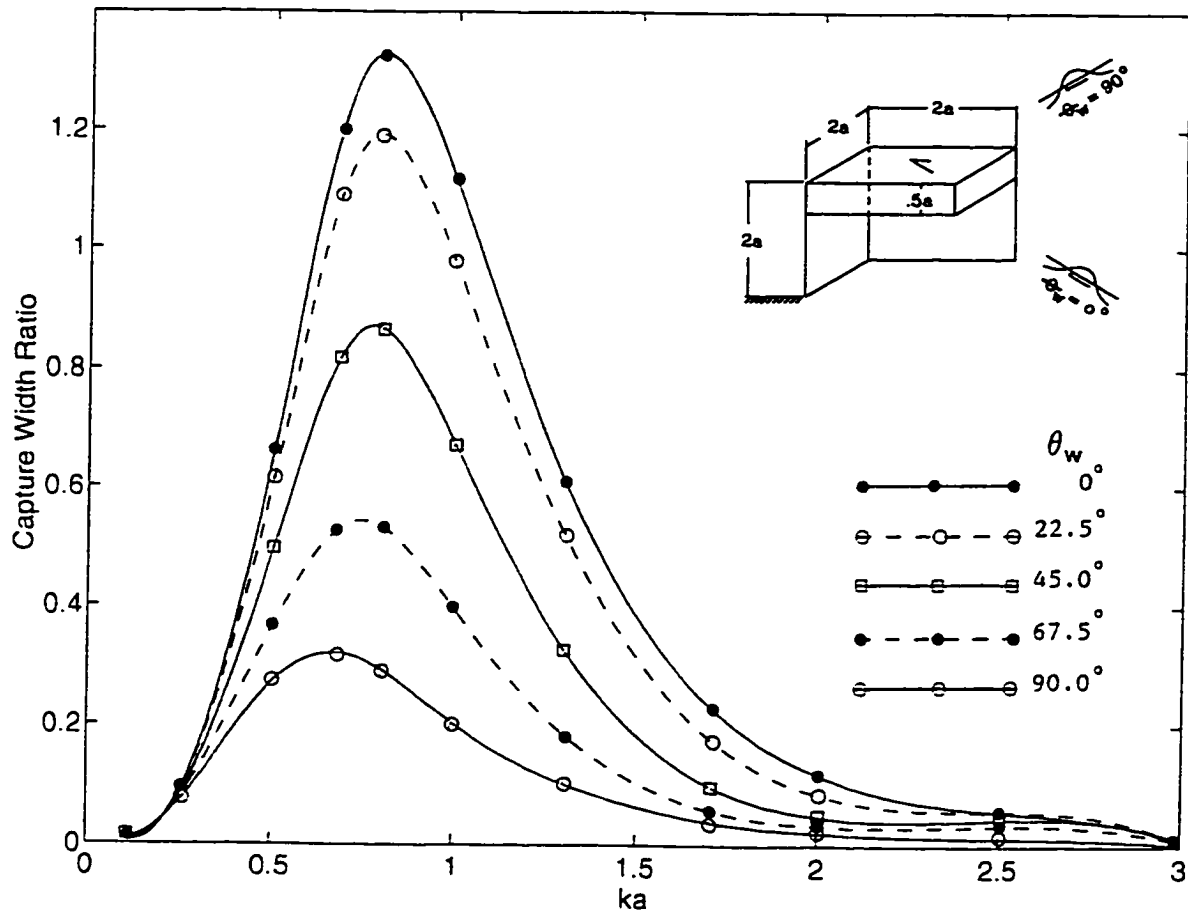
Figure 5.11. Variation in Capture Width Ratio with
Incident Wave Direction for Device Type 5
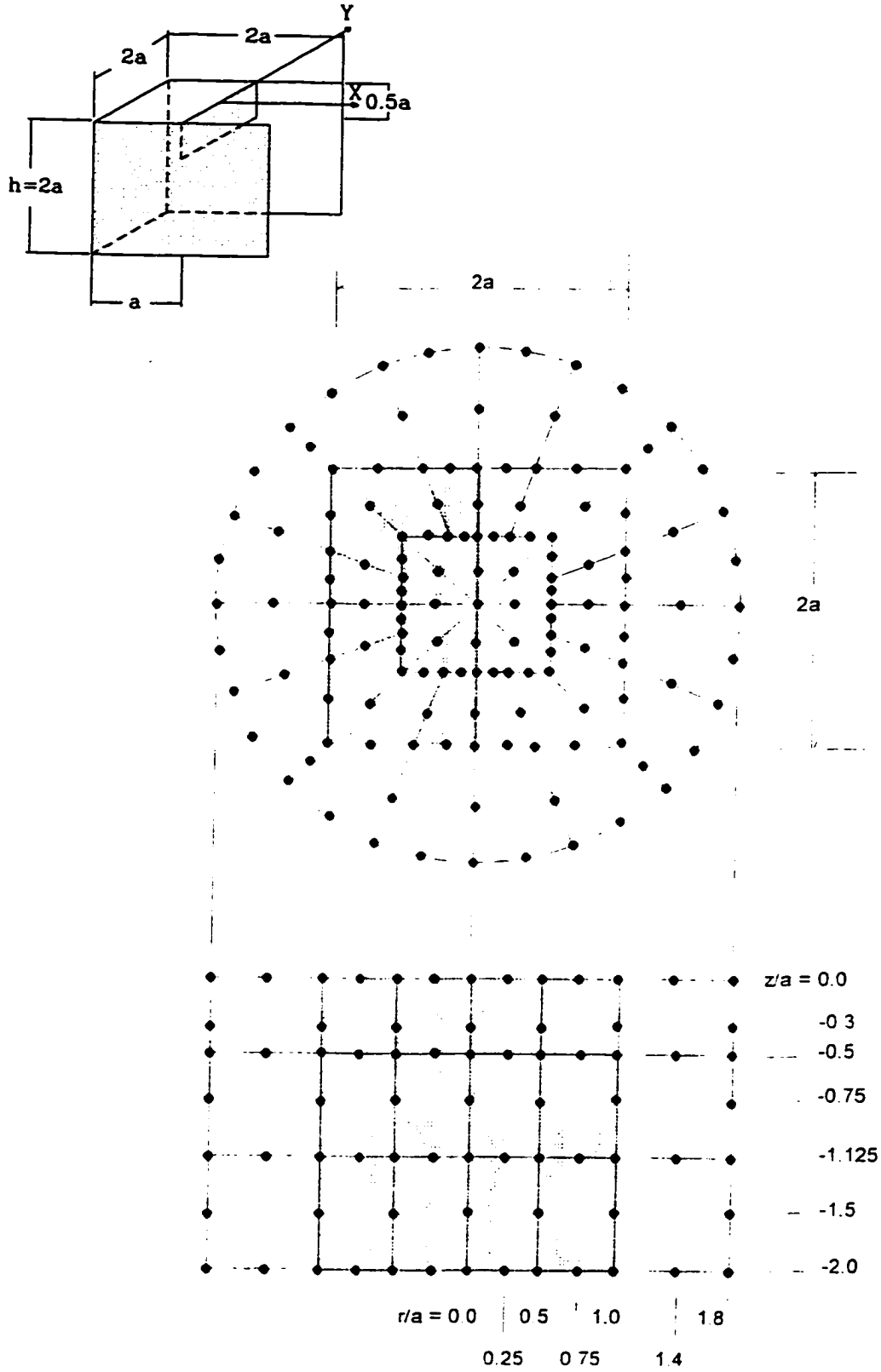
Figure 5.12. Finite Element Grid for Device Type 6
$(l_y = l_z = 2.0, l_x = 1.0)$

The resonant conditions for device type 6 occurs when the expression $2.0 - \dfrac{4\pi^2}{(W_T)_{res}^2} \mu = 0$ and is satisfied for two distinct frequencies;

Resonant Frequency #1 $ka=0.59$, $\mu=4.10$, $b_r=1.59$

Resonant Frequency #2 $ka=1.01$, $\mu=2.06$, $b_r=1.79$

As in the previous device types, optimum power extraction occurs when the applied damping (b_a) is set equal to the radiation damping at the resonant frequency. Of the two distinct frequencies, the first resonant frequency produces the largest peak response (i.e. maximum CWR) and therefore was chosen for optimization, such that $b_a=b_r=1.59$. The performance curves based on these conditions are given in Figure 5.13. As evident by the performance curves, the finite element method coupled together with the analytical model for power extraction predicted the additional resonance associated with the projected side walls. The effect of this additional resonance on device performance is that the frequency response is significantly broadened. Although a reduction in performance is apparent for increased incident wave directions, the relatively broad bandwidth is still maintained.

5.9 Comparison of Various OWC Device Types

A comparison of the performance for the various OWC device types (types 1 through 6) are presented in Figure 5.14. The upper figure presents the frequency response curves for an incident wave direction of $\theta_w=0°$ and the lower figure presents the variation in the maximum capture width ratio with incident wave direction.
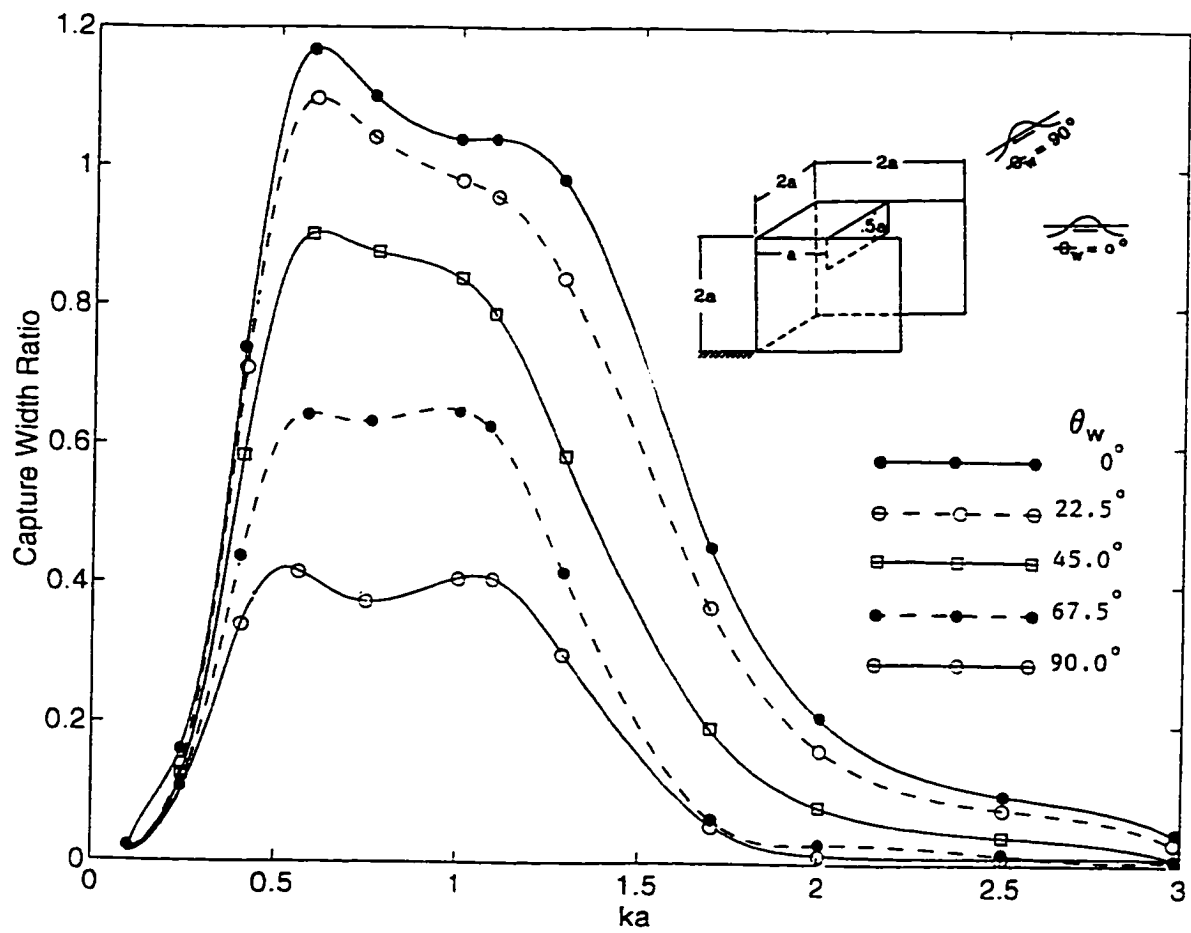
Figure 5.13. Variation in Capture Width Ratio with
Incident Wave Direction for Device Type 6
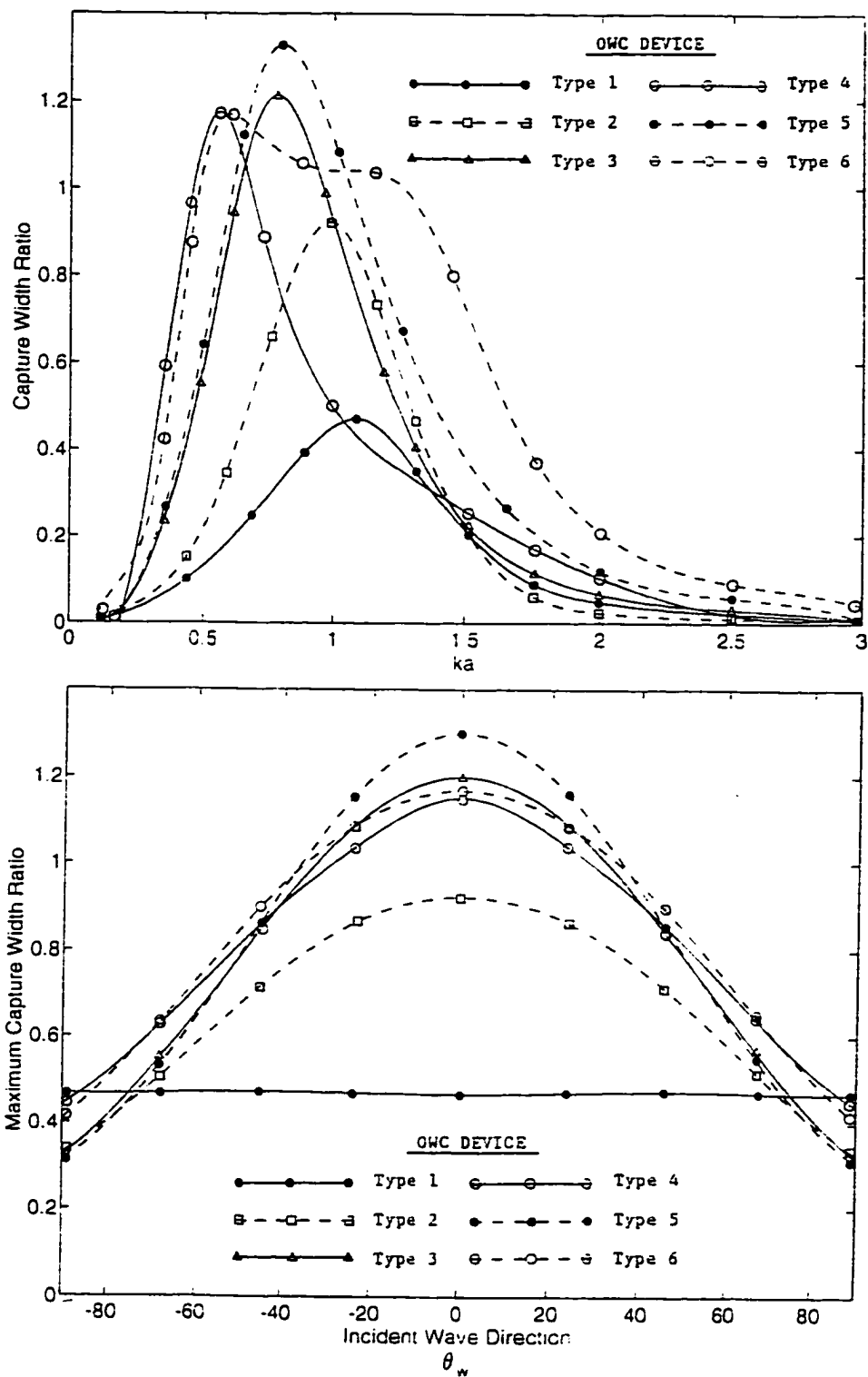
Figure 5.14. Comparison of the Various OWC Device Types
(Upper figure presents the frequency response for $\theta_w = 0°$
and the lower figure depicts the variation in
maximum CWR with wave direction.)

The upper figure clearly demonstrates that the frequency response curves are quite different for the various device types and show a wide variability in both the resonant frequency and peak performance. Table 5.2 summarizes the resonant conditions for the different device types and, as would be expected, the added mass of the internal surface plate is influenced by the geometrical configuration of this device and in turn has a direct effect on the resonant frequency.

Table 5.2 Summary Resonant Conditions
for the Various Device Types

Device Type	ka	μ	Device Type	ka	μ
1	1.120	3.65	4	0.520	9.83
2	0.985	4.20	5	0.756	5.82
3	0.750	5.86	6	0.59	4.10

It is interesting that device type 5 (a device not previously investigated) has the largest peak CWR for ka values in the range between 0.65 to 1.10 and incident wave directions between -35° to +35°. However, this response is relatively narrow banded when compared to the broad banded response of device type 6.

It is rather unfortunate that the performance of device types 2 through 6 show reductions in the maximum CWR for incident wave directions outside the range of -40 to +40° and surprisingly with very little variance. For incident wave directions of $\theta_w = \pm 90$, these devices have a maximum CWR less than the simple attenuator device (type 1).

5.10   Verification of Model to Experimental Results

The accuracy of the present method is examined by comparing the 3-dimensional numerical results with data from the following two experimental tests: 1) Resonant conditions for a cylindrical attenuator type oscillating water column, and 2) Wave power extraction for a rectangular terminator type oscillating water column. A description of these two experimental tests and the computational methods applied are described in the next two sections.

5.10.1   Verification of Resonant Conditions for a Cylindrical Attenuator Type OWC

The experimental tests for the cylindrical type OWC were carried out at the Technical University of Nova Scotia (TUNS) wave tank. The physical dimensions of the wave tank are 1-metre wide and 30 metres in length, and contains a computer controlled wave maker and absorber to generate single frequency or a spectrum of unidirectional waves. A cylindrical, hollow vertical tube 0.305 metres in diameter, with an open top and bottom was used to represent the attenuator type OWC. Single frequency harmonic waves were generated in the tank and the exterior wave height and internal free surface response recorded by a set of capacitance wave gauges. The capacitance gauges were calibrated by placing the instruments in the tank and measuring the change in voltage for a range of vertical displacements in still water. A linear regression analysis was performed to determine the best-fit curve for the controlled measurements. The linear regression of the interior capacitance gauge was found to be $y = 14.078 \, x - 22.062$ with a correlation Corr $(x,y) = 0.9991$. The linear regression of the exterior capacitance gauge was $y = 13.569 \, x - 20.236$ with a correlation Corr $(x,y) = 0.9994$, where x and y are the measured

displacement (inches) and voltage (volts), respectively. The internal frequency response was recorded at a sampling frequency of 20 Hz for four different normalized drafts, $l_d/a=0.66$, 1.0, 1.33, and 1.67, where l_d is the draft length and a is the radius of the cylinder. The natural frequency (f_{res}) of the device was determined experimentally by recording the frequency which produced the maximum normalized internal free-surface response (ξ_o/α_o), where α_o is the wave amplitude and ξ_o is the amplitude of the internal free-surface.

Harmonic regular waves with frequencies varying between 0.70 Hz to 2.0 Hz, and a wave height of 10 cm were used in the experiment test cases. An iterative procedure was used to determine the experimental frequencies which produced the maximum internal free-surface response during steady-state conditions. To minimize the backscattering of waves from the wave-maker and wave-absorber, the cylindrical device was securely placed in the centre of the tank, which allowed a steady-state internal response for approximately 10 seconds. The average frequency recorded by the internal capacitance gauge time-series during this 10 second period was used to compute the natural frequency of the OWC device for a particular draft length. Figure 5.15 illustrates the finite element idealization of the cylindrical attenuator type OWC for the normalized drafts, $l_d/a=0.25$, 0.5, 1.0 and 2.0. The non-dimensional amplitude of oscillation (ξ_o/α_o) of the internal surface with no applied damping ($b_a=0$) is given by

$$\left(\frac{\xi_o}{\alpha_o}\right) = \frac{C_z}{\left(\left(\alpha_1 - \frac{4\pi^2}{W_T^2}\mu\right)^2 + \left(\frac{2\pi}{W_T}b_r\right)^2\right)^{1/2}} \tag{5.9}$$

where $\alpha_1 = \pi$ for a cylindrical internal surface. A range of wave frequencies were numerically run to determine the resonant frequency which produces the maximum amplitude of oscillation. Table 5.3 summarizes the resonant conditions for the various normalized draft lengths.
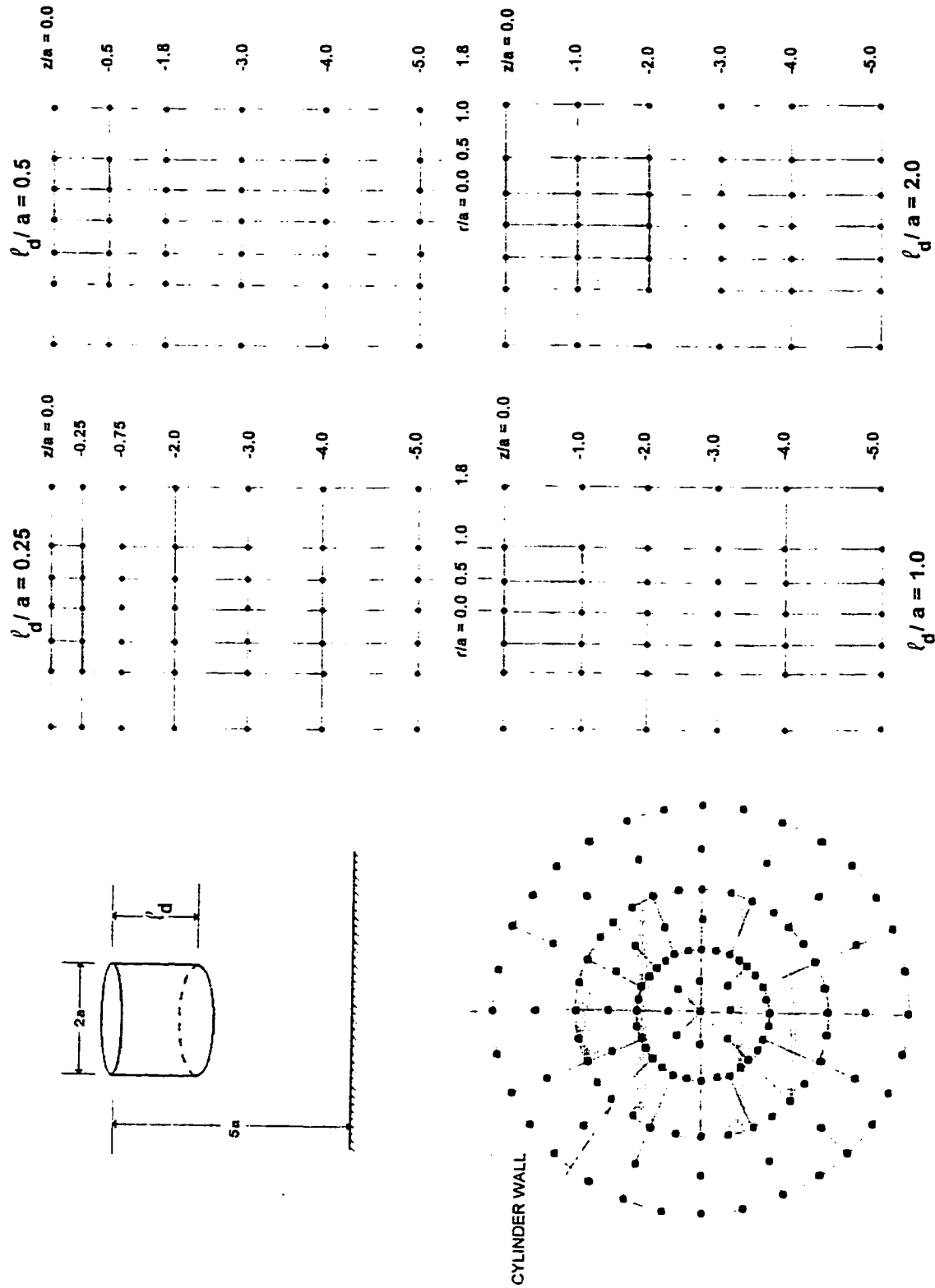
Figure 5.15. Finite Element Mesh for the Cylindrical OWC Device with Normalized Drafts ($\frac{l_d}{a}$ = 0.25, 0.5, 1.0 and 2.0)

Table 5.3. Resonant Conditions for a Cylindrical Attenuator
Type OWC with Varying Drafts

Normalized Draft L_d/a	Natural Frequency f_{res}(Hz)	Non-Dimensional Added Mass μ
0.25	1.40	1.30
0.50	1.14	2.89
0.75	1.02	3.68
1.00	0.93	4.50
1.25	0.86	5.25
2.00	0.72	7.70

In Figure 5.16, the computational results are compared to the experimental test results. In addition to experimental results carried out in the TUNS wave tank, a similar experiment carried out by Long (1979) in a 1.5 metre wide wave tank and a device with the same characteristic dimensions as the TUNS experiment is also shown. The numerical data and both experimental data sets show good agreement for a wide range of dimensionless drafts. This is an important verification because it justifies the assumption that the internal free-surface can be replaced by a thin rigid plate which oscillates in the vertical (heave) direction with the side walls.

5.10.2 Verification of Wave Power Extraction for a Rectangular Terminator Type OWC

The second data set used for verification purposes was an experimental study carried out by Count et al. (1983) in a 20-metre wide wave tank at Gifford Technology, Cadnam. The experiments examined the performance of an isolated OWC device and an array of devices in regular and irregular wave conditions. This section describes the experimental procedure and presents a comparison of the experimental results with numerical results for the performance of an isolated terminator type device in regular wave conditions.
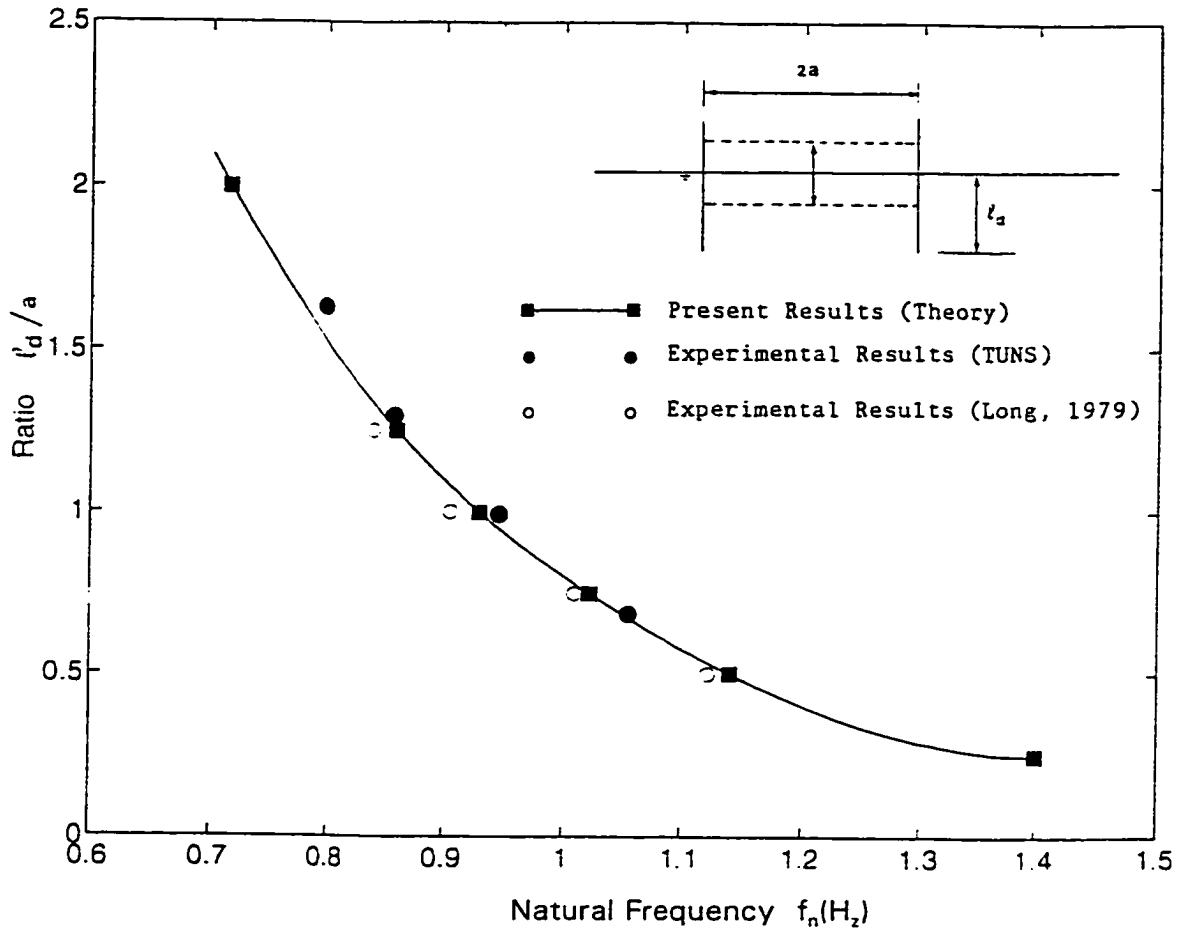
Figure 5.16. Natural Frequency of a Cylindrical OWC Device
with Various Submergence Depths

The geometrical configuration of the OWC device used in the experimental tests is given at the top of Figure 5.17 where the characteristic dimension, a, of the device is equal to 0.1 metres. The device was elevated approximately 20 cm above the tank bottom so that the device dimensions could be kept small enough for the practical range of experimental wave frequencies (i.e. 0.8 Hz to 1.5 Hz). The power absorbed by the device was through an orifice plate assembly at the top of the device which was calibrated to determine the pressure drop (ΔP) and flow (Q) characteristics. The relationship between ΔP and Q was of the form

$$\Delta P = \beta_1 Q|Q| + \beta_2 Q \qquad (5.10)$$

where β_1 and β_2 are constants dependent on the orifice size. The pressure measurements were monitored 20 times a second (0.05 Hz) and the average wave power absorbed by the device determined by

$$P_e = \frac{1}{N} \sum_{n=1}^{N} \Delta P(t_n) Q(t_n) \qquad (5.11)$$

where N is the total number of data points. A total of 2400 data points were averaged for each test and represents a 2-minute monitoring period. The performance of the device during the monitoring period was measured in terms of the capture width ratio, defined as

$$CWR = \frac{\text{Air Power Absorbed by Device}}{\text{Wave Power Absorbed on Device Width}} = \frac{P_e}{P(2a)} \qquad (5.12)$$

where 2a represents the device width and P represents the average incident wave power per unit frontage such that

$$P = \frac{\rho g^2 H^2 T}{32\pi} \left[1 + \frac{2kh}{\sinh 2kh} \right] \tanh kh \qquad (5.13)$$
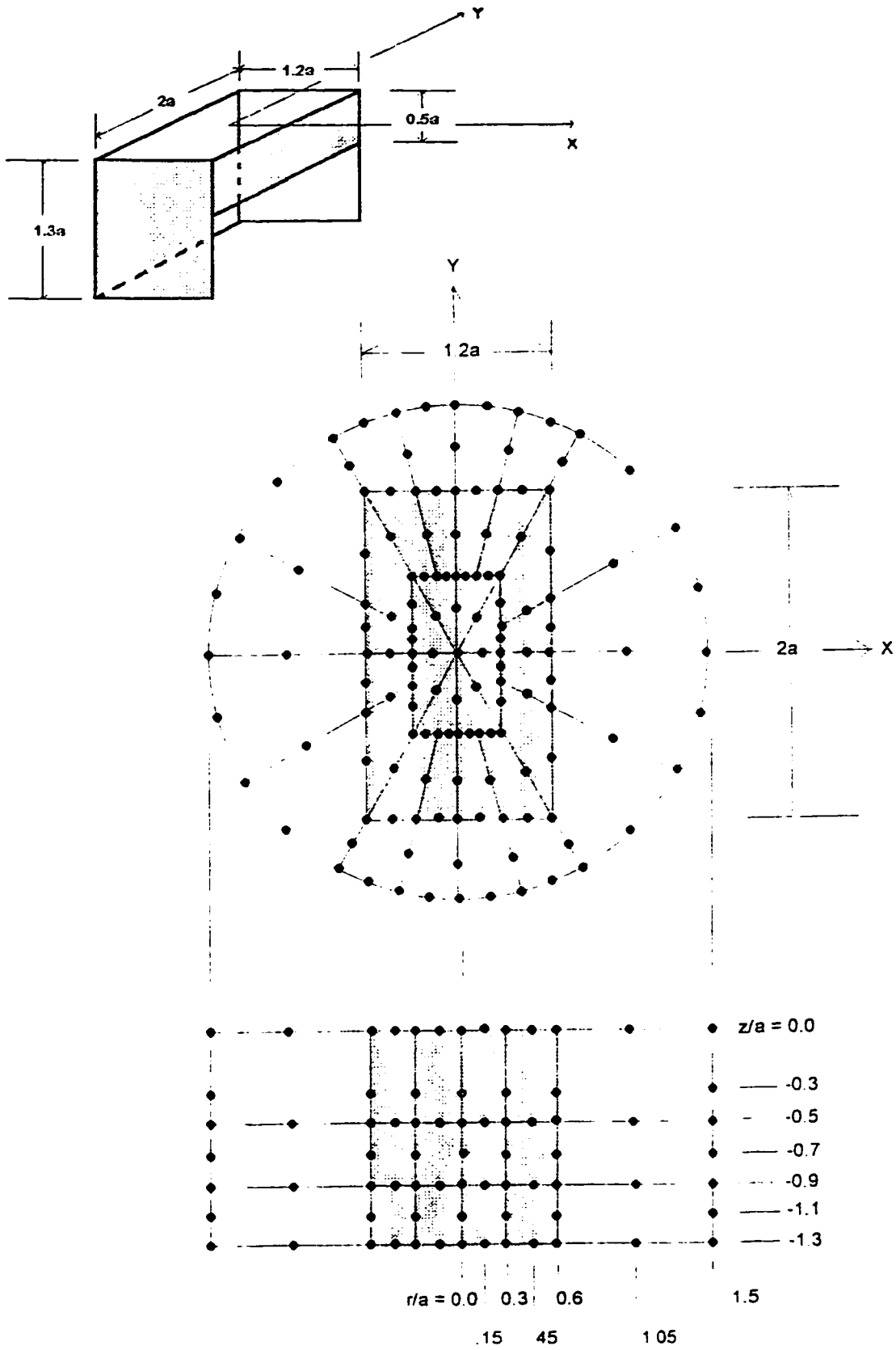
Figure 5.17. Finite Element Grid for the Experimental OWC Device used by Count et al. (1983)

and kh is related to the dispersion relationship

$$k_o h = kh \tanh kh$$

$$\text{where,} \quad k_o h = \frac{4\pi^2}{gT^2} h \tag{5.14}$$

The wave parameters H and T were recorded for each experimental test run and the performance of the device was then determined, with the results plotted in terms of a CWR for a given experimental wave frequency.

The finite element mesh used to describe the fluid within the artificial cylindrical boundary is given in Figure 5.17. A total of 120 elements (834 nodes) distributed over 3 radial and 3 vertical layers were used to numerically model the experimental device. The elevated block beneath the experimental OWC device was not numerically modelled due to the limitation of the radiation heave condition. Because the numerical method produces a forced heave oscillation of the device, any attached structure with an area in the x-y plane will also oscillate and create an additional added mass which is not related to the internal surface plate. However, because the actual device dimensions are identical for both the numerical model and experimental tests and that the performance is defined as a ratio of power extracted to incident wave power, similar performance curves would be expected.

The non-dimensional coefficients of C_z, μ and b_r were determined for a range of ka values between 0.1 to 3.0 (which incorporates the experimental frequency range) and are presented in Figure 5.18.
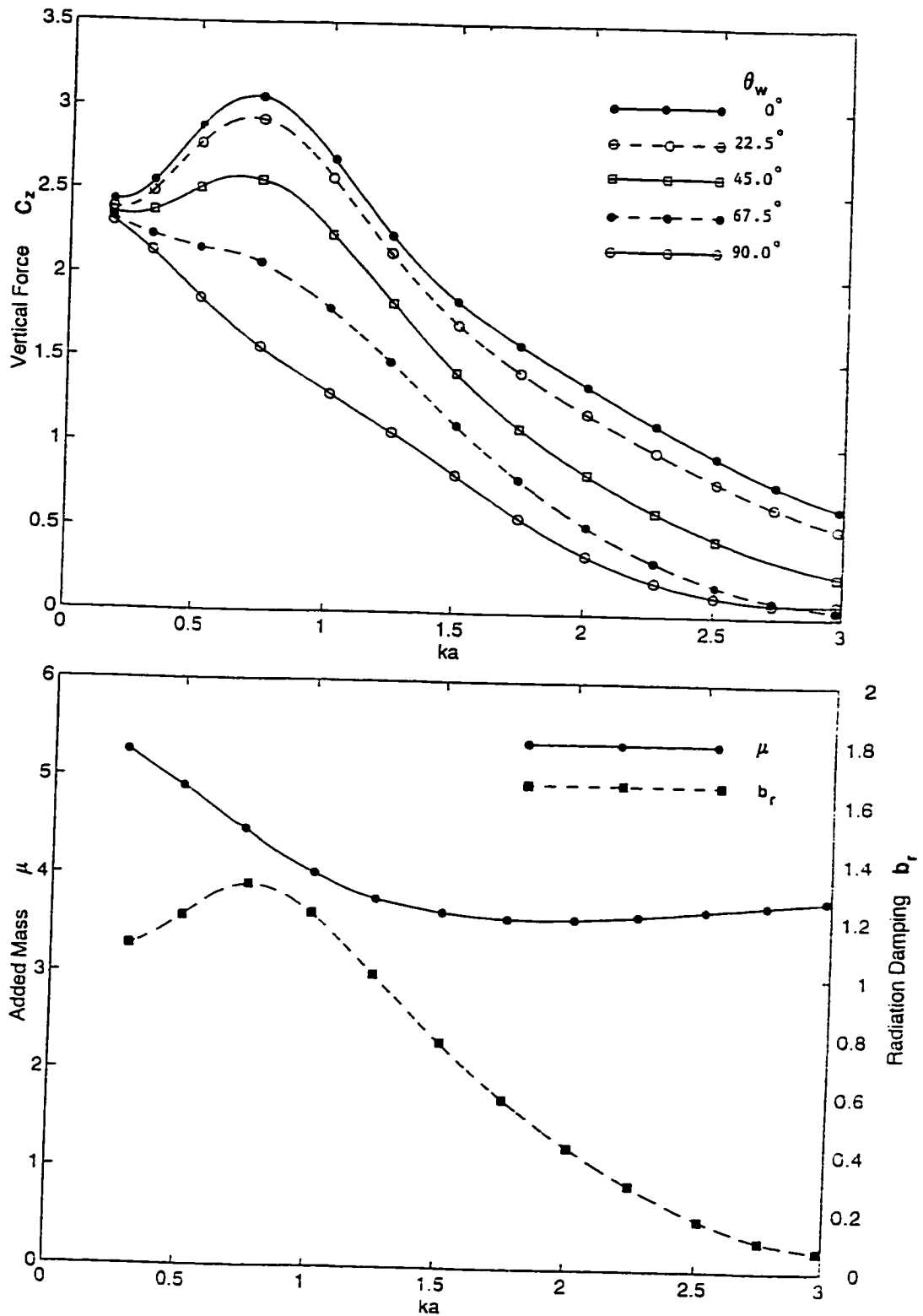
Figure 5.18. Non-Dimensional Coefficients of Vertical Diffraction
Force (C_z), Heave Added Mass (μ), and Radiation Damping (b_r)
for Count's (1983) Experimental OWC Device

The performance of the device is expressed in terms of the capture width ratio such that

$$CWR = \left(\frac{2\pi}{W_T}\right)^3 b_a \left(\frac{\xi_o}{\alpha_o}\right)^2 \frac{1}{\left[1 + \dfrac{2.6\,ka}{\sinh 2.6\,ka}\right]\tanh 1.3\,ka} \tag{5.15}$$

where

$$\left(\frac{\xi_o}{\alpha_o}\right) = \frac{C_z}{\left(\left(2.4 - \dfrac{4\pi^2}{W_T^2}\mu\right)^2 + \left(\dfrac{2\pi}{W_t}(b_a + b_r)\right)^2\right)^{1/2}} \tag{5.16}$$

The resonant conditions for the device occurs when the expression $2.4 - \dfrac{4\pi^2}{(W_T)^2}\mu = 0$ and is satisfied for $ka = 0.725$ and $\mu = 4.49$.

A comparison of the numerically computed optimized performance with the experimental results of Count et al. (1983) is given in Figure 5.19 for the incident wave direction of $\theta_w = 0°$. Figure 5.19 shows that the numerical and experimental results for device performance are in fairly close agreement for the range of experimental frequencies tested. It is also encouraging to see that both the numerical method and experimental tests show capture width ratios in excess of unity at the peak performance.

The numerical method predicts the response of the device quite well for the lower frequency waves, up to approximately 1.2 Hz, but shows a divergence from the experimental data for the higher frequency waves between 1.2 Hz to 1.5 Hz. Another apparent difference between the numerical and experimental data is the presence of two peaks in the experimental data and one relatively broad peak response for the numerical results. One possible explanation for these two differences is the difficulty of carrying out experimental testing of single-frequency harmonic
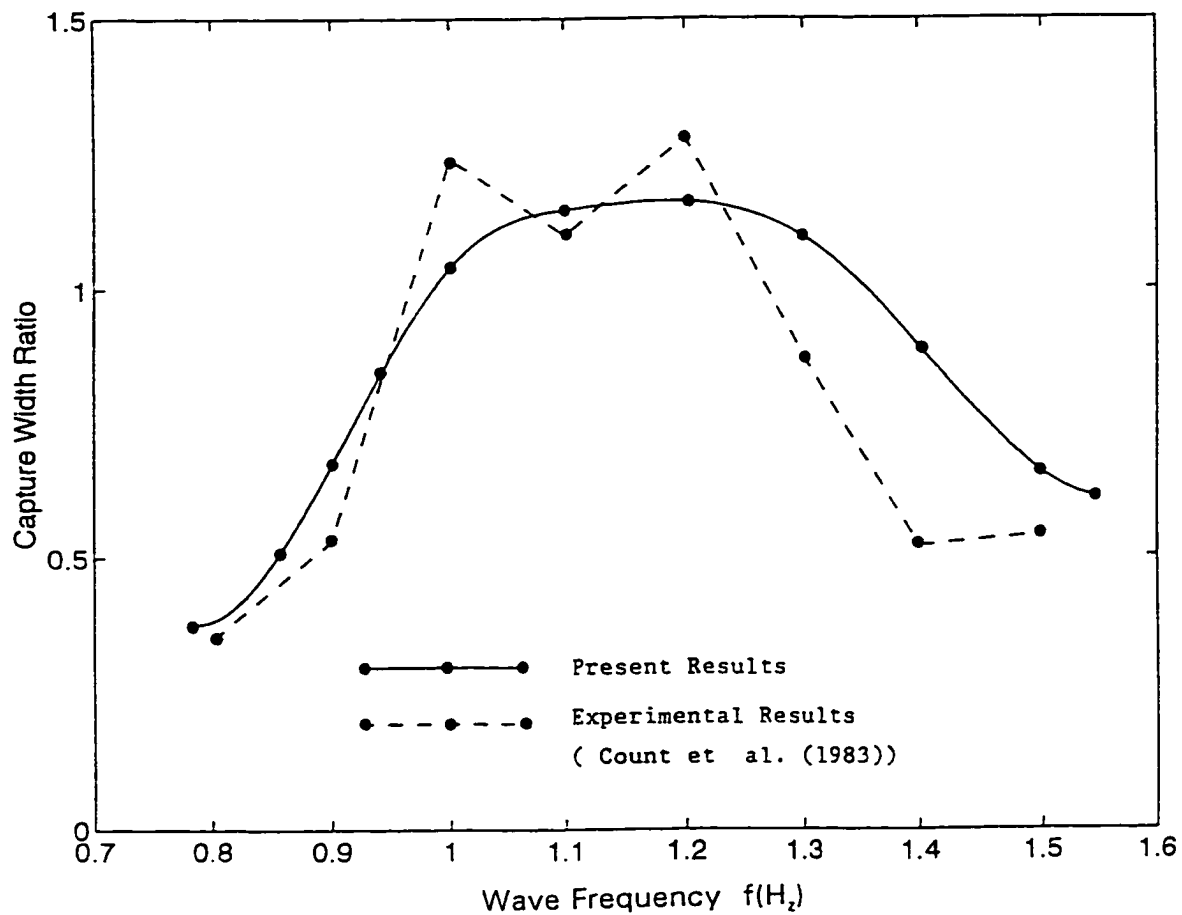
Figure 5.19. Comparison of Predicted OWC Device Performance
with the Experimental Data of Count et al. (1983)
($\theta_w=0°$, regular waves)

waves in a wide wave tank. In a very narrow wave tank, regular waves effectively transmit energy in the direction of wave propagation with negligible energy transmitted to the side walls. Therefore, waves remain fairly consistent in height at any particular location in the narrow tank (assuming no interference effects from a structure, change in tank bottom slope or depth). However, in a wide wave tank, where the crest and trough extends the width of the tank, distortions in the wave profile are common and can cause variations in wave height at any particular location in the tank. Count et al. (1983) reported these inherent distortions of regular waves in the wide tank at Gifford Technology and estimated that variations in wave height up to 20% are possible. Because the experimental wave heights generated in the wide tank were computer controlled and not measured in front of the device, any variation in wave height will effect the incident average wave power and produce errors in the experimental capture width ratio.

CHAPTER 6

PERFORMANCE OF THE OSCILLATING WATER COLUMN DEVICE

IN RANDOM SEAS

Determining the performance of the oscillating water column wave energy device in random seas is an important step towards the understanding of the potential wave power extraction in a realistic sea state. A probabilistic model to describe the response of the oscillating water column in a random sea state is developed in this chapter. The mathematical model utilizes the radiation-diffraction finite element results determined by potential flow theory in Chapter 5 and a transformation of random variables from a representative wave height and period probability distribution. The probabilistic approach models the device performance for a complete range of wave spectral bandwidths. In addition, the average capture width ratio is determined for random seas and verified with experimental results carried out by Count et al. (1983) in a wide wave tank.

6.1   Formulation of the Probabilistic Model

The average capture width ratio in random sea conditions is determined by a transform-ation of random variables from Longuet-Higgins (1983) joint probability distribution of normalized wave height and period (pdf(R,τ)) and the functional relationship (derived by linear wave theory for monochromatic sea conditions) of available average wave power in finite depth and the average wave power extraction for the particular type of OWC device. A flowchart

depicting the methodology used for carrying out the transformations for random sea conditions is given in Figure 6.1. The mathematical formulation is separated into two main components, namely: (1) the determination of average wave power extraction $(\overline{P}_{e_N})$ for a particular OWC device type in random seas, and (2) the determination of available average wave power $(\overline{P}_N)$ in finite depth in random seas. The ratio of these two components is equivalent to the average capture width ratio $(\overline{CWR} = \overline{P}_{e_N}/\overline{P}_N)$. Because the OWC devices considered in Chapter 5 have been numerically modelled in finite water depth (i.e. waves are affected by the presence of the sea bottom), it is necessary to extend the probabilistic models of average wave power given in Chapter 3 to include for the effects of water depth.

6.1.1 Average OWC Power Extraction in Random Seas

The average wave power extracted by the OWC device for monochromatic sea conditions has been derived in Chapter 4 (Equation 4.14) and is given by

$$P_e = \frac{1}{2}B_a\omega^2\alpha_o^2\left(\frac{\xi_o}{\alpha_o}\right)^2 \tag{6.1}$$

where, B_a, ω, α_o, and ξ_o are the dimensional applied damping, wave frequency, wave amplitude and internal amplitude response as a function of wave direction, respectively. Expressing Equation 6.1 in terms of the normalized wave height $(R = H/H_{rms} = 2\alpha_o/H_{rms})$, normalized wave period $(\tau = T/T_{m_{01}})$ and non-dimensional applied damping $\left(b_a = B_a/\rho a^3\sqrt{g/a}\right)$ gives

$$P_e = \left(\frac{2\pi}{\overline{W}_T}\right)^3 b_a\frac{R^2}{\tau^2}\left(\frac{\xi_o}{\alpha_o}\right)^2\left(\frac{\rho g^2}{32\pi}H^2_{rms}T_{m_{01}}(2a)\right) \tag{6.2}$$

Random Sea Conditions
Joint PDF of Wave Height
and Period pdf(R,r)

Wave Power Extraction
from OWC Device

Available Wave Power
in Finite Depth

Functional Relationship

$$P_{e_N} = f_1(R,\tau)$$

Functional Relationship

$$P_N = f_2(R,\tau)$$

Joint PDF of Wave Power
Extraction and Period

$$pdf(P_{e_N},\tau)$$

Joint PDF of Wave Power
and Period

$$pdf(P_N,\tau)$$

PDF of Wave Power
Extraction

$$pdf(P_{e_n}) = \int_0^\infty pdf(P_{e_N},\tau)d\tau$$

PDF of Wave Power in
Finite Depth

$$pdf(P_N) = \int_0^\infty pdf(P_N,\tau)d\tau$$

Average Wave Power
Extraction

$$\overline{P}_{e_N} = \int_0^\infty P_{e_N} \cdot pdf(P_{e_N})dP_{e_N}$$

Average Wave Power
in Finite Depth

$$\overline{P}_N = \int_0^\infty P_N \cdot pdf(P_N)dP_N$$

Average Capture
Width Ratio

$$\overline{CWR} = \overline{P}_{e_N}/\overline{P}_N$$

Figure 6.1. Methodology for the Determination of
Average Capture Width Ratio in Random Seas

where $\overline{W}_T$ = Mean Normalized Wave Period = $T_{m_{01}}/\sqrt{a/g}$. The expression $\dfrac{\rho g^2}{32\pi}H^2_{rms}T_{m_{01}}$ (2a) is equivalent to the deep water average wave power for a device width of 2a. The normalized wave power extraction (P_{e_N}) is given by

$$P_{e_N} = \frac{P_e}{\dfrac{\rho g^2}{32\pi}H^2_{rms}T_{m_{01}}(2a)} = \left(\frac{2\pi}{\overline{W}_T}\right)^3 b_a \frac{R^2}{\tau^2}\left(\frac{\xi_0}{\alpha_0}\right)^2 \tag{6.3}$$

where the OWC amplitude response ξ_0/α_0 can be expressed as

$$\left(\frac{\xi_0}{\alpha_0}\right)^2 = \frac{C_z^2}{\left(l_x l_y - \dfrac{4\pi^2}{W_t^2}\mu\right)^2 + \left(\dfrac{2\pi}{W_T}(b_a+b_r)\right)^2}$$

$$= \frac{C_z^2}{\left(l_x l_y - \dfrac{4\pi^2\mu}{\tau^2\overline{W}_T^2}\right)^2 + \left(\dfrac{2\pi}{\tau\overline{W}_T}(b_a+b_r)\right)^2} \tag{6.4}$$

By substituting equation 6.4 into 6.3, the normalized average waver power extraction becomes

$$P_{e_N} = \left(\frac{2\pi}{\overline{W}_T}\right)^3 b_a \frac{R^2}{\tau^2}\left[\frac{C_z^2}{\left(l_x l_y - \dfrac{4\pi^2\mu}{\tau^2\overline{W}_T^2}\right)^2 + \left(\dfrac{2\pi}{\tau\overline{W}_T}(b_a+b_r)\right)^2}\right] = f_1(R,\tau) \tag{6.5}$$

This expression is referred to as the functional relationship between normalized wave power extraction (P_{e_N}) and the random variables of normalized wave height (R) and period (τ). Rearranging equation 6.5, such that

$$R^2 = \alpha(\tau)\tau^2 P_{e_N} \tag{6.6}$$

and

$$R = \alpha^{1/2}(\tau)\tau P_{e_N}^{1/2} = h_1(P_{e_N},\tau)$$

where

$$\alpha(\tau) = \left(\frac{\overline{W}_T}{2\pi}\right)^3 \frac{1}{b_a} \left[\frac{\left(l_x l_y - \frac{4\pi^2\mu}{\tau^2 \overline{W}_T^2}\right)^2 + \left(\frac{2\pi}{\tau\overline{W}_T}(b_a+b_r)\right)^2}{C_z^2} \right]$$

and by applying a standard transformation of random variables, Longuet-Higgins (1983) joint probability-distribution of normalized wave height and period (pdf (R,τ)) is transformed to the pdf (P_{e_N},τ) by the relationship

$$pdf(P_{e_N},\tau) = [pdf(R,\tau)]_{R = h_1(P_{e_N},\tau)} \cdot |J|$$

$$= [pdf(R,\tau)]_{R = h_1(P_{e_N},\tau)} \cdot |\partial R/\partial P_{e_N}|$$

$$= \left[C_1 \frac{R^2}{\tau^2}\exp\left\{-R^2\left(1+\frac{1}{\nu^2}(1-\frac{1}{\tau})^2\right)\right\}\right]_{R=\alpha^{1/2}(\tau)\tau P_{e_N}^{1/2}} \cdot \frac{1}{2}\alpha^{1/2}(\tau)\tau P_{e_N}^{-1/2}$$

(6.7)

where ν is the spectral bandwidth parameter. The joint pdf (P_{e_N},τ) now becomes

$$pdf(P_{e_N},\tau) = \frac{1}{2}C_1\alpha^{3/2}(\tau)\,\tau\,P_{e_N}^{1/2}\exp\left\{-\alpha(\tau)\tau^2 P_{e_N}\left(1+\frac{1}{\nu^2}\left(1-\frac{1}{\tau}\right)^2\right)\right\}$$

(6.8)

The pdf(P_{e_N}) is determined by integrating the pdf(P_{e_N},τ) according to

$$\text{pdf}(P_{e_N}) = \int_o^\infty \text{pdf}(P_{e_N}, \tau) d\tau$$

and the average normalized wave power extraction $(\overline{P}_{e_N})$ is determined by the expression

$$\overline{P}_{e_N} = \frac{\int_o^\infty P_{e_N} \cdot \text{pdf}(P_{e_N}) dP_{e_N}}{\int_o^\infty \text{pdf}(P_{e_N}) dP_{e_N}} = \frac{\int_o^\infty \int_o^\infty P_{e_N} \cdot \text{pdf}(P_{e_N}, \tau) d\tau P_{e_N}}{\int_o^\infty \int_o^\infty \text{pdf}(P_{e_N}, \tau) d\tau P_{e_N}} \tag{6.10}$$

where $\int_o^\infty \int_o^\infty (P_{e_N}, \tau) d\tau dP_{e_N} = 1.0$ by definition of a joint probability density function.

Therefore, $\overline{P}_{e_N}$ reduces to

$$\overline{P}_{e_N} = \int_o^\infty \int_o^\infty P_{e_N} \text{pdf}(P_{e_N}, \tau) d\tau dP_{e_N} \tag{6.11}$$

and substituting Equation 6.8 into 6.11 gives

$$\overline{P}_{e_N} = \int_o^\infty \int_o^\infty \frac{1}{2} C_1 \alpha^{3/2}(\tau) \tau P_{e_N}^{3/2} \exp\left\{-\alpha(\tau)\tau^2 P_{e_N}\left(1 + \frac{1}{v^2}\left(1 - \frac{1}{\tau}\right)^2\right)\right\} d\tau dP_{e_N} \tag{6.12}$$

6.1.2 Average Wave Power in Finite Depth and Random Seas

The linear wave approximation for average wave power in finite depth and monochromatic seas has been previously derived in Section 2.2 of Chapter 2 and is given by

$$P = \frac{\rho g^2}{32\pi} H^2 T \left[1 + \frac{2kh}{\sinh 2kh} \right] \tanh kh \qquad (6.13)$$

Probabilistic methods for the determination of average wave power in deep water and random sea conditions were derived in Chapter 3, by using a standard transformation of random variables from Longuet-Higgins (1952, 1983) probability distributions and the deep water relationship $P = \frac{\rho g^2}{32\pi} H^2 T$. In this section, a similar probabilistic formulation is derived to include for the effect of finite water depth (i.e. the additional term $\left[1 + \frac{2kh}{\sin 2kh} \right] \tanh kh$ in Equation 6.13). Normalizing Equation 6.13 by the root-mean square wave height and mean period gives

$$P = \frac{\rho g^2}{32\pi} R^2 H_{rms}^2 \tau T_{m_{01}} g(\tau) \qquad (6.14)$$

where

$$g(\tau) = \left[1 + \frac{2kh(\tau)}{\sinh 2kh(\tau)} \right] \tanh kh(\tau) \qquad (6.15)$$

and the normalized average wave power in finite depth P_N can be expressed by

$$P_N = \frac{P}{\dfrac{\rho g^2}{32\pi} H_{rms}^2 T_{m_{01}}} = R^2 \tau g(\tau) = f_2(R, \tau) \qquad (6.16)$$

The function kh in Equation 6.13 is related directly to the dispersion relationship, such that

$$k_o h = kh \tanh kh \qquad (6.17)$$

where $k_o h = \frac{2\pi}{L_o} h = \frac{4\pi^2}{gT^2} h$ and $kh = \frac{2\pi}{L} h$. Because the dispersion relationship is a transcendental equation, the wave length (L) must be determined iteratively for a given wave period and water depth. An approximate solution for kh, given by Hunt (1979), is

$$(kh)^2 = y^2 + \cfrac{y}{1 + \displaystyle\sum_{n=1}^{6} d_n y^n}$$
(6.18)

where $\quad y \;=\; \left(\dfrac{2\pi}{T}\right)^2 \dfrac{h}{g}$

$d_1 \;=\; 0.6666666666, \qquad d_2 \;=\; 0.355555555, \qquad d_3 \;=\; 0.1608465608$

$d_4 \;=\; 0.0632098765, \qquad d_5 \;=\; 0.0217540484, \qquad d_6 \;=\; 0.0065407983$

Expressing the function y in terms of the normalized wave period $(\tau = T/T_{m_{01}})$ and the characteristic water depth $(h = l_z a)$ gives

$$y(\tau) \;=\; \frac{4\pi^2}{\tau^2 T^2_{m_{01}}} \frac{l_z a}{g} = \frac{4\pi^2 l_z}{\tau^2 \overline{W}^2_T}$$
(6.19)

and the function $kh(\tau)$ becomes

(6.20) $\quad (kh(\tau))^2 \;=\; y^2(\tau) \;=\; \cfrac{y(\tau)}{1 + \displaystyle\sum_{n=1}^{6} d_n y^n(\tau)}$

Rearranging Equation 6.16 such that the functional relationship between normalized wave height, wave period, and average wave power becomes

$$R = \left(\frac{1}{\tau g(\tau)}\right)^{1/2} P_N^{1/2} \;=\; h_2(P_N, \tau)$$
(6.21)

and the pdf(R, τ) is transformed to the pdf (P_N, τ) by the relationship

$$\text{pdf}(P_N, \tau) = (\text{pdf}(R, \tau))_{R = h_2(P_N, \tau)} \cdot |J|$$

$$= C_1 \frac{R^2}{\tau^2} \exp\left\{-R^2\left(1 + \frac{1}{v^2}(1 - \frac{1}{\tau})^2\right)\right\}_{R = h_2(P_N, \tau)} \cdot |\partial R/\partial P_N|$$

$$= C_1 \frac{P_N}{\tau^3 g(\tau)} \exp\left\{-\frac{P_N}{\tau g(\tau)}\left(1 + \frac{1}{v^2}(1 - \frac{1}{\tau})^2\right)\right\} \cdot \frac{1}{2}\left(\frac{1}{\tau g(\tau)}\right)^{1/2} P_N^{-1/2}$$

$$= \frac{1}{2}C_1\left(\frac{P_N}{\tau^7 g^3(\tau)}\right)^{1/2} \cdot \exp\left\{-\frac{P_N}{\tau g(\tau)}\left(1 + \frac{1}{v^2}(1 - \frac{1}{\tau})^2\right)\right\}$$

(6.22)

The pdf(P_N) is determined by integrating out the normalized wave period by

$$\text{pdf}(P_N) = \int_o^\infty \text{pdf}(P_N, \tau) d\tau \qquad (6.23)$$

and the average wave power ($\overline{P}_N$) for finite depth and random seas becomes

$$\overline{P}_N = \frac{\int_o^\infty P_N \cdot \text{pdf}(P_N) dP_N}{\int_o^\infty \text{pdf}(P_N) dP_N} = \frac{\int_o^\infty \int_o^\infty P_N \cdot \text{pdf}(P_N, \tau) d\tau P_N}{\int_o^\infty \int_o^\infty \text{pdf}(P_N, \tau) d\tau P_N} \qquad (6.24)$$

By definition of a probability distribution the

$$\int_o^\infty \int_o^\infty \text{pdf}(P_N, \tau) d\tau dP_N = 1.0$$

and $\overline{P}_N$ becomes

$$\overline{P}_N = \int_0^\infty \int_0^\infty P_N \cdot pdf(P_N,\tau) d\tau dP_N$$

$$= \int_0^\infty \int_0^\infty \frac{1}{2} C_1 \left(\frac{P_N^3}{\tau^7 g^3(\tau)} \right)^{1/2} \exp\left\{ -\frac{P_N}{\tau g(\tau)} \left(1 + \frac{1}{v^2} \left(1 - \frac{1}{\tau} \right)^2 \right) \right\} d\tau dP_N \qquad (6.25)$$

6.1.3 Average Capture Width Ratio in Random Seas

The average capture width ratio ($\overline{CWR}$) in a random sea state is defined as the ratio of average wave power extraction ($\overline{P}_{e_N}$) for an OWC device of width 2a and the available average wave power ($\overline{P}_N$).

$$\overline{CWR} = \frac{\overline{P}_{e_N}}{\overline{P}_N} = \frac{\dfrac{\overline{P}_e}{\dfrac{\rho g^2}{32\pi} H_{rms}^2 T_{m_{01}}(2a)}}{\dfrac{\overline{P}}{\dfrac{\rho g^2}{32\pi} H_{rms}^2 T_{m_{01}}}} = \frac{\overline{P}_e}{\overline{P}(2a)} \qquad (6.26)$$

where $\overline{P}_e$ and $\overline{P}$ represent the dimensional average wave power extraction and average wave power, respectively. Substituting Equations 6.12 and 6.26 into the above expression gives

$$\overline{CWR} = \frac{\int_0^\infty \int_0^\infty P_{e_N} \cdot pdf(P_{e_N},\tau) d\tau dP_{e_N}}{\int_0^\infty \int_0^\infty P_N \cdot pdf(P_N,\tau) d\tau dP_N}$$

$$= \frac{\int_0^\infty \int_0^\infty \alpha^{3/2}(\tau) \tau P_{e_N}^{3/2} \cdot \exp\left\{ -\alpha(\tau) \tau^2 P_{e_N} \left(1 + \frac{1}{v^2}(1 - \frac{1}{\tau})^2 \right) \right\} d\tau dP_{e_N}}{\int_0^\infty \int_0^\infty \left(\frac{P_N^3}{\tau^7 g^3(\tau)} \right)^{1/2} \cdot \exp\left\{ -\frac{P_N}{\tau g(\tau)} \left(1 + \frac{1}{v^2}\left(1 - \frac{1}{\tau} \right)^2 \right) \right\} d\tau dP_N} \qquad (6.28)$$

The average capture width ratio is determined numerically for a particular OWC device type and random sea condition. Because the frequency dependent coefficients μ, b_r, and C_z represent a family of curves for a given device type, a piecewise integration is performed with the coefficients approximated by a number of linear segments over the range of numerical integration. The segments are represented by the linear equations given by

$$(\mu)_n = A_n + B_n(\tau\overline{W}_T), \quad (b_r)_n = C_n + D_n(\tau\overline{W}_T) \quad \text{and} \quad (C_z)_n = E_n + F_n(\tau\overline{W}_T) \quad (6.27)$$

where n represents the number of linear segments and A_n, B_n, C_n, D_n, E_n,and F_n are constants that are dependent on the OWC device type and range of $\tau\overline{W}_T$. Based on the dispersion relationship (expressed in terms of the normalized parameters) $\tau\overline{W}_T = W_T = \dfrac{2\pi}{\sqrt{ka\tanh kl_z a}}$, the curves of μ, b_r, C_z given in Chapter 5, can be converted to the format necessary for the linear segment approximation and the determination of $\overline{CWR}$. For $\nu = 0$ (constant wave period), equation 6.28 contains a singularity which can be removed by the substitution $x = (1-1/\tau)/\nu$. Based on this substitution the $\overline{CWR}$ can be integrated analytically (Appendix D) and reduces to the capture width ratio in monochromatic seas (equation 5.6 for $\alpha_1 = l_x l_y$ and $\alpha_2 = 2.0$) with $T = T_{m_{01}}$.

6.2   OWC Response to Random Seas

OWC device types 5 and 6 were chosen as examples for determining the response of each device to various random sea conditions. Both devices show relatively high capture width ratios in response to monochromatic seas over a relatively wide range of wave frequencies and directions. As described in Section 6.1, the average capture width ratio $\overline{CWR}$ is determined numerically for a particular OWC device type and random sea condition. The random sea condition are described by two variables; the spectral bandwidth parameter υ and the normalized

average wave period $\overline{W}_T = T_{m_{01}}/\sqrt{a/g}$. OWC response curves based on these two variables are described in Sections 6.2.1 and 6.2.2 for device types 5 and 6, respectively.

6.2.1 Device Type 5 - Random Seas

Figure 6.2 presents the response curves of device type 5 $(l_x=l_y=l_z=2.0)$ for varying random wave conditions approaching at an angle of $\theta_w=0°$. The curves represent the average capture width ratio (Equation 6.28) of the device in random seas with four different spectral bandwidth parameters (ν) equal to 0.0, 0.2, 0.4 and 0.6 and normalized mean wave periods $(\overline{W}_T)$ between the range of 3 to 15. The curves of μ, b_r, and C_z used for the linear segment approximation were obtained from Figure C.7 in Appendix C.

There are a number of points that should be noted from the response curves given in Figure 6.2. The results, clearly demonstrate the following:

A- A reduction in peak power output occurs as the spectral bandwidth (υ) increases (i.e. broad-banded wave spectra causes a degradation in performance near the natural frequency of the device). In particular, a 45% reduction in peak power output occurs for wide banded wave spectra $(\nu=0.6)$ when compared to monochromatic wave conditions $(\nu=0.0)$.

B- Random seas have the effect of broadening the frequency response of the device and improving the performance for normalized mean wave periods greater than 11 and less than 6. In this range, the average capture width ratio increases for larger spectral bandwidth parameters (i.e. broad banded wave spectra $\nu=0.6$
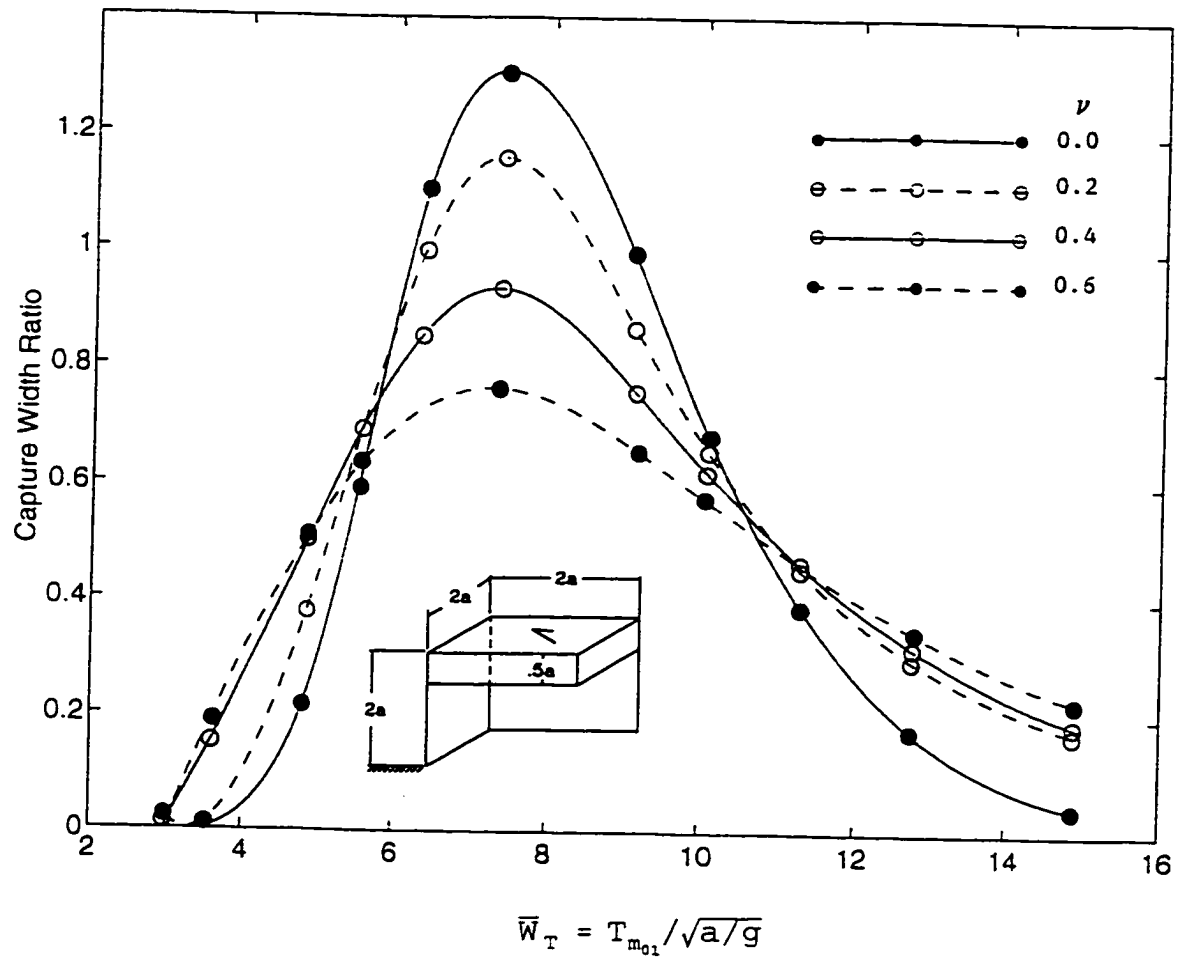
Figure 6.2. Average Capture Width Ratio in Random Seas - Device Type 5
$(\theta_w = 0°, \ l_x = l_y = l_z = 2.0)$

has the effect of increasing $\overline{\text{CWR}}$ by approximately 20% when compared to monochromatic seas).

Because the curves presented in Figure 6.2 represent random waves approaching from an incident wave direction of $\theta_w = 0°$, a further reduction in device performance would be expected from other wave directions. It is estimated that the maximum $\overline{\text{CWR}}$ for random seas approaching from the directions of 45° and 90° and a spectral bandwidth parameter of $\nu = 0.6$ are approximately 0.45 and 0.17, respectively.

6.2.2   Device Type 6 - Random Seas

The performance of device type 6 ($l_x = 1.0$, $l_y = l_z = 2.0$) in random waves approaching at an angle of $\theta_w = 0°$ is presented in Figure 6.3. In this example, μ, b_r and C_z curves used for the linear segment approximation and numerical integration were obtained from Figure C.8 in Appendix C.

The curves in Figure 6.3 demonstrate the advantage of designing an oscillating water column device with a broad frequency response. Although a reduction in power output for increased spectral bandwidth parameters is evident near the two resonances, the broad frequency response is still maintained. For $\nu = 0.6$, the average $\overline{\text{CWR}}$ is approximately 0.8 for normalized mean wave periods in the range of 6 to 10. In addition to the broad frequency response near the two resonances of the device, the curves also show increased performance over the monochromatic seas case for $\overline{W}_T > 12.5$ and $\overline{W}_T < 5.5$. Similar characteristics were also apparent in the previous example, however, in this example the $\overline{\text{CWR}}$ is considerably improved, particularly for higher wave periods with potentially higher power levels.
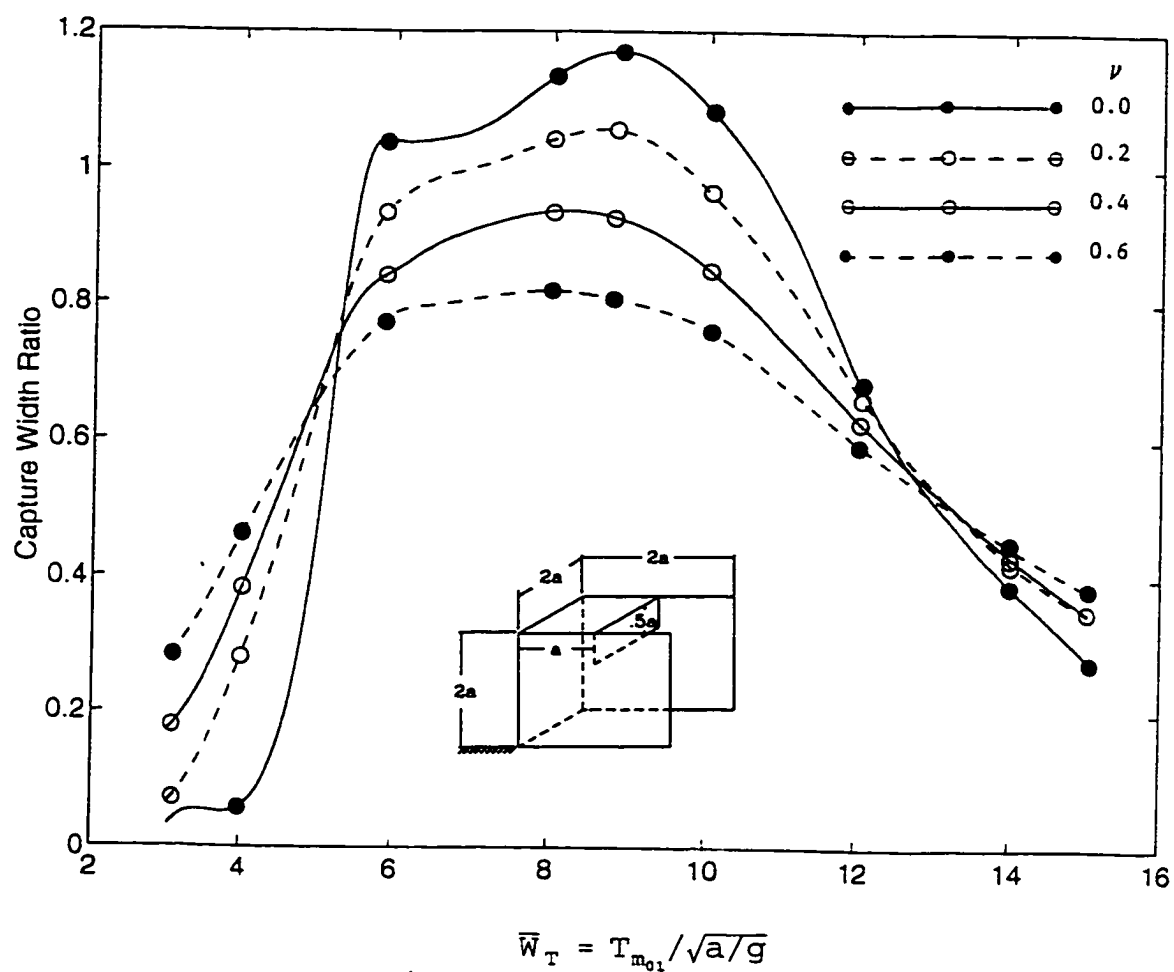
Figure 6.3. Average Capture Width Ratio in Random Seas - Device Type 6
$(\theta_w=0°,\ l_x=l_y=l_z = 2.0)$

6.3   Verification of Model to Experimental Results

Although many laboratory experiments of the oscillating water column have been

conducted and results reported in the literature, most of these studies involved monochromatic

waves in a narrow wave tank. These data sets are useful for assessing the two dimensional

effects associated with the OWC device but gives very little insight into the 3-dimensional

radiation/diffraction effects of an isolated device in random seas. For this reason, the search was

limited to experimental results in a wide wave tank capable of generating random waves. One

such experiment was carried out by Count et al. (1983) which examined the performance of both

an isolated device and arrays in regular and irregular seas. In this section, the experimental tests

of the isolated device to random waves are compared to the probabilistic model developed in this

chapter.

The experimental tests for regular waves have been described and verified with numerical

results given in Section 5.10.2. The geometrical configuration of the oscillating water column

used in the irregular wave tests is the same as the one used in regular tests. The spectral form

selected for the irregular wave tests was a Pierson-Moskowitz (1964) frequency spectrum with

a Mitsuyasu spread. The probabilistic methods developed up to this point represent random wave

conditions in which all the energy is confined to a single direction. Although wave spectra can

have a significant portion of energy in a very narrow directional band, it is more typical for

random seas to have a wide range of directionality. To include for the effect of directionality in

the probabilistic model, the joint probability distribution of wave height and period was assumed

to represent the irregular wave conditions in a particular directional band. The average capture

width ratio determined numerically in each directional band was then weighted according to the

percentage of energy in each band and summed to determine the overall device performance and average capture width ratio.

All the irregular wave tests carried out in the wide wave tank had a directional spectral $S(f,\theta)$ of the form

$$S(f,\theta) = S(f)\cos^s\theta/\int_o^\pi \cos^s\theta\, d\theta \qquad (6.28)$$

where the parameter s is a spreading index of the form

$$s = 15.85\left(\frac{f}{f_o}\right)^5 \quad, f \le f_o$$

$$\qquad (6.29)$$

$$s = 15.85\left(\frac{f_o}{f}\right)^5 \quad, f \ge f_o$$

and f_o is the wave frequency at which the frequency spectra $S(f)$ is maximum. The Pierson-Moskowitz (1964) frequency spectra $S(f)$ is of the form

$$S(f) = Af^{-5}\exp(-Bf^{-4}) \qquad (6.32)$$

where the constants A and B are

$$A = \frac{2.7m_o}{T_e^4} \quad\text{and}\quad B = \frac{0.675}{T_e^4} \qquad (6.33)$$

and m_o is the area under the frequency spectra and T_e is the energy period defined as

$$T_e = \frac{m_{-1}}{m_o} = \frac{\int_0^\infty f^{-1}S(f)df}{\int_0^\infty S(f)df} \qquad (6.34)$$

The experimental results from the irregular wave tests are plotted in terms of the average capture width ratio (defined in Section 5.10) and the energy period T_e. In order to verify the probabilistic model developed in this chapter with the experimental results, it is necessary to determine the spectral bandwidth parameter, ν, of the Pierson-Moscowitz spectra and the relationship between the energy period T_e and mean period $T_{m_{01}}$. By definition of moments, m_n is defined as

$$m_n = \int_0^\infty f^n S(f)df = \int_0^\infty f^n A f^{-5} \exp(-Bf^{-4})df = \int_0^\infty A f^{n-5} \exp(-Bf^{-4})df \qquad (6.35)$$

by letting $t = Bf^{-4}$ and $dt = -4Bf^{-5}df$, the above expression can be rewritten in the form

$$m_n = \int_0^\infty \frac{A}{4B}\left(\frac{B}{t}\right)^{\frac{n}{4}} \exp(-t) \ dt = \frac{A}{4B^{1-\frac{n}{4}}} \int_0^\infty t^{-\frac{n}{4}} \exp(-t)dt \qquad (6.36)$$

By a further substitution of $-n/4 = m-1$, equation 6.36 can be expressed in terms of the gamma function (Sarpkaya and Isaacson, 1981) given by

$$m_n = \frac{1}{4} A B^{\frac{n}{4}-1} \ \Gamma\left(1-\frac{n}{4}\right) \quad \text{for } n \le 4 \qquad (6.37)$$

Based on this expression, relationships between the experimental statistical parameters (T_e, T_p) and the theoretical statistical parameters $(\nu, T_{m_{01}})$ were derived and are given in Table 6.1.

Table 6.1

Statistical Relationships for the Pierson Moscowitz Spectra

Moments (m_n)	$m_o = \dfrac{A}{4B}$ $\qquad m_1 = 0.30635\dfrac{A}{B^{3/4}}$ $m_2 = 0.44311\dfrac{A}{\sqrt{B}}$ $\quad m_{-1} = 0.2266AB^{-5/4}$
Spectral Bandwidth Parameter (ν)	$\nu = \left(\dfrac{m_o m_2}{m_1^2} - 1\right)^{1/2} = 0.4247$
Energy Period and Mean Period Ratio $\dfrac{T_e}{T_{m_{01}}}$	$T_e = \dfrac{m_{-1}}{m_o} \quad T_{m_{01}} = \dfrac{m_o}{m_1} \quad \dfrac{T_e}{T_{m_{01}}} = 1.1107$
Energy Period and Peak Period Ratio $\dfrac{T_e}{T_p}$	$T_e = \dfrac{m_{-1}}{m_o} \quad , \quad f_o = \dfrac{1}{T_p}$ $\dfrac{T_e}{T_p} = 0.8573$

The peak frequency $(f_o = \dfrac{1}{T_p})$ was determined by

$$\frac{\partial}{\partial f}S(f) = \frac{\partial}{\partial f}Af^{-5}\exp(-Bf^{-4}) = 0 \qquad (6.38)$$

which after differentiation gives $f_o = 0.9457B^{1/4}$.

Based on this information, the probabilistic model was tested with the experimental results by first generating a family of curves which represent the performance of the device in random waves ($\nu = 0.4247$) approaching from five directions over the range of energy periods (T_e) used in the experimental wave tests. Figure 6.4 depicts the average capture width ratio of the isolated

device for wave directions equal to $\theta_w = 0°$, 22.5°, 45°, 67.5°, and 90°. To account for the directional spread of the wave spectra used in the experimental tests, the energy was proportioned into quadrants in the range between -90° to +90°. Due to the symmetry of the device and recognizing an equal distribution of energy on either side of the principal wave direction ($\theta_w = 0°$), it is only necessary to consider the response curves and directional spectra in the range between 0 and +90°. Five quadrants in the range of 0° to 11.25°, 11.25° to 33.75°, 33.75° to 56.25°, 56.25° to 78.75°, and 78.75° to 90° were chosen to represent the fractional energy of the directional spectra. The fraction of energy in a quadrant between θ_1 to θ_2 is given by

$$\frac{\int_o^\infty \int_{\theta_1}^{\theta_2} S(f,\theta) \, d\theta \, df}{\int_o^\infty \int_{-\pi/2}^{\pi/2} S(f,\theta) \, d\theta \, df} = \text{Fractional Energy in Quadrant } \theta_1 \text{ to } \theta_2 \qquad (6.39)$$

The overall device performance for a particular energy period (T_e) was approximated by multiplying the fraction of energy in each quadrant by the representative $\overline{CWR}$ (given in Figure 6.4) and summed over the 9 quadrants. Results of this methodology in comparison to the experimental data of Count et al. (1983) are displayed in Figure 6.5.

Although the probabilistic model slightly over predicts the experimental results, the predicted curve shows good qualitative agreement and follows the trend of data in all the experimental energy periods. The differences between the predicted and experimental results may be attributed to viscous energy losses and the interaction of the various wave components in the irregular sea state which have not been accounted for in the theoretical model. Applying a weighting function (proportional to the fraction of directional energy) to the average capture width ratio for random waves from individual directions appears to be a satisfactory method for
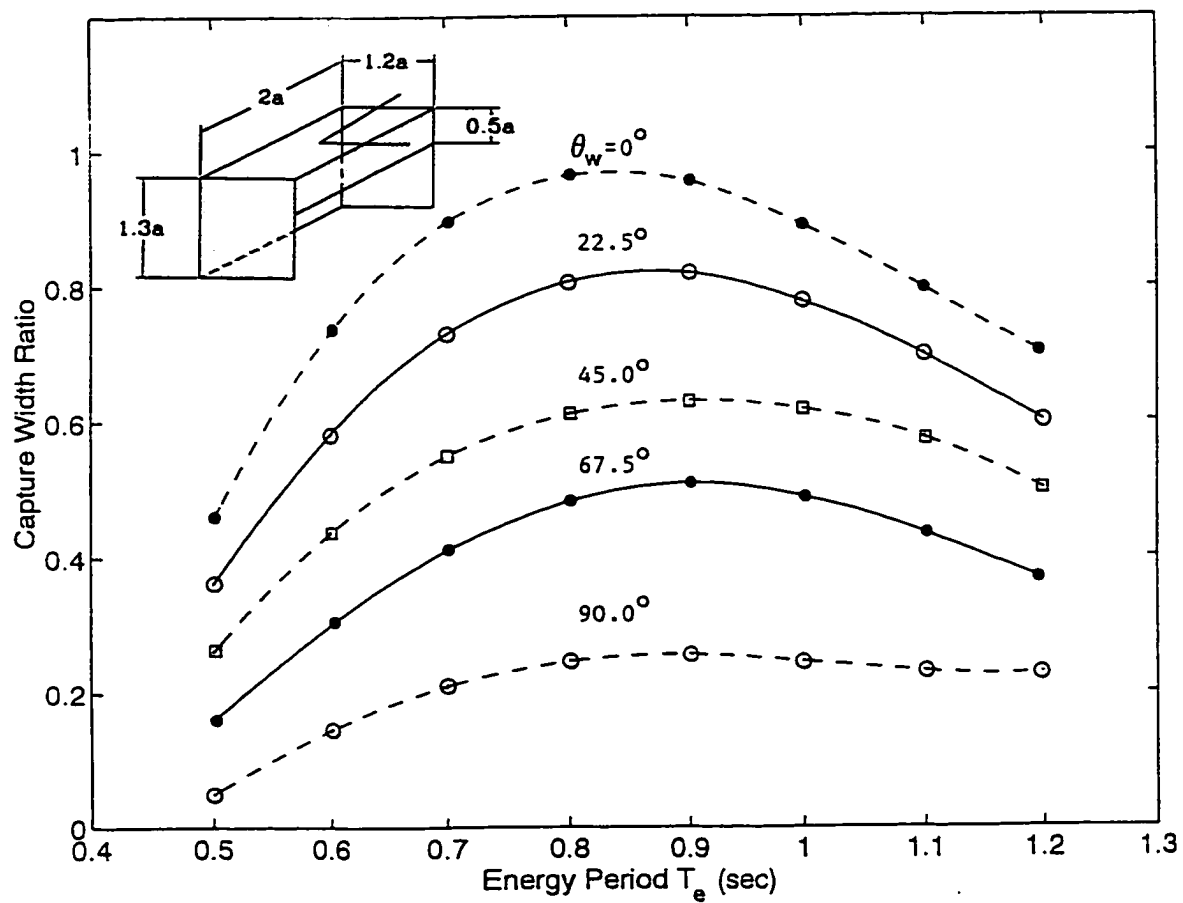
Figure 6.4. Average Capture Width Ratio of Isolated Device
for Single Wave Directions
($\nu=0.4247$, $l_x=1.2$, $l_y=2.0$, $l_z=1.3$)
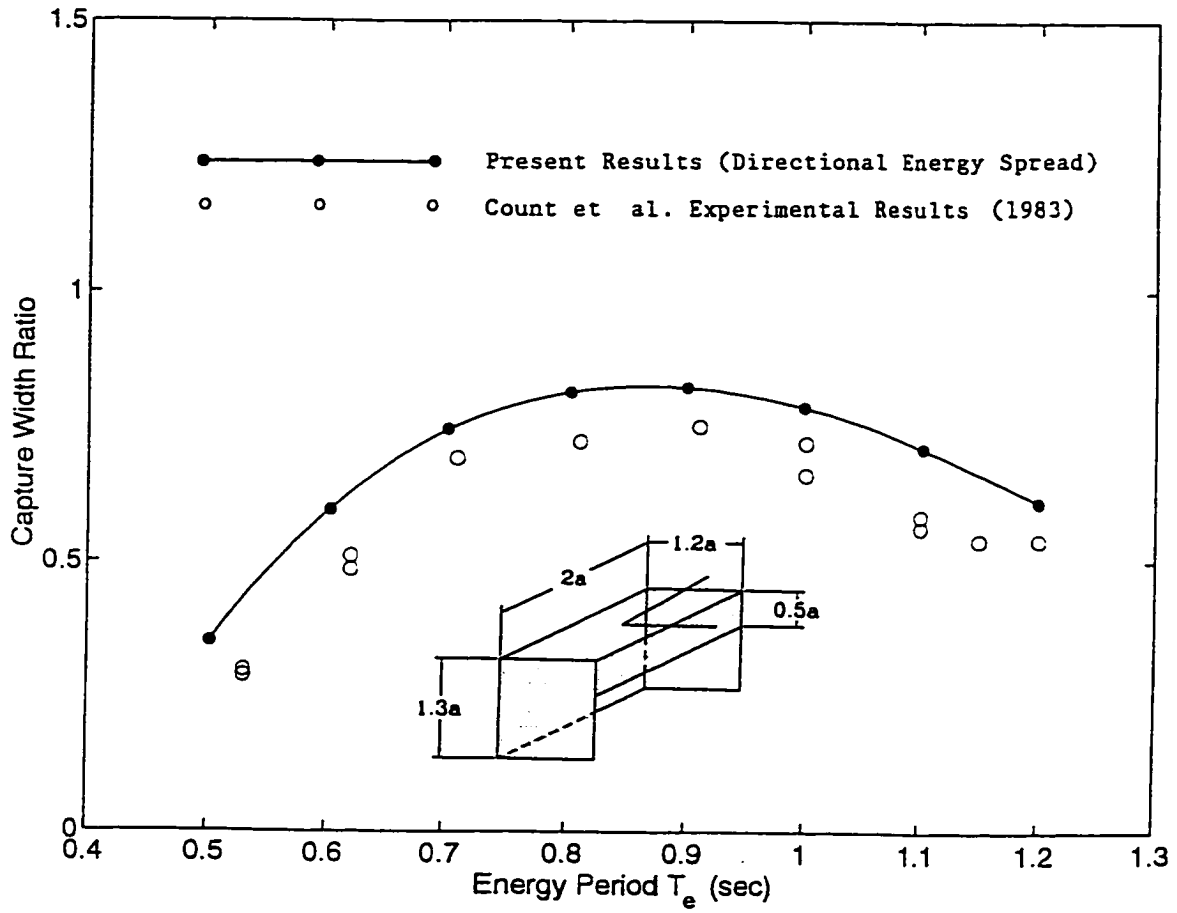
Figure 6.5. Comparison of Predicted Overall Device Performance
to Experimental Data of Count et al. (1983).

including directionality effects. However, this method can be improved on by increasing the number of quadrants in which the weighting function can be applied and this would require additional finite element diffraction computations.

It is interesting to compare the predicted overall performance of the device in Figure 6.5 with the average capture width ratio curves for individual wave directions in Figure 6.4. Although Figure 6.4 shows a significant reduction in $\overline{CWR}$ for wave directions greater than 45°, the overall device performance (Figure 6.5) still remains relatively high. This is because a significant portion of energy, approximately 85% of the total energy in the directional spectra, is contained within ±35° of the principle wave direction (0°). Therefore, the weighting function applied to the quadrants outside of ±35° is relatively small and has less of an effect on the overall device performance. However, directional wave spectra with a large degree of spreading (i.e. small spreading index parameters) will contribute to a further reduction in the overall device performance.

CHAPTER 7

CONCLUSIONS AND RECOMMENDATIONS

The objective of this research was to quantitatively describe the response of various three-dimensional OWC wave energy devices in monochromatic and random sea conditions. The mathematical problem was formulated through the development of a probability density function of wave power extraction which was transformed from a theoretical joint distribution of wave heights and periods in a random wave field and a functional relationship describing the wave power extraction of the device in monochromatic sea conditions. Three-dimensional numerical modelling by the hybrid finite element method was used to describe the complicated fluid/structure interaction and the required radiation-diffraction hydrodynamic force coefficients for the functional relationship. Based on this linear superposition principle, an overall device performance in random seas with narrow or broad banded wave spectra characteristics was determined and expressed as an average capture width ratio.

As a result of this research, several important conclusions can be drawn.

(1)   In random seas, the performance of the device is influenced by the frequency bandwidth of the wave spectra. In particular, an increase in the spectral bandwidth parameter ν causes a reduction in peak performance, but effectively broadens the frequency response of the device.

(2)   The design of an OWC device with a broad banded response in monochromatic seas is clearly advantageous to the performance of the device in random seas. Although the overall peak performance is reduced, the relatively broad peak response is still maintained for large spectral bandwidth parameters.

(3)   Probabilistic models for the determination of average wave power in a random sea state were developed based on a standard transformation of random variables and theoretical probability distributions of wave heights (pdf(R)) and wave heights and periods (pdf(R,τ)). These models were shown to accurately predict the average wave power in a random sea. The probabilistic model which accounted for the random distribution of both wave heights and periods produced the best results. This model is more realistic than previous approximate methods because the spectral bandwidth parameter ν is included, a parameter which leads to a more detailed description of the spectrum.

(4)   Modelling the 3-dimensional radiation-diffraction effects of the oscillating water column device by the hybrid finite element method and an analytical model describing the interior OWC surface motion was shown to accurately predict the device performance for a wide range of regular wave experimental frequencies.

(5)   An experimental program to identify the variation in natural frequency of the device with submergence depth (draft) was carried out in the Technical University of Nova Scotia wave tank and was shown to be in agreement with the 3-dimensional numerical model results.

(6)   A comparison of six different types of OWC devices, numerically modelled in finite depth and monochromatic seas, was carried out to determine the effects of wave frequency and direction on device performance. The devices modelled included the attenuator device (type 1) and three terminator type devices with a single back wall (type 2), back wall and two half side walls (type 3), and a back wall and two full side walls (type 4). By gradually extending the walls of the device down to the seafloor, the effects of added mass, radiation damping, and diffraction on device performance were quantified. Based on the results, device type 3 (a device not previously considered in the

literature) showed a slightly improved performance over the standard terminator type device (type 4). Because of this result, a similar device with a back wall and one full side wall (type 5) was considered and was shown to have a significantly improved peak performance over device type 4 and the other device types for a wide range of incident wave directions. Although the various device types showed considerable variation in the natural frequency and peak performance, the frequency response was fairly narrow banded for each device type. Device type 6 consists of two parallel projecting side walls from the front of the device and has been found by previous investigators to create an additional resonance which effectively broadens the response. This additional resonance was also observed in this research and when compared to the other device types, showed the broadest frequency response, but not the best peak performance for incident wave directions in the range of $\pm 40°$.

A number of possible areas of future research are identified below.

(1) A theoretical probabilistic analysis and experimental program which investigates the potential wave power extraction of an OWC device in a random sea with wave amplitudes exceeding the submergence depth of the front OWC wall would be of considerable interest. Investigations into potential wave power extraction over a portion of the wave cycle would be required in this area of research.

(2) The use of the linear diffraction theory for determining the response of the oscillating water column device has led to a better understanding of the fluid-structure interaction in this research. An extensive experimental study would be beneficial for a better understanding of the viscous effects and their importance in estimating the hydrodynamic forces on the OWC device.

(3)   The interaction between seafloor sediment transport processes and the oscillating water column device is poorly understood. An experimental study which models this complicated interaction would be useful in assessing whether or not sediment accretion could occur in the interior of the device, a process which may affect the design natural frequency and ultimately the device performance. The conditions which cause these sediment processes would aid in the engineering analysis of determining if the device should be elevated above the seafloor to prevent sediment from entering the device.

(4)   Results from this research confirms previous research results that an OWC device with two parallel projecting side walls has a relatively broad frequency response when compared to other types of OWC devices. However, the degradation in peak performance with increased incident wave direction is similar to previous OWC device types and a theoretical study followed through by an experimental program should be undertaken to improve this directionality bandwidth while maintaining (or possibly improving) the frequency response.

(5)   Quantifying the effects of non-linear waves on the annual distribution of wave power and performance of the oscillating water column would be of considerable value to researchers studying existing or proposed shore-based oscillating water columns. Curran et al. (1995) monitored the air flow rate at the Islay Wave Power Plant and reported non-linear characteristics in the time-series which they attributed to the shallow water wave effects. Superimposed on this non-linear effect may also be the non-linearities associated with the non-vertical walls at the Islay plant, an effect first studied by Hassan (1984) and Watts and Graham (1985).

REFERENCES

Ambli, N., Bonke, K. Malme, O. and Reitan A., "The Kaevernor Multi-resonant OWC", Proc. 2nd Int. Symposium on Wave Energy Utilization, Trondheim, Norway, June 1982.

Baird, W.F. and Mogridge, G.R., "Estimates of the Power of Wind-Generated Water Waves at Some Canadian Coastal Locations," National Research Council Canada, Hydraulic Laboratory Tech. Report. No. LTR-HY-53, 1976.

Borgman, L.E., "Directional Spectral Models for Design Use for Surface Waves," Preprints, Offshore Technology Conference, 1979.

Budal, K. and Falnes, J., "A Resonant Point Absorber of Ocean Wave Power," Nature, 256; 478-9, 1975.

Budal, K, Falnes, J., Kyllingstand, A., and Oltedal G., "Experiments with Point Absorbers," Proceedings 1st Symposium Wave Energy Utilization Gothenburg, Gothenburg Chalmes Technical University, 1980.

Canadian Atlantic Storms Program (CASP), Unpublished Wave Spectra Data Obtained from the Department of Fisheries and Oceans, Physical Oceangraphy Division, 1986.

Chen, J., and Chen G., "Hydrodynamic Analysis and Design Method of OWC Wave Energy Convertors," J. Hydrodynamics, Volume 1, No. 4, pp. 20-26, 1987.

Count, B.M., "Theoretical Hydrodynamic Studies on Harbour Systems for Wave Energy Absorption", CEGB, Technology Planning and Research Division, Marchwood Engineering Laboratories, March 1983.

Count, B., Fry, R. and Haskell, J., "An experimental investigation of the Harbour Concept in Wave Energy", CEGB, Technology Planning and Research Division, Marchwood Engineering Laboratories, March 1983.

Count, B.M., Fry, R., Haskell, J., and Jackson, N., "The M.E.L. Oscillating Water Column," CEGB Report No. RD/M/1157N81, 1981.

Curran, R., Raghunathan, R.S., Stewart, T.P. and Whittaker, J.T., "Matching a Wells Turbine to the Islay Oscillating Water Column Wave Power Converter", OMAE, Offshore Technology, Volume 1-A, ASME, pp. 147-154, 1995.

Eatock Taylor, R. and Zietsman, J., "Hydrodynamic Loading on Multi-component Bodies," Proc. 3rd Int. Boss. Conf., MIT, Hemisphere Publishing Corp., Vol. 1, pp. 424-443, 1982.

Evans, D., "Wave Power Absorption within a Resonant Harbour", Proc. of 2nd Int. Symp. on Wave Energy Utilization, Trondheim, Norway, pp. 371-382, June 1982.

Evans, D. and McIver, P., "A Hydrodynamic Theory for Wave Energy Devices with Projecting Sidewalls in Harbours", Journal of Fluid Mechanics, 1988.

Evans, D.V., "Power From Water Waves", Ann. Rev. Fluid. Mech., Vol. 13, pp. 157-187, 1981.

Evans, D., "The Oscillating Water Column Wave Energy Device," J. Inst. Math. Its. Appl., Vol. 22, pp. 423-33, 1978.

Evans, D., "Some Analytical Results for Two and Three Dimensional Wave Energy Absorbers," Power from Sea Waves. Proc. IMA Conf., Edinburgh, 1979.

Evans D., "Some Theoretical Aspects of 3-D Wave Energy Absorbers", 1st Symposium on Wave Energy Utilization, Sweden, 1979.

Funke, E.R. and Mansard, E.P.D., "On the Synthesis of Realistic Sea States in a Laboratory Flume," National Research Council of Canada, Hydraulics Laboratory, Tech. Rept., LTR-HY-66, 1979.

Greenberg, D., "The Response due to a 3-D OWC Wave Energy Absorber," Journal of Marine-Hydrodynamics, Dec. 1990.

Grove-Palmer, C.O.J., "Wave Energy in the United Kingdom - A Review of the Programme June 1975 - March 1982," Proceedings of 2nd Int. Symp. on Wave Energy Utilization, Trondheim, Norway, June 1982.

Hassan, K.M., "Investigation of the Oscillating Water Column Ocean Wave Energy Converter,", MSc Thesis, Technical University of Nova Scotia, Halifax, Canada, 1984.

Hasslemann, K., Ross, D.B., Muller, P., and Sole, W., A Parametric Wave Prediction Model, J. Phys. Oceanography, Vol. 6, pp. 200-228, 1973.

Hunt, J.N., "Direct Solution of Wave Dispersion Equation," J. Waterway, Port, Coast and Ocean Division, ASCE, Vol. 105, No. WW4, pp. 457-459, 1979.

Koola, P.M., Ravindran, M. and Aswatha Narayana, P.A., "Model Studies of Oscillating Water Column Wave-Energy Device," Journal of Energy Engineering, Vol. 121, No. 1, April 1995.

Lamb, H., Hydrodynamics, 6th Ed. Cambridge University Press, 1932.

LeBlond, P.H., Catisal S.M. and Isaacson, M., "Wave Spectra in Canadian Waters," Marine Environmental Data Services Branch, Department of Fisheries and Oceans, Canadian Contractor Report No. 6, 1982.

Long, A.E., "The Oscillating Water Column (Point Absorber)" Proceedings of a Workshop on Wave Energy, Maidenhead, December, pp. 33-45, 1979.

Longuet-Higgins, M.S., "The Statistical Analysis of a Random Moving Surface." Phil. Trans. R. Soc. London, A249, pp. 249, 321-387, 1957.

Longuet-Higgins, M.S., "On the Statistical Distribution of the Heights of Sea Waves." J. Marine Res., XI (No. 3), pp. 245-265, 1951.

Longuet-Higgins, M.S., "On the Joint Distribution of Wave Periods and Amplitudes in a Random Wave Field", Proc. Royal Society of London, A389, pp. 241-258, 1983.

Ma, Q.W., "Non-linear Analysis on Hydrodynamic Performance of Oscillating Water Column Wave Energy Device with a Lateral Opening", OMAE Offshore Technology, Volume 1-A, ASME, pp. 131-136, 1995.

Maeda, H., Kinoshita, T., Masuda, K. and Kata, W., "Fundamental Research on Oscillating Water Column Wave Power Absorbers," Journal of Energy Resources Technology, Vol. 107, ASME, pp. 81-86, March 1985.

Mansard, E.P.D., "Different Methods of Evaluating Wave Power in a Random Sea State: A Comparative Study," National Research Council of Canada, Hydraulic Laboratory, Tech. Rept. HY-97, 1978.

Marine Environmental Data Service (MEDS) Waves Recorded off Osborne Head, Station #37, Unpublished Data Set, Environment Canada, 1991.

McCormick, M., Ocean Wave Energy Conversion, Wiley and Sons, 1981.

McCormick, M.E., "Analysis of a Wave-Energy Conversion Buoy," Journal of Hydronautics, Vol. 8, No. 3, pp.77-82, 1974.

McCormick. M.E., "A Modified Linear Analysis of a Wave Energy Conversion Buoy," Journal of Ocean Engineering, Vol. 3, pp. 133-144, 1976.

McIver, J. and Evans, D., "An Approximate Theory for the Performance of a Number of Wave Energy Devices Set into a Reflecting Wall," Applied Ocean Research, April 1988.

Mei, C.C., "Numerical Methods in Water Wave Diffraction and Radiation," Annual Review Fluid Mech., Vol. 10, pp.393-416, 1978.

Mogridge, G.R., "A Review of Wave Power Technology," National Research Council of Canada, Hydraulics Laboratory, LTR-HY-74, 1980.

Moody, G.W. and Elliot G., "The Development of the N.E.L. Breakwater Wave Energy Convertor," Proc. 2nd International Symposium on Wave Energy Utilization, Trondheim Norway, June 1982.

Neumann, G.and Pierson, W.J., Principles of Physical Oceanography, Prentice-Hall, Inc., N.J., 1966.

Ochi, M.K. and Wang, W.C., "Non Gaussian Characteristics of Coastal Waves," Proc. 19th Conf. Coastal Engineering, ASSCE, Vol. 1, pp. 516-531, 1984.

Pawlowski, J.S., "An Algorithm for Finite Element Computation of Linear Scattering Problems," Institute for Marine Dynamics (IMD), Report No. LTR-SH-378, 1985.

Pierson, W.J. and Moskowitz, L., "A proposed spectral form for fully developed wind seas based on the similarity theory of S.A. Kitaigorodskii. "J. Geog. Res., Vol. 69, pp. 5181-5190, 1964.

Pizer, D., "Maximum Wave Power Absorption of Point Absorbers under Motion Constraints", Applied Ocean Research, Vol. 15, No. 4, pp. 225-236, 1993.

Pontes, M.T., Athanassoulis, G.A., Barstow, S., Cavaleri, L., Holmes, B., Mollison, D., and Ollveira-Pires, H., "An Atlas of the Wave Energy Resource in Europe," OMAE, Offshore Technology, Vol. 1-A, ASME, pp. 155-163, 1995.

Raghunathan, S., "The prediction of performance of biplane wells turbine", Proc. of the 3rd Int. Society of Offshore and Polar Eng. Cont., Singapore, Vol. 1, pp. 167-175, 1993.

Rahman, M. and Bhatta, D.D., "Wave Scattering by a Floating Circular Cylindrical Structure", Dept. of Applied Mathematics, TUNS, August 1992.

Robinson, R.W., "The Effects of Geometric-Wavefield Interactions on the Performance of Oscillating Water Column Wave Energy Convectors," PhD Thesis, Queens University, Belfast, 1982.

Sarmento, A.J. and Falcao, A.F., "Wave Generation by an Oscillating Surface Pressure and its Application in Wave-energy Extraction," Journal of Fluid Mechanics, Vol. 150, pp. 467-485, 1985.

Sarpkaya, T. and Isaacson, M., "Mechanics of Wave Forces on Offshore Structures," VanNostrand Reinhold Company, New York, pp. 651, 1981.

Scott, J.R., "A Sea Spectrum for Model Tests and Long-Term Ship Protection." J. Ship Research, Vol. 9, pp. 145-152, 1965.

Teng, B. and Eatock Taylor, R., "New Higher Order Boundary Element Methods for Wave Diffraction/Radiation," Applied Ocean Research, Vol. 17, pp.71-77, 1995.

Tzong, T.J., Wu, F.H.Y., and Leung, T.C.F., "Modelling of a Resonant Wave Power System by Three-Dimensional Finite Elements", Proc. 6th Int. Off. Mech. and Arctic Eng. Symp., Vol. 1, 455-463, 1987.

Walpole, R.E. and Myres, R.M., Probability and Statistics for Engineers and Scientists, 2nd Edition, MacMillan Publishing Co. Inc., N.Y., 1978.

Watts, K.C., Hassan, K.M., Sarwal, S.N., Alexander H.C. and Graham, J.W., "Non-Linear Analysis of a Non-Vertical Walled OWC Ocean Wave Energy Converter", 5th Offshore Mechanics and Arctic Engineering Symposium, Dallas, Texas, 1985.

Watts, K.C. and Graham, J.W., "Ocean Wave Energy Conversion Devices Popular Today." Proc. of CSME, Halifax, Vol. 9, No. 2, pp. 105-113, 1985.

Whittaker, T.J.T., Robinson R.W. and Murray, M.A., "A Hydrodynamic Study of an Oscillating Water Column Wave Energy Converter," Future Energy Concepts, I.E.E. Conf., 1981.

Whittaker, T.J.T., "Small scale low cost wave energy power devices, Phase 3: electrical production." ETSU Report HMSO, 1993.

Whittaker, T.J.T., "Islay Gully Wave Energy Device, Phase 2: device construction and pneumatic monitoring." ETSU Report No. ETSU WV 1680, HMSO, 1991.

Yue, D.K.P., Chen, H.S. and Mei, C.C., "A Hybrid Element Method for Calculating Three-Dimensional Water Wave Scattering," MIT Report MITSG-76-19, pp. 222, 1976.

APPENDIX A

SCATTER DIAGRAMS OF WAVE DATA AND AVERAGE WAVE POWER FOR
OSBORNE HEAD, NOVA SCOTIA

Station 37

Osborne Head, Nova Scotia

December 12, 1970 to December 8, 1990

No. of Observations (N_tot) 56,600

CHARACTERISTIC WAVE HEIGHT

Hc (meters)	Hc (feet)	2.5	3.5	4.5	5.5	6.5	7.5	8.5	9.5	10.5	11.5	12.5	13.5	14.5	15.5	16.5	17.5	18.5	19.5
	28.5																		
	27.5																		
	26.5																		
	25.5										1	3							
8.0	24.5										1	2						2	
	23.5									2	4	3							
	22.5									2	3								
7.0	21.5								2	7	5	1							
	20.5								4	7	3	1					1	2	2
	19.5							9	11	11	9	1					2		
6.0	18.5						2	1	14	19	3				4	5			
	17.5					4		2	25	31	9	2			1	6			
	16.5				3	3	18	43	50	25		1		1	4	4		3	
5.0	15.5				18	44	53	16				4	6						
	14.5			2	46	61	86	58	20		5	8			2		1		
	13.5			9	57	75	76	56	28	9	8			3		2	1		
4.0	12.5		1	23	68	94	71	65	42	3	5								
	11.5		6	49	95	137	110	150	77	28	4	1	1	2					
	10.5		18	87	130	175	178	97	33	5	2	2							
3.0	9.5		2	70	140	147	269	210	205	107	37	7	4						1
	8.5		14	178	217	288	347	345	265	117	27	2				1			
	7.5		4	85	361	332	434	459	356	131	39	8	17	2					
2.0	6.5	1	14	290	499	450	657	635	394	126	33	10	8			1			
	5.5	3	83	617	652	621	1103	1367	779	465	173	49	12	20	1				
	4.5		55	415	1124	827	921	1884	1935	833	468	140	48	10	26	2	2		
1.0	3.5	2	317	881	1403	1121	1614	2755	2286	936	531	184	75	5	59	16	13	1	
	2.5	68	656	672	904	1139	1692	2381	1927	594	372	187	104	12	105	3	29	2	6
	1.5	233	193	209	309	530	926	1284	1076	344	228	169	193	95	7	95	2	19	4

PEAK PERIOD Tp (Seconds)

Figure A.1. Scatter Diagram of Characteristic Wave Height (Hc) and Peak Period (Tp) for Osborne Head, Nova Scotia (1970-1990)

Hc (meters)	Hc (feet)	\<PEAK PERIOD T_p (Seconds)\>																		$\sum_{j=1}^{m} H_{ci}^2 T_{pj}/P_{tot}$
		2.5	3.5	4.5	5.5	6.5	7.5	8.5	9.5	10.5	11.5	12.5	13.5	14.5	15.5	16.5	17.5	18.5	19.5	
	28.5																			0.025
	27.5																			0.024
	26.5																			0.030
8.0	25.5									.018	.007									0.034
	24.5									.011	.006	.006								0.060
	23.5									.009	.020									0.128
7.0	22.5								.009	.014	.005			.006						0.164
	21.5								.007	.027	.021	.005								0.245
	20.5								.016	.025	.016	.029	.014	.005	.011			.012		0.332
6.0	19.5			.001					.003	.029	.039	.042	.037	.004	.010					0.482
	18.5			.001				.005	.036	.046	.044	.065	.011	.017	.023					0.491
	17.5							.008	.047	.046	.046	.071	.095	.030	.007	.004	.024			0.608
	16.5							.006	.064	.050	.108	.136	.074	.003	.014	.014	.012			0.640
5.0	15.5							.029	.082	.071	.098	.128	.042	.011	.018	.013				0.597
	14.5					.003		.066	.098	.066	.167	.122	.046	.012	.021	.006		.003		0.728
	13.5					.010		.071	.104	.117	.128	.102	.055	.019	.018	.007	.005	.003		0.825
4.0	12.5				.001	.022		.072	.112	.093	.108	.102	.071	.005	.010					0.862
	11.5				.004	.039		.086	.138	.123	.163	.102	.040	.006	.002	.004		.002		1.001
	10.5				.010	.058		.098	.157	.162	.181	.107	.039	.006	.003	.003				1.215
3.0	9.5	.001			.033	.076		.090	.185	.160	.171	.097	.036	.004	.008				.001	1.233
	8.5	.001			.066	.094		.142	.191	.177	.085	.021	.002	.003	.004	.001				1.259
	7.5	.001	.001	.021	.106	.112	.166	.210	.217	.185	.074	.024	.005	.012	.001			.002		1.170
2.0	6.5	.001	.002	.054	.110	.114	.189	.288	.305	.154	.053	.015	.005	.004		.001		.001		0.964
	5.5	.001	.009	.082	.103	.113	.227	.260	.315	.226	.198	.052	.016	.004	.008	.001				0.430
	4.5	.001	.003	.030	.100	.087	.112	.299	.142	.130	.087	.028	.011	.002	.007	.001	.001			0.083
1.0	3.5	.001	.011	.039	.076	.072	.119	.213	.097	.060	.023	.010	.001	.001	.009	.003	.002			
	2.5	.001	.012	.015	.025	.037	.064	.101	.092	.031	.012	.007	.001	.001	.008	.001	.003	.001	.001	
	1.5	.001	.002	.003	.006	.013	.012	.018	.006	.004	.003	.004	.001	.001	.003	.001	.001	.001	.001	
		.005	.028	.099	.367	.633	.947	1.87	2.16	2.77	2.21	1.48	.616	.100	.177	.124	.013	.035	.002	13.629 KW/m
		.005	.028	.099	.367	.655	1.02	2.13	2.59	2.66	2.59	1.74	.715	.113	.195	.131	.013	.035	.002	15.768 KW/m

CHARACTERISTIC WAVE HEIGHT

Figure A.2. Scatter Diagram of Average Wave Power for Osborne Head, Nova Scotia (1970-199)

APPENDIX B

DETERMINATION OF THE AVERAGE OF THE HIGHEST 1/N
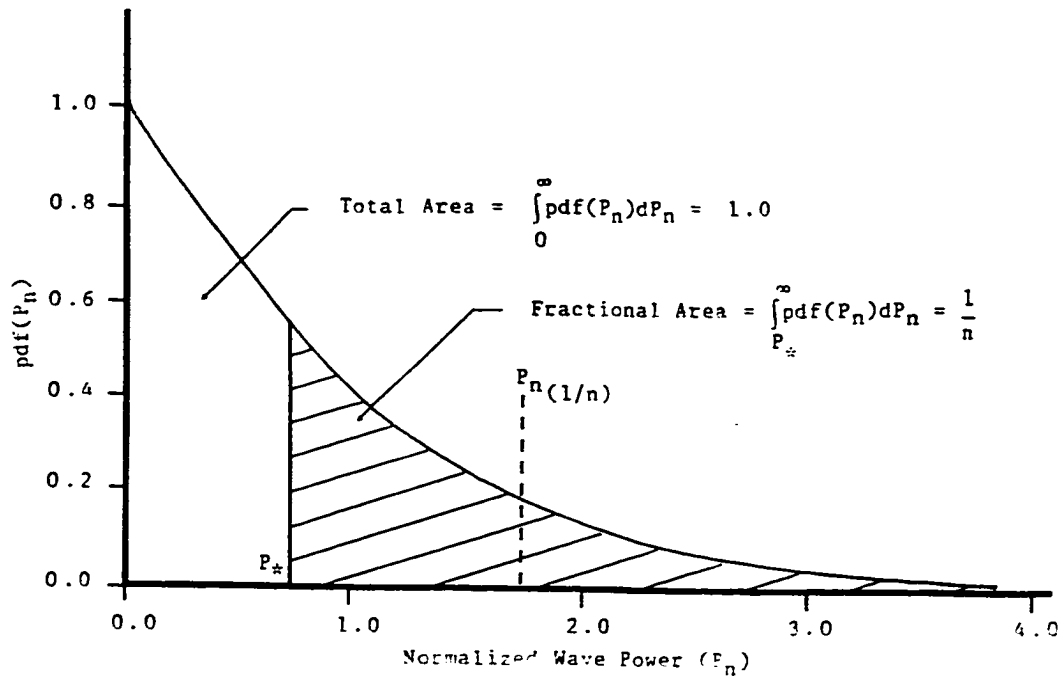NORMALIZED WAVE POWER VALUES

Figure B.1. Probability Density Function of Normalized Wave Power (Method A)

By definition of the probability density function, the total area under the pdf curve is

$$\int_0^{\infty} \text{pdf}(P_N)dP_N = 1.0 = \int_0^{\infty} (\exp{-P_N})dP_N \qquad \text{(B.1)}$$

The lower limit (P_*) of the highest $1/n$ normalized wave power values is given by

$$\int_{P_*}^{\infty} \text{pdf}(P_N) = \int_{P_*}^{\infty} (\exp{-P_N})dP_N = \frac{1}{n} \qquad \text{(B.2)}$$

and integrating yields

$$-\exp{-P_N} \Big|_{P_*}^{\infty} = \frac{1}{n} \qquad \text{(B.3)}$$

and

and

$$P_* = -\ln(\frac{1}{n}) \tag{B.4}$$

Therefore, the average of the highest $1/n$ normalized wave power values can be expressed by

$$P_{N_{1/n}} = \frac{\int_{P_*}^{\infty} P_N \ \text{pdf } (P_N)dP_N}{\int_{P_*}^{\infty} \text{pdf } (P_N)dP_N} = \frac{\int_{-\ln(\frac{1}{n})}^{\infty} P_N \ (\exp-P_N) \ dP_N}{\int_{-\ln(\frac{1}{n})}^{\infty} (\exp-P_N) \ dP_N} \tag{B.5}$$

where

$$\int_{-\ln(\frac{1}{n})}^{\infty} (\exp-P_N) \ dP_N = \frac{1}{n} \tag{B.6}$$

yields

$$P_{N_{1/n}} = \frac{\int_{-\ln(\frac{1}{n})}^{\infty} P_N \ (\exp-P_N) \ dP_N}{\frac{1}{n}} = \frac{\frac{1}{n}\left[1-\ln(\frac{1}{n})\right]}{\frac{1}{n}} = 1-\ln(\frac{1}{n}) \tag{B.7}$$

APPENDIX C

NON-DIMENSIONAL HYDRODYNAMIC COEFFICIENT CURVES OF VERTICAL
DIFFRACTION FORCE (C_z), HEAVE ADDED MASS (μ) AND
RADIATION DAMPING (b_r) FOR THE VARIOUS OWC DEVICE TYPES

$$C_z = \frac{F_d}{\rho g \alpha_o a^2} \ , \ \mu = \frac{m_a}{\rho a^3} \ , \ b_r = \frac{B_r}{\rho a^3 \sqrt{\dfrac{g}{a}}}$$
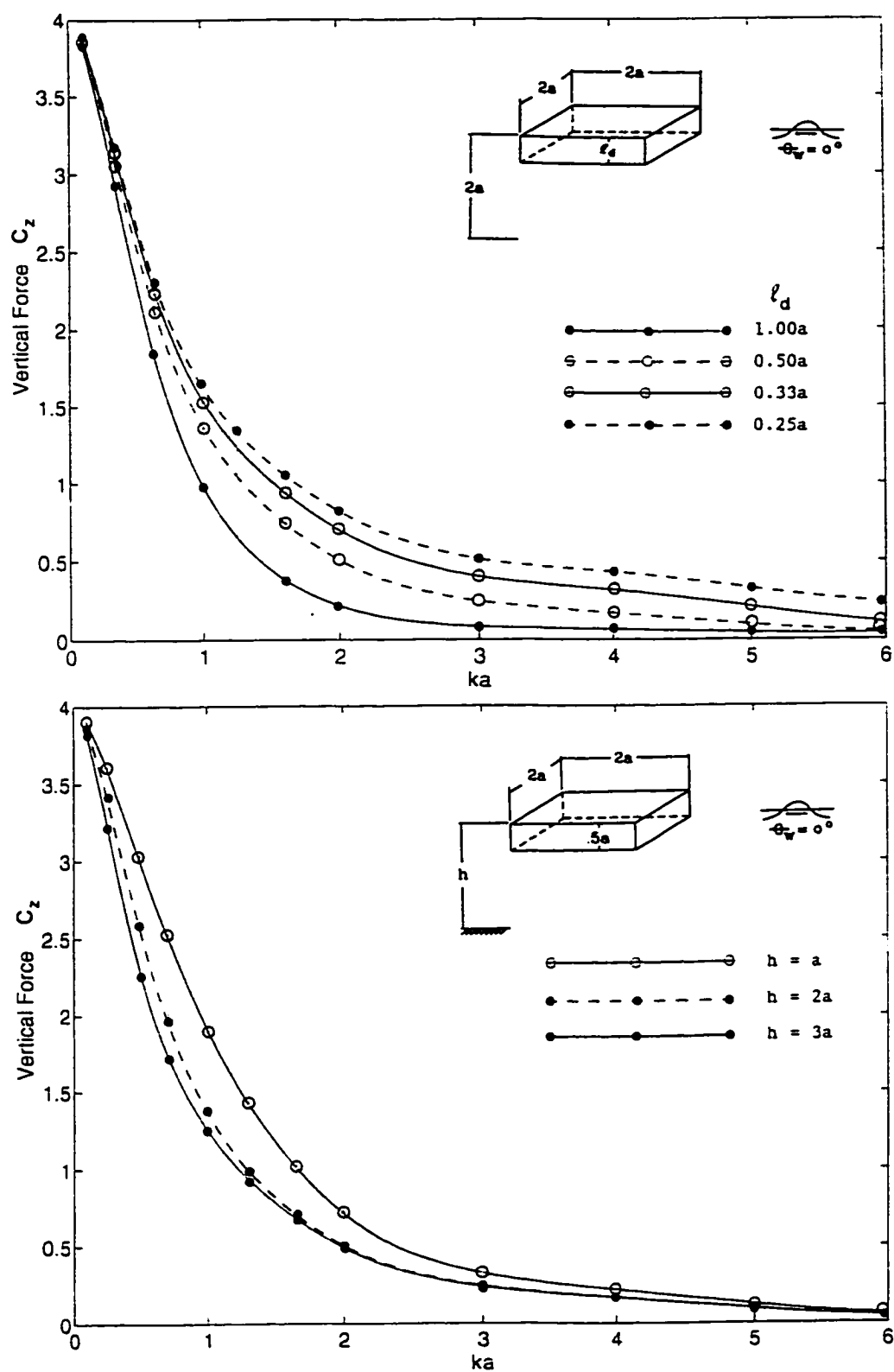
Figure C.1   Non-Dimensional Vertical Diffraction Force (C_z) for Device
Type 1 with Fixed Water Depth and Varying Drafts (Upper-
Figure) and Fixed Draft and Varying Water Depths (Lower
Figures)
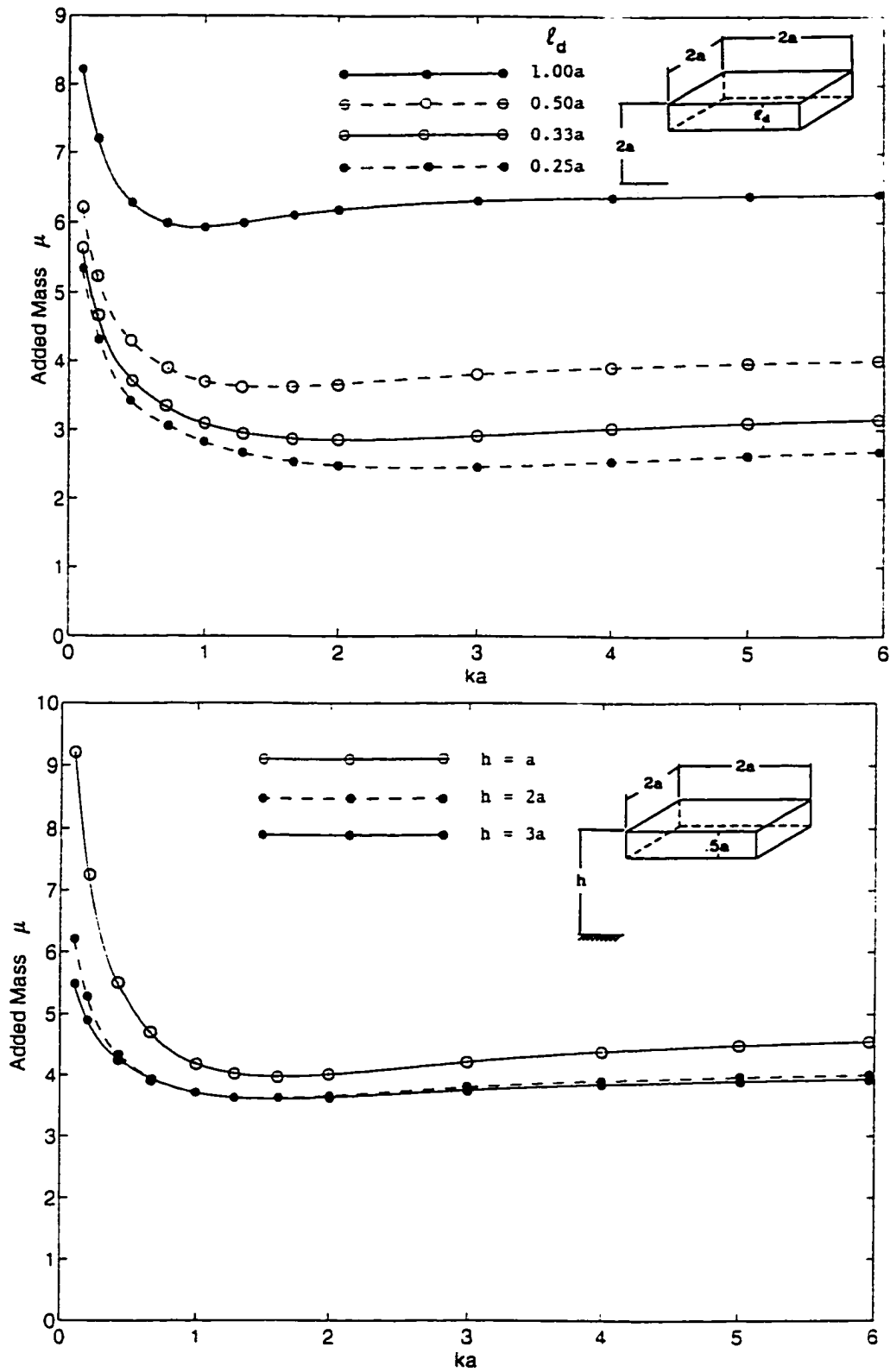
Figure C.2   Non-Dimensional Heave Added Mass (μ) for Device Type 1 with
Fixed Water Depth and Varying Drafts (Upper Figure) and
Fixed Draft and Varying Water Depths (Lower Figure)
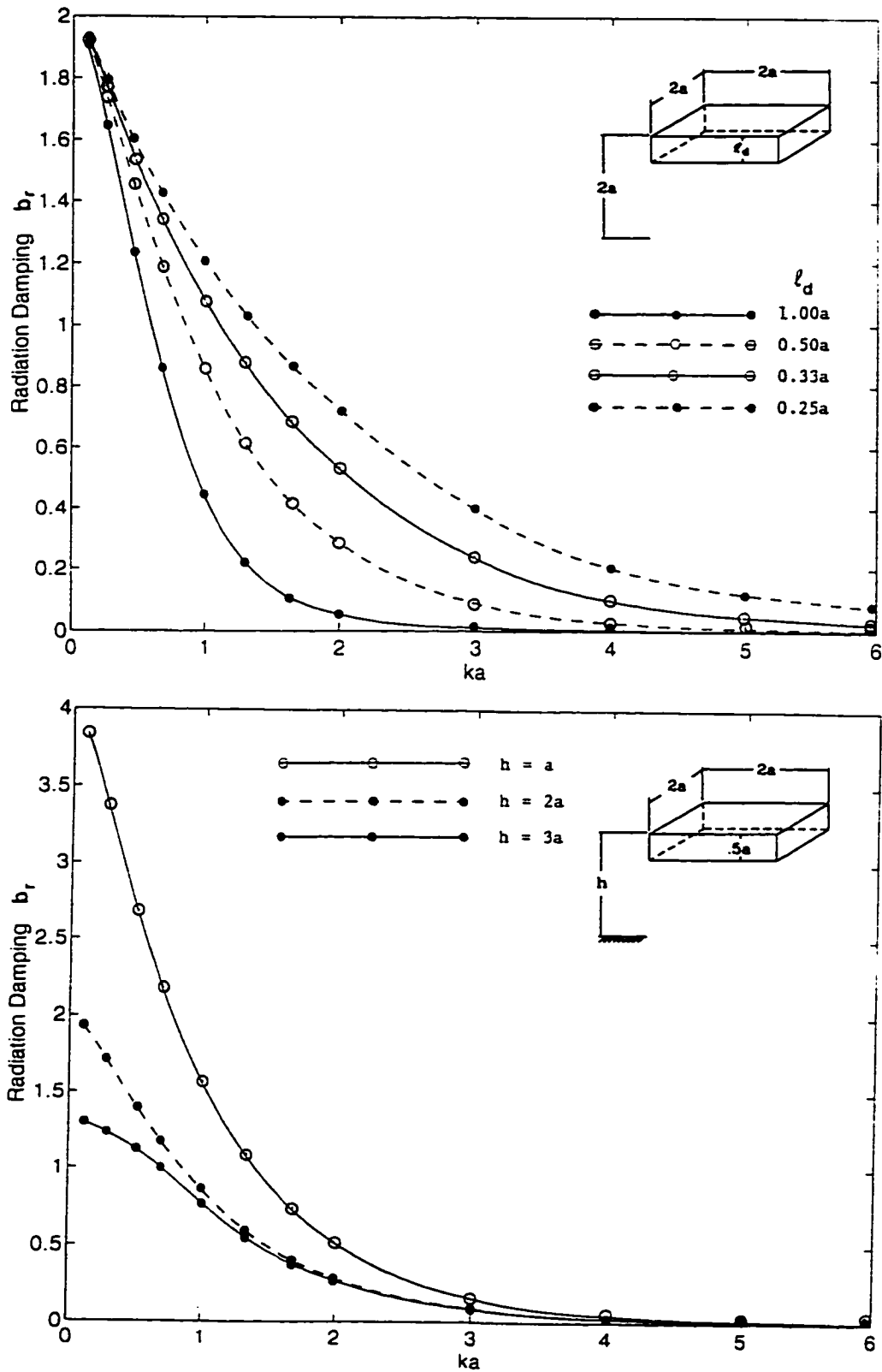
Figure C.3   Non-Dimensional Heave Radiation Damping (b_r) for Device
Type 1 with Fixed Water Depth and Varying Drafts (Upper-
Figure) and Fixed Draft and Varying Water Depths (Lower
Figure)
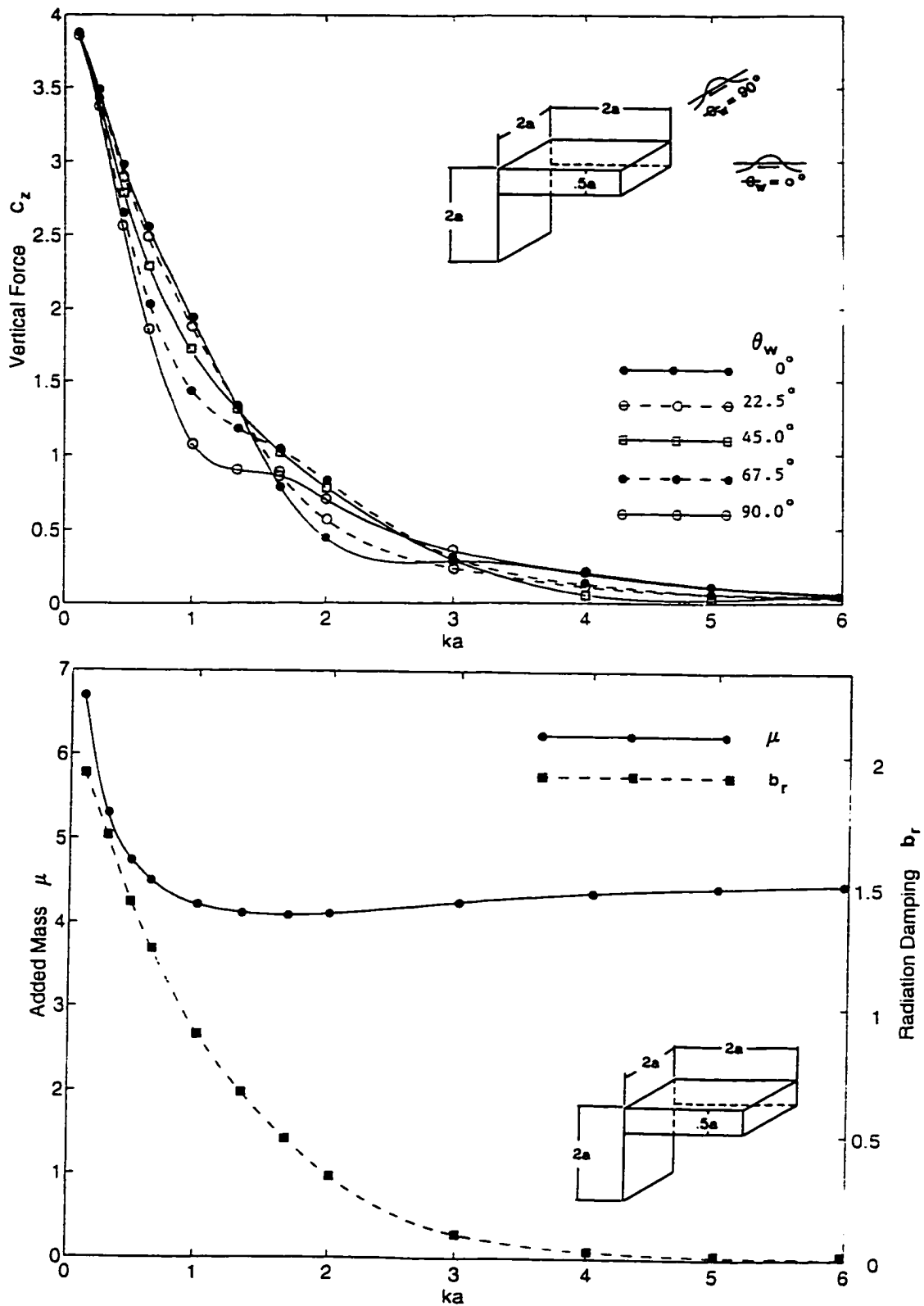
Figure C.4   Non-Dimensional Coefficients of Vertical Diffraction
Force (C_z), Heave Added Mass (μ), and Radiation Damping
(b_r) for Device Type 2
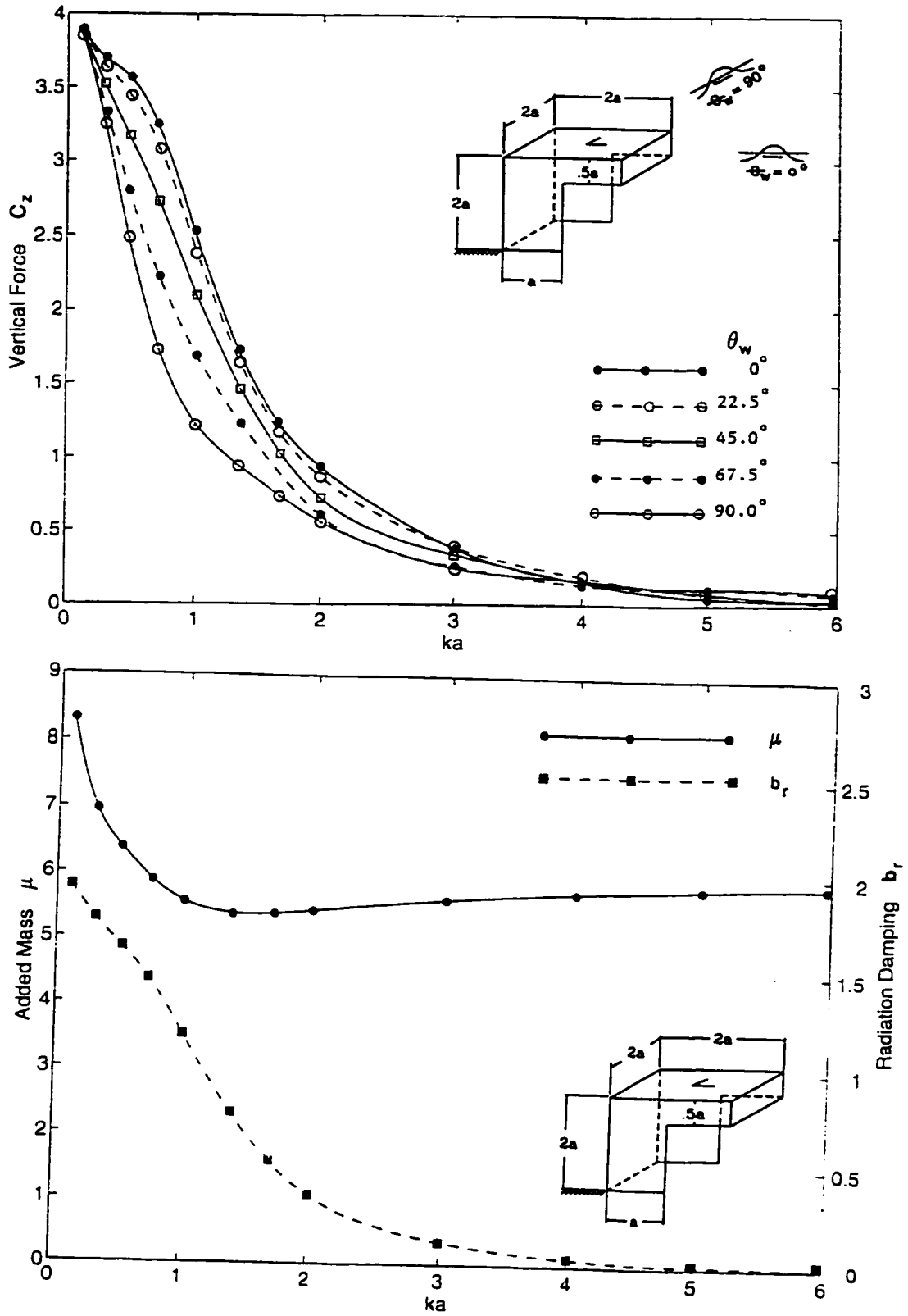
Figure C.5   Non-Dimensional Coefficients of Vertical Diffraction
Force (C_z), Heave Added Mass (μ), and Radiation Damping
(b_r) for Device Type 3
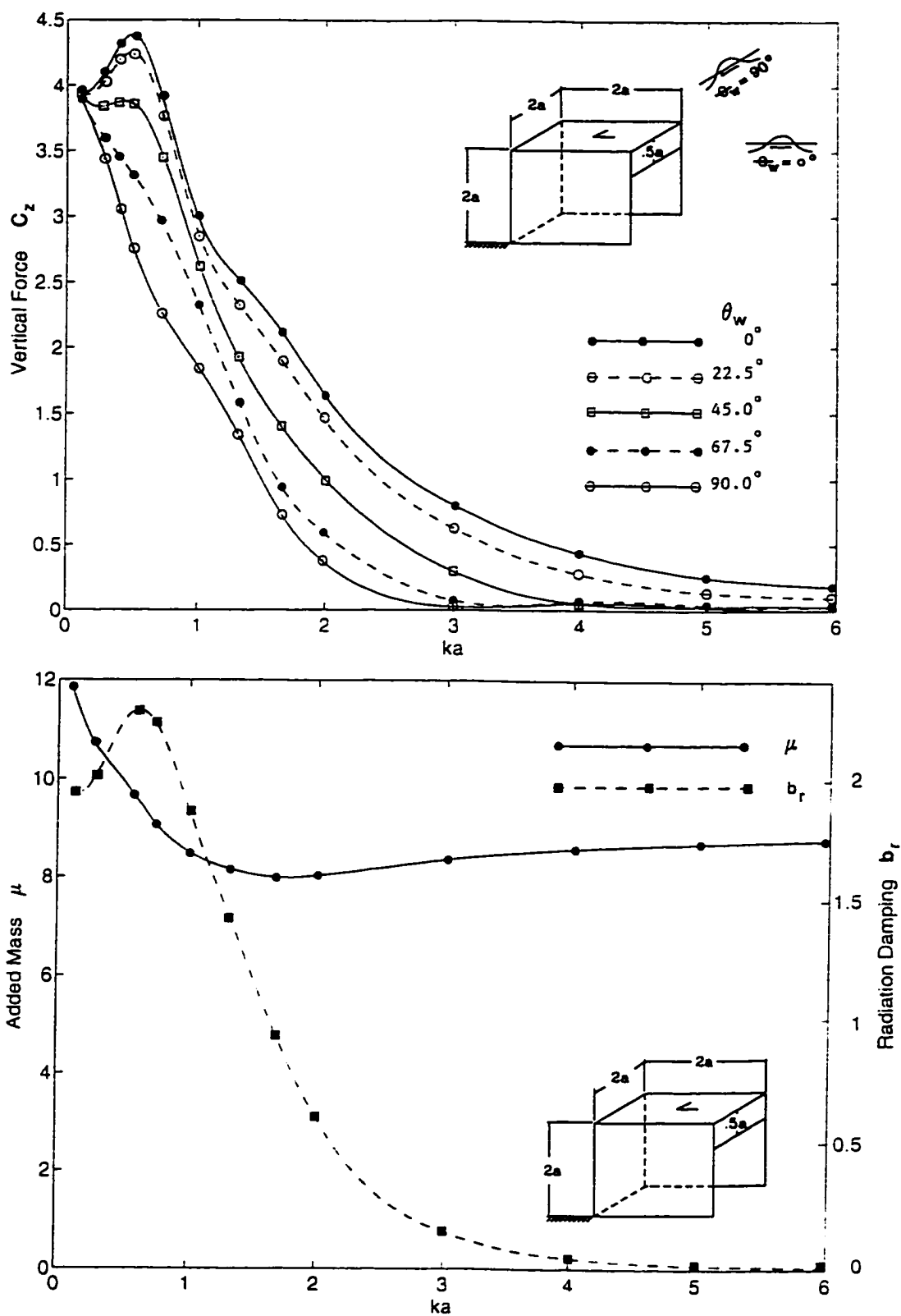
Figure C.6   Non-Dimensional Coefficients of Vertical Diffraction
Force (C_z), Heave Added Mass (μ), and Radiation Damping
(b_r) for Device Type 4
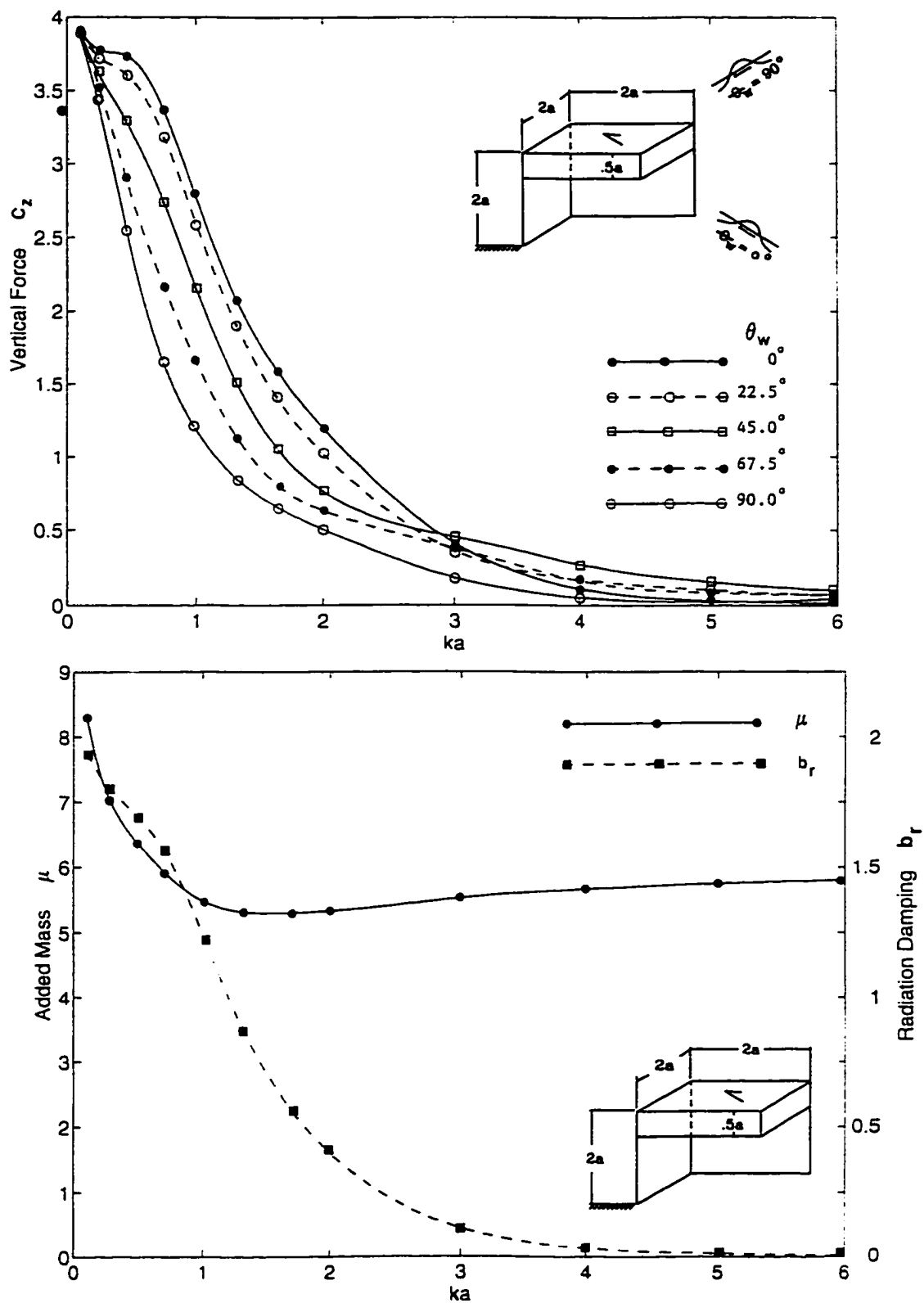
Figure C.7   Non-Dimensional Coefficients of Vertical Diffraction
Force (C$_z$), Heave Added Mass (μ), and Radiation Damping
(b$_r$) for Device Type 5
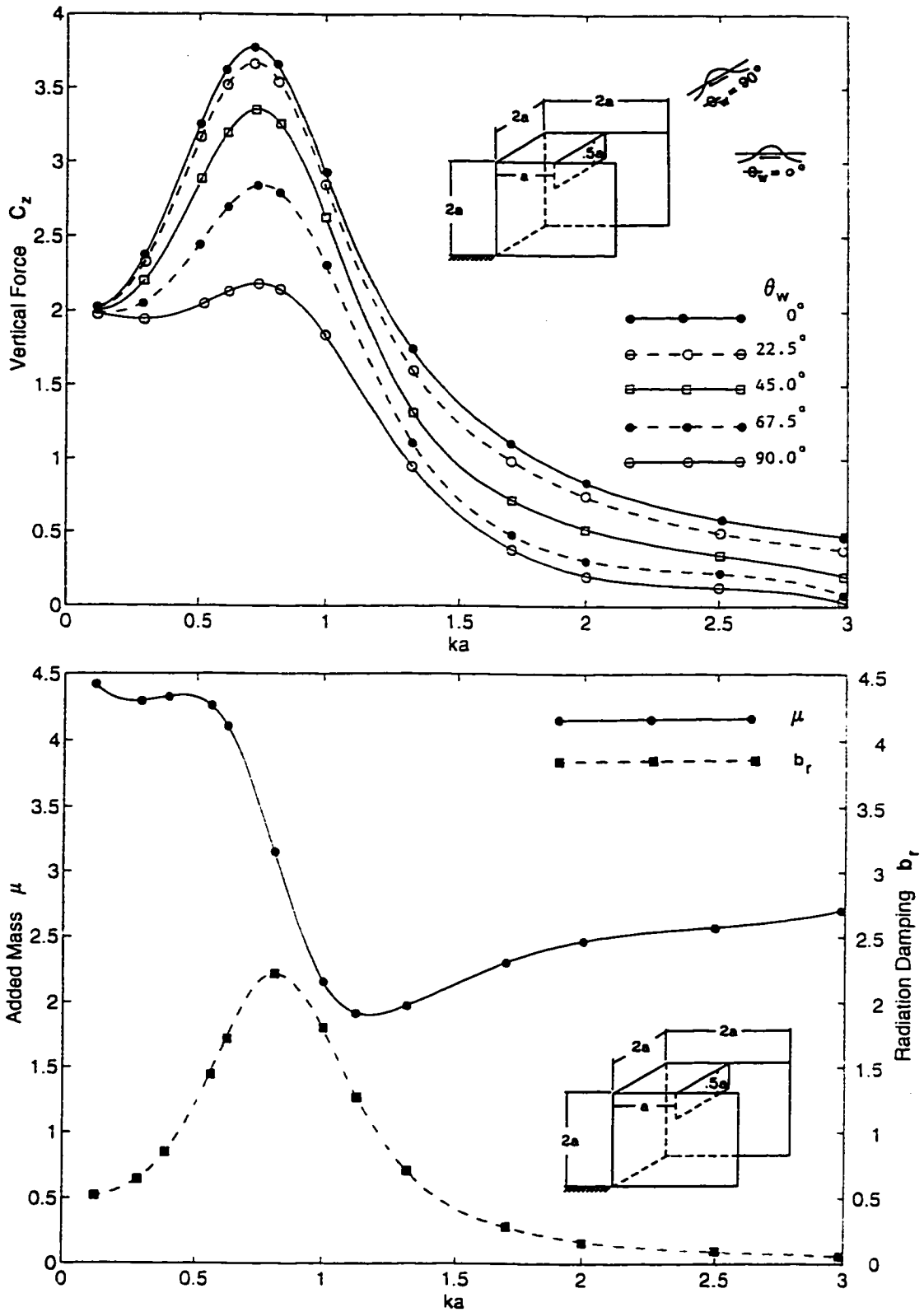
Figure C.8   Non-Dimensional Coefficients of Vertical Diffraction
Force (C_z), Heave Added Mass (μ), and Radiation Damping
(b_r) for Device Type 6

APPENDIX D

EVALUATION OF AVERAGE CAPTURE WIDTH RATIO ($\overline{\text{CWR}}$)
FOR A SPECTRAL BANDWIDTH PARAMETER EQUAL TO 0

D.1   Evaluation of $(\overline{CWR})$ for $v=0$

The integration in equation 6.28, for a spectral bandwidth parameter v equal to 0, can be determined analytically by the following substitutions:

$$\overline{CWR} = \frac{\displaystyle\int_0^\infty \int_0^\infty \alpha^{3/2}(\tau)\tau P_{e_N}^{3/2} \exp\left\{-\alpha(\tau)\tau^2 P_{e_N}\left(1+\frac{1}{v^2}\left(1-\frac{1}{\tau}\right)^2\right)\right\}d\tau dP_{e_N}}{\displaystyle\int_0^\infty \int_0^\infty \left(\frac{P_N^3}{\tau^7 f^3(\tau)}\right)^{1/2} \exp\left\{-\frac{P_N}{\tau f(\tau)}\left(1+\frac{1}{v^2}\left(1-\frac{1}{\tau}\right)^2\right)\right\}d\tau dP_N}$$

(D.1)

by letting $x = \frac{1}{v}\left(1-\frac{1}{\tau}\right)$ $dx = \frac{1}{v}\tau^{-2}\,d\tau$

Limits of integration: $\tau \to 0$, $x \to -\infty$

$\tau \to \infty$, $x \to \frac{1}{v}\,\Big|_{v=0} = \infty$

$\tau = \frac{1}{1-xv}\,\Big|_{v=0} = 1$

Substituting into equation D.1 gives

$$\overline{CWR} = \frac{\displaystyle\int_0^\infty \int_{-\infty}^\infty \alpha^{3/2}(1)P_{e_N}^{3/2} \exp\left\{-\alpha(1)P_{e_N}(1+x^2)\right\}dxdP_{e_N}}{\displaystyle\int_0^\infty \int_{-\infty}^\infty \left(\frac{P_N^3}{f^3(1)}\right)^{1/2} \exp\left\{-\frac{P_N}{f(1)}(1+x^2)\right\}dxdP_N}$$

$$= \frac{\displaystyle\int_0^\infty \alpha^{3/2}(1)P_{e_N}^{3/2} \exp\left\{-\alpha(1)P_{e_N}\right\} \int_{-\infty}^\infty \exp\left\{-\alpha(1)P_{e_N}x^2\right\}dxdP_{e_N}}{\displaystyle\int_0^\infty \left(\frac{P_N}{f(1)}\right)^{3/2}\exp\left\{-\frac{P_N}{f(1)}\right\} \int_{-\infty}^\infty \exp\left\{-\frac{P_N x^2}{f(1)}\right\}dxdP_N}$$

(D.2)

where the well known error function

$$\int_{-\infty}^{\infty} \exp\{-ax^2\}dx = \sqrt{\frac{\pi}{a}}$$

and equation D.2 reduces to

$$\overline{CWR} = \frac{\int_{0}^{\infty} \left(\frac{\pi}{\alpha(1)P_{e_N}}\right)^{1/2} \alpha^{3/2}(1)P_{e_N}^{3/2} \exp\{-\alpha(1)P_{e_N}\}dP_{e_N}}{\int_{0}^{\infty} \left(\frac{\pi f(1)}{P_N}\right)^{1/2}\left(\frac{P_N}{f(1)}\right)^{3/2} \exp\left\{-\frac{P_N}{f(1)}\right\}dP_N} \tag{D.3}$$

$$\overline{CWR} = \alpha(1)f(1)\frac{\int_{0}^{\infty} P_{e_N} \exp\{-\alpha(1)P_{e_N}\}\, dP_{e_N}}{\int_{0}^{\infty} P_N \exp\left\{-\frac{P_N}{f(1)}\right\}dP_N} \tag{D.4}$$

Performing an integration by parts gives

$$\overline{CWR} = \frac{1}{\alpha(1)f(1)} \tag{D.5}$$

where

$$\alpha(1) = \left(\frac{\overline{W}_T}{2\pi}\right)^3 \frac{1}{b_a}\left[\frac{\left(l_x l_y - \frac{4\pi^2\mu}{\overline{W}_T^2}\right)^2 + \left(\frac{2\pi}{\overline{W}_T}(b_a + b_r)\right)^2}{C_z^2}\right]$$
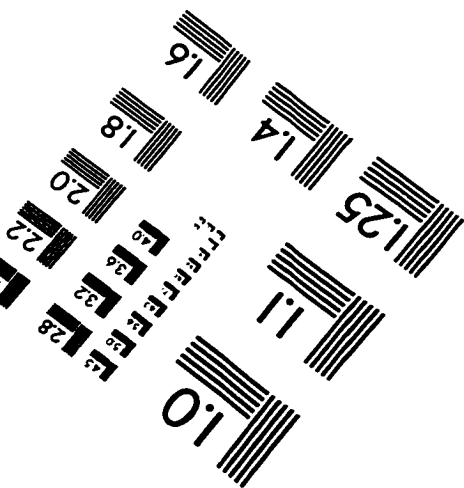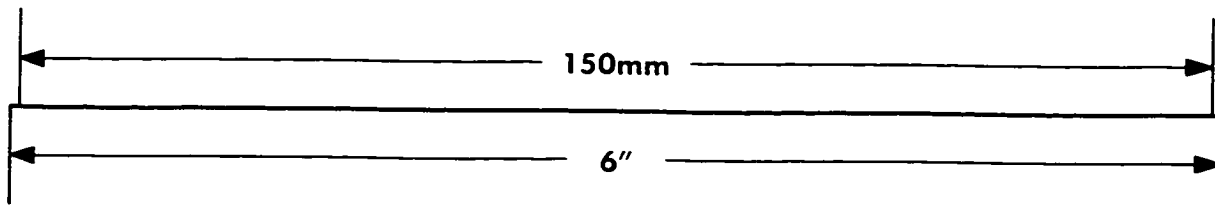
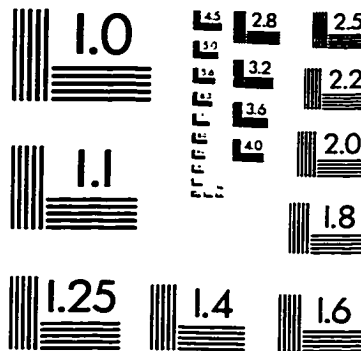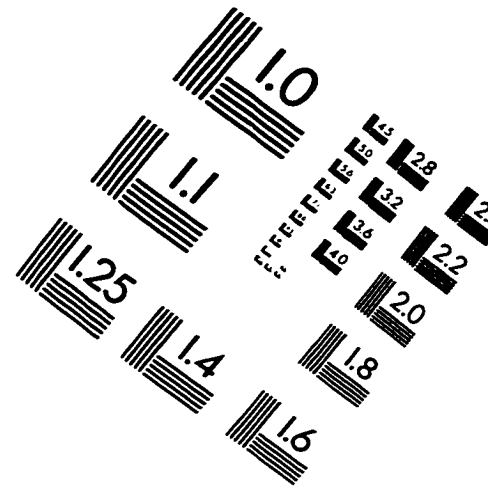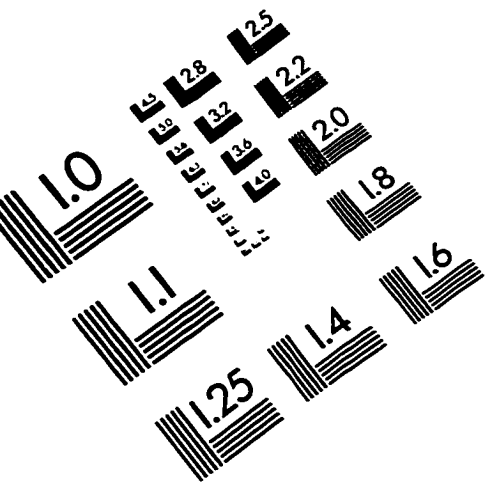$$f(1) = \left[1 + \frac{2kh}{\sinh 2kh}\right]\tanh kh$$

and the average capture width ratio for random seas with $v=0$ becomes

$$\overline{CWR} = \left(\frac{2\pi}{\overline{W}_T}\right)^3 b_a\left(\frac{\xi_0}{\alpha_0}\right)^2 \frac{1}{\left[1 + \frac{2kh}{\sinh 2kh}\right]\tanh kh} \tag{D.6}$$

which is equivalent to the capture width ratio in monochromatic seas for $T = T_{m_{01}}$.

IMAGE EVALUATION
TEST TARGET (QA-3)

150mm

6"
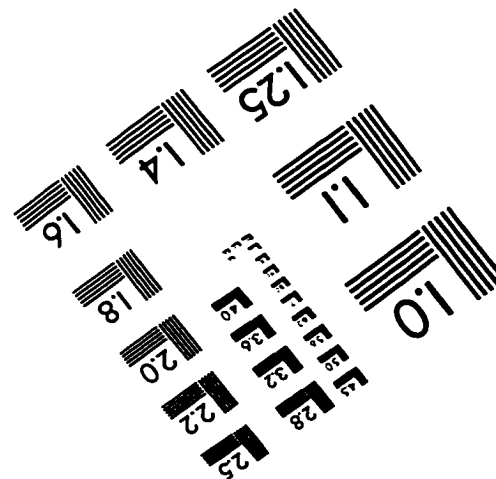
APPLIED IMAGE, Inc
1653 East Main Street
Rochester, NY 14609 USA
Phone: 716/482-0300
Fax: 716/288-5989

© 1993, Applied Image, Inc., All Rights Reserved